Simulations of Dissolution of Structured Particles

Hui Cao

Submitted in accordance with the requirements for the degree of
Doctor of Philosophy

The University of Leeds
School of Chemical and Process Engineering

April, 2015

The candidate confirms that the work submitted is her own and that appropriate credit has been given where reference has been made to the work of others.

ACKNOWLEDGEMENTS

I would like to acknowledge my supervisors, Dr Xiaodong Jia and Professor Yulong Ding along with all members of the research group. I wish to express my most sincere thanks to them for their time, advice, support, useful guidance, many valuable suggestions and comments.

Funding for this project was provided by Procter and Gamble; I should like to thank Dr Carlos Amador from P&G for the help and guidance provided over the course of my PhD.

ABSTRACT

This thesis presents a new modelling framework for the simulation of detergent powder dissolution. Focusing on population of particles containing multi ingredients with porous structure, the general model framework links mixing system power and particle dissolution behaviour by combining convective dissolution equations and computational fluid dynamics simulation.

Particle dissolves in a variety way due to many factors for example particle shape and size, pore structure, agitation speed, solvent material and temperature. It is difficult to quantitatively conclude these factors on dissolution. As a result, detailed simulations based on Lattice-Boltzmann method are carried out to investigate factors for instance particle shape, surface area to volume ratio and pore structure separately. Later on, both experiment and simulation methods have been studied to explore the effects of agitation and particle wetting process. Results show that surface area to volume ratio plays a more important role in terms of particle related properties. Results also indicate that agitation affects dissolution significantly comparing to the other studied factors.

The new dissolution model, expressed as a coupled system of numerical and computational issues, is used to predict particle dissolution behaviour in a well mixed system. Simple case study of single ingredient non porous particle sodium carbonate (provided by Proctor and Gamble) successfully shows the capability of the model by validating modelling results with experimental results. Later on, more complicated case study of multi ingredients porous detergent powder (PANDORA, one of the semi product in Proctor and Gamble) suggests that this model can predict porous particle dissolution while the particles are treated as spheres with envelope density.

Based on the good agreements between modelling and experiment data, this model can be applied for predicting bulk particle dissolution behaviour in different mixing systems, or the same mixing system but different bulk particle.

CONTENTS

LIST OF TABLES

LIST OF FIGURES

NOMENCLATURE

A surface area

A_0 initial surface area of particle

$A_{impeller}$ impeller surface area

C solute concentration of at time t

$C_{Max,Int}$ maximium internal concentration

C_s equilibrium solubility

$C_{s,\delta=0}$ solubility when diffusion layer thickness δ approaches zero

D diffusion coefficient

D_{AB} inter-diffusion coefficient in dilute solutions

D°_{AB} diffusion coefficient at infinite dilution

D_{fit} diffusivity from fitting result

D_{SE} diffusivity from Stokes-Einstein equation

F_c Faraday constant

F_{fr} frictional force

$F_{impeller}$ force acting on each point of impeller surface

F_{st} surface tension force

G surface specific dissolution rate

I identity matrix

K_0 zero order release constant

K_A new proportionality constant

K_{cr} constant in cubic-root law

K dissolution rate constant,

L characteristic length

L_T tablet length

M_B molecular weight of solvent

$N_{particle}$ particles number

N_P power number

N , Ω agitation speed

N_{factor} porosity factor

P impeller power

Q_0 initial amount of particle ingredient in the solution

Q_t amount of particle ingredient dissolved

R_{cr} critical radius

Re particle Reynolds number

Sc Schmidt number

Sh Sherwood number

T absolute temperature

V , V_f liquid volume

V_A molar volume of solute at the normal boiling point

V_{pore} pore volume

$V_{particle}$ particle bulk volume

V_s velocity of the flowing liquid against the flat surface

W solid weight

W_0 initial solid weight

Z_+ cation valence

Z_- anion valence

a constant

b constant

b_T tablet width

$d_{impeller}$ impeller diameter

d_p particle diameter

$d_{p,0}$ initial particle size

d_{tank} tank diameter

g acceleration of gravity

h the height of capillary rise

h_c characteristic mesh size

h_{eq} equilibrium height

k contact stiffness

k_B Boltzmann's constant

l_s length of the surface in the direction of flow

m mass of the particle

n interface normal

p pressure

r_p radius of the diffusing particle

t time

u_p diffusing particle velocity

u relative velocity between liquid and particle

$u_{\max}$ maximum liquid velocity in convective dissolution

(u_x, u_y, u_z) fluid velocity components

(x, y, z) spatial coordinates

Γ torque on impeller

α constant

β slip length

$\dot{\chi}$ parameter determines the amount of reinitialization

δ diffusion layer thickness

δ' Dirac delta function

ε turbulent energy dissipation rate

ϕ level set function

φ particle porosity

γ surface tension

$\dot{\gamma}$ shear rate

λ_+° cationic conductance at infinite dilution

λ_-° anionic conductance at infinite dilution

μ viscosity

μ_f liquid viscosity

θ wetting angle of the liquid

θ_{ad} advancing contact angle

θ_{eq} equilibrium contact angle

ρ density

ρ_f fluid density

$\rho_{particle,envelope}$ particle evelope density

$\rho_{particle,absolute}$ particle true density

σ surface tension coefficient

ξ parameter determines the thickness of the interface

ξ_B association factor of solvent

CHAPTER 1
INTRODUCTION

The dissolution behaviour of particles with microstructure in a liquid is very important for many products such as fertilizers, washing powders, pharmaceutical, various ‘instant’ food as well as special chemicals. The control of the dissolution process of particles is a key to achieve the desired functionalities of these products.

Theoretically, for a granule, its dissolution behaviour depends on the solubility of granule ingredients in a given liquid. According to this parameter, particles can be simply divided into two types, dissolvable and non-dissolvable. However, most granules in modern industry contain different chemical ingredients which have different solubilities. Meanwhile, the multi-ingredients granules are often in the forms of porous media. In this case, the dissolution kinetics is very different from one ingredient solid particle dissolving in liquid, it is much more complicated.

According to Hsu et al [1], the dissolving process of solid particles in liquid can broadly be divided into two steps: the escape of solute molecules from the solid surface and the diffusion of these molecules toward the bulk liquid phase. For a porous medium, for example washing powder, the dissolving of active ingredients consists of several steps: i) wetting of granules followed by penetration of liquid into pores in the granules due to capillary forces; ii) immersion of the granule into the liquid; iii) the dissolution of the solid bridges between the primary particles followed by the dispersion of the primary particles within the liquid; and iv) the dissolution of soluble primary particles [1]. It is important to note that in real processes these steps are difficult to be clearly isolated from each other. They may not happen sequentially, but rather occur simultaneously, and affect each other. Therefore, analysis and modelling of these processes remains difficult [1].

In this research, detergent granules are used as a physical model to build up a model to simulate the dissolution behaviour. The aim is to use the modelling results to help

the industry to control the manufacturing process and finally control the release of active ingredients during applications.

Aims and objectives The primary aim of this study is to help establish quantitative relationships between processing, microstructure, and end-use behaviour (dissolution) through a combination of physical experiments and computer simulation studies, and to develop a systematic procedure for rational granule microstructure design.

This project aims to understand dissolution behaviour of structured granules consisting of multi-ingredients. Objectives are:

i) To understand how parameters affect particle dissolution by either experiment or simulation or both.

ii) To establish mathematical models for linking the relationship between particle dissolution behaviour and the input power of the dissolution system. Finite element method is used to simulate the filling process of water into pores and the energy dissipation in a stirring tank. Meanwhile lattice Boltzmann method is used to simulate dissolving process of primary particles.

iii) To validate the relationship by carrying out the experiment of dissolution of detergent particles in water at different conditions, for example stirring speed and temperature. The detergent particles contain both porous and non porous structure.

Methodologies Both experimental work and mathematical modelling are carried out to investigate the dissolution behaviour of particles. Parameters such as particle shape, surface area to volume ratio, pore structure and agitation are simulated by combining a Lattice-Boltzmann method based code *DigiDiss* and Finite-Element method based software COMSOL Multiphysics. Noyes-Whitney equation is derived to suit dilute electrolyte solutions. The relationship between

importing power and particle dissolution behaviour is linked by numerical simulation and mathematical calculation. This relation is validated by the experiment of particle dissolution.

Organisation of the thesis This thesis is organised in following manner. Chapter Two reviews the literature relevant to this study including mass transfer theories, the factors affecting dissolution, the dissolution behaviour of structured particles, and then both experiment and simulation method related to particle dissolution. Chapter Three explains materials and preparation, experiments carried out in the presented study as well as simulation. Chapter Four starts from simulation of some parameters affecting dissolution, such as particle shape, surface area to volume ratio, pore structure and agitation. Chapter Five provides the derivation of equations for non-porous and porous particles dissolve in water based on Noyes-Whitney Equation, and the predictional results from the developed framework. The model framework is validate in Chapter Six by comparing experimental results to the predictional results from Chapter Five. Finally, a summary of the main conclusions is given in the Chapter Seven, where recommendations for the future work are also given.

CHAPTER 2
LITERATURE REVIEW

Dissolution is a process in which a solid substance solubilizes in a given solvent i.e. mass transfer from the solid surface to the liquid phase.

The earliest reference to dissolution was by Noyes and Whitney in 1897 [2], where they stated that the dissolution rate is governed by the rate of diffusion of a saturated thin layer forming instantly around the dissolving material.

Since then, dissolution phenomena have been studied for more than a century. The dissolution kinetics of powders is of critical importance in many industrial and consumer applications, ranging from food and pharmaceutical products, to chemicals, fertilizers, paints, etc.

The dissolution process of structured granules with multi-components is much more complex comparing to traditional regular shaped solid. The process could involve wetting of granules followed by penetration of liquid into pores depends on if the particle has a porous structure or not, then dissolution of the solid bridges between the primary particles followed by the dispersion of the primary particles within the liquid, and dissolution of soluble primary particles. The review is mainly on: i) fundamental theories of dissolution, ii) factors affecting dissolution, iii) processes involved in complex particle dissolution, iv) experimental test and v) modelling method of dissolution.

2.1 Mass transfer theories

In the general case, the dissolution rate of a pure substance depends on the total resistance of three possible sequential stages of the process: diffusional supply of solvent to the dissolving surface, the transition of dissolved substance from solid to solute state immediately at the dissolution surface and the transport of solute (by diffusion and/or convection) from the surface to the bulk of solvent [3].

The modelling of particle dissolution behaviour is relevant to many industrial processes. Examples include thermal processing of ferrous and non-ferrous alloys, dissolution of solid tablets, controlled release of agrochemicals, and food nutrition agents.

2.1.1 Formulation of mass transfer models

Theoretical models of dissolution continued to be developed in the early 1900s by Brunner, when he adapted Fick's Law of diffusion. In the 1930s the cube root law, which describes a linear relationship between dissolution rate and cube root of time, came into favour.

A number of older mathematical models have been developed to describe particle dissolution processes. Generally, the dissolution of a solid particle can be divided into three steps: (1) decomposition of the chemical component, (2) the crossing of the interfacial atoms, and (3) long-range diffusion in the matrix. Process (1) and (2) can be considered as interfacial process, while process (3) can be used when the interfacial processes are infinitely fast. As a result, for the dissolution dynamics, these models provide an upper boundary.

Zero order kinetics

Assuming that the area around the particle does not change and the solution is far from equilibrium conditions, the particle dissolution rate can be simply represented by:

$$Q_t = Q_0 + K_0 t \qquad 2\text{-}1$$

where Q_t is the amount of particle ingredient dissolved in time t , Q_0 is the initial amount of particle ingredient in the solution, and K_0 is the zero order release

constant [4]. Equation 2-1 indicates that particle ingredients dissolve the same amount into liquid per unit of time, which is obviously an ideal model. In a real situation, however, the assumptions of this model are rarely met.

Diffusion layer model

In 1897, Noyes and Whitney published a paper of "The Rate of Solution of Solid Substances in Their Own Solution" suggesting dissolution rate is controlled by a layer of saturated solution that forms instantly around a solid particle (see Figure 2.1) [2]. They developed the famous Noyes-Whitney equation:

$$V\frac{dC}{dt} = K(C_s - C) \qquad 2\text{-}2$$

where V is the liquid volume, K is dissolution rate constant, C is the solute concentration of at time t, C_s is the equilibrium solubility [2]. Figure 2.2 shows plots of data from Noyes and Whitney together with Equation 2-2 using the original estimates for the value of the constants. The authors proposed a mechanism that relate dissolution to a thin diffusion layer which is formed around the solid surface and through which the molecules diffuse to the bulk aqueous phase.

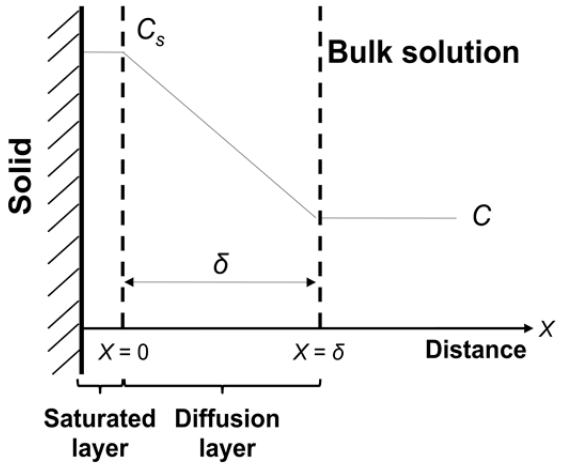

Figure 2. 1 Schematic of diffusion layer model of dissolution by Noyes and Whitney. C_s is saturated concentration, C is bulk concentration at time, and δ is diffusion layer thickness.

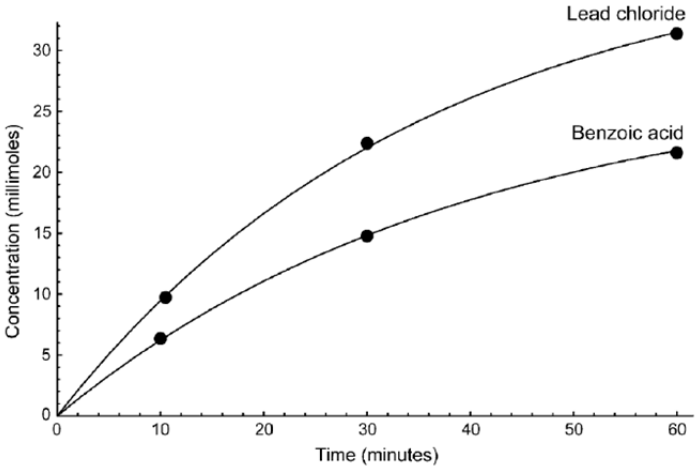

Figure 2. 2 Concentration-time plots of Noyes and Whitney [2] data together with plots of Equation 2-2 using the original estimates for the values of the constants [5].

Later on in 1900, based on Noyes and Whitney's work, Brunner and Tolloczko proved that dissolution rate depends on the chemical and physical structures of the solid, the surface area exposed to the medium, agitation speed, medium temperature and the overall design of the dissolution apparatus [6]. They further refined the Noyes-Whitney equation to consider the solid surface area exposed to the liquid and gave:

$$V\frac{dC}{dt} = K_A A(C_s - C) \qquad 2\text{-}3$$

where K_A is the new proportionality constant, and A is surface area [6].

Brunner further studied the specific relations between the constants and together with the theoretical work of Walther Nernst, they derived from Equation 2-3 and involved the diffusion layer concept and Fick's second law, and proposed what is known as the Nernst-Brunner equation [7, 8]:

$$V\frac{dC}{dt} = \frac{D}{\delta}A(C_s - C) \qquad 2\text{-}4$$

In 1931, by letting surface area A of Equation 2-3 to be proportional to the weight W, Hixson and Crowell made Equation 2-3 applicable to dissolving compact objects

[9]. Considering the concentration is far smaller than the saturated concentration, $C_s - C$ can be treated as constant, then Equation 2-3 can be integrated and yields a cubic-root law:

$$W^{1/3} = W_0^{1/3} - K_{cr}t \qquad 2\text{-}5$$

where W_0 is the initial weight and K_{cr} is a constant. In their paper, this equation hadn't been sufficiently validated with a wide range of experiments, nor to the explanations about the mechanism of the process.

Danckwert's model

Danckwert takes into account the eddies or packets that are present in the agitated fluid which reach the solid-liquid interface, absorb the solute by diffusion and carry it into the bulk of solution. These packets are continuously replaced by new ones and expose to new solid surface each time, thus the theory is called surface renewal theory.

Interfacial barrier model

The interfacial barrier model, considered that interfacial transport, rather than diffusion through the film, is the limiting step due to a high activation energy level for the former. This model was first proposed by Wilderman [10] in 1909 and was also considered by Zdanovskii [11] in 1946, but has not been studied in detail and an explicit mathematical description for the dissolution kinetics is not available, while variations have also appeared [12].

2.1.2 Diffusion coefficient

Diffusion is always related to dissolution. It is a net movement of a substance (e.g., an atom, ion or molecule) from high concentration to low concentration. It could happen between solid-solid, liquid-liquid, gas-gas and also in between them.

Diffusion in liquid is complex. Liquids are characterized by a combination of strong intermolecular forces in addition to the irregular chaotic arrangement of atoms present in the gas phase [13]. The difficulty in treating the liquid state becomes readily apparent since liquids in reality consist of clusters of irregularly arranged atoms or molecules which exist in an activated state and exhibit random motion.

Numerous attempts to predict molecular diffusivities in the liquid state have been made using one of three general approaches. These are the hydro dynamical, quasi-crystalline, and fluctuation theories. A variety of equations are based on the hydrodynamical theories, which relate the diffusion coefficient to the viscosity or to a friction constant, which can then be related to viscosity. A physical interpretation of the diffusivity for spherical solute particles that are large compared to the solvent in which they move is given by the Stokes-Einstein equation [14]. The Stokes-Einstein equation is based on the assumption that the particles are hard spheres that move at a uniform velocity in a continuum under the action of a unit force F. Stokes' law describing the force acting on an atom is

$$F = 6\pi\mu_f r_p u_p \qquad 2\text{-}6$$

Einstein proposed an equation relating the diffusion coefficient to the mobility M as

$$D = k_B T M \qquad 2\text{-}7$$

Since the mobility has units of velocity per unit force, Equation 2-6 and 2-7 can be solved to obtain the equation named Stokes-Einstein equation

$$D = \frac{k_B T}{6\pi r_p \mu_f} \qquad 2\text{-}8$$

where D is self-diffusion coefficient, k_B is Boltzmann's constant, T is absolute temperature, r_p is radius of the diffusing particle, μ_f is liquid viscosity, and u_p is diffusing particle velocity.

Although there are many arguments against this model, its vindication lies in its use as a model that predicts, in a number of cases, diffusion coefficients with the correct order of magnitude.

Several empirical relations have been proposed using the Stokes-Einstein equation as the basic model. Wilke and Chang [15] obtained an equation for predicting diffusivities in dilute solutions of nonelectrolytes

$$D_{AB} = \frac{1.17 \times 10^{-13} (\xi_B M_B)^{1/2} T}{V_A^{0.6} \mu_f} \qquad 2\text{-}9$$

where D_{AB} is inter-diffusion coefficient in dilute solutions, V_A is molar volume of solute at the normal boiling point, M_B is molecular weight of solvent, and ξ_B is association factor of solvent B. Recommended values for ξ_B are: 1.0 for nonpolar solvent, 1.5 for ethanol, 1.9 for methanol and 2.6 for water.

Although the Wilke-Chang equation is not recommended when water is the solute, diffusion coefficients can be predicted to within 11% using water as solvent and to within 27% for organic solvents. Errors greater than 200% are possible when water is used as the solute.

Another equation for predicting diffusion coefficient was developed by Nernst in 1888 [16]. This is the first equation relates the diffusivity of electrolyte solutions to electrical conductivities. His equation, which is valid at infinite dilution, is

$$D_{AB}^{\circ} = \frac{RT}{F_c^2}\frac{\lambda_+^{\circ}\lambda_-^{\circ}}{\lambda_+^{\circ}+\lambda_-^{\circ}}\frac{|Z_-|+|Z_+|}{|Z_+Z_-|} = 8.931\times10^{-14}T\frac{\lambda_+^{\circ}\lambda_-^{\circ}}{\lambda_+^{\circ}+\lambda_-^{\circ}}\frac{|Z_-|+|Z_+|}{|Z_+Z_-|} \qquad 2\text{-}10$$

where F_c is Faraday constant, D_{AB}° is diffusion coefficients at infinite dilution, λ_+° is cationic conductance at infinite dilution, λ_-° is anionic conductance at infinite dilution, Z_+ is cation valence and Z_- is anion valence.

In an electrolyte solution the solute dissociates into cations and anions. Because the size of the ions are different than the original molecule, their mobility through the solvent will also be different. Presumably the smaller ion might diffuse faster than the lager one, however, a separation of electric charge does not occur, so both ionic species must diffuse at the same rate.

Nernst's equation has been verified experimentally for dilute solutions. Selected ionic conductances at infinite dilution are given in Table 2. 1 [17]. An extensive list of values is given by Robinson and Stokes [11].

Table 2. 1 Ionic conductances at infinite dilution in water at 25°C [11, 17].

Cation	λ_+°	Anion	λ_-°
Ag^+	61.9	Br^-	78.4
H^+	349.8	Cl^-	76.35
Li^+	38.7	ClO_3^-	64.6
Na^+	50.1	ClO_4^-	67.4
K^+	73.5	F^-	55.4
NH^+	73.6	I^-	76.8
Ca^{2+}	59.5	NO_3^-	71.46
Cu^{2+}	56.6	OH^-	198.6
Mg^{2+}	53.0	CO_3^{2-}	69.3
Zn^{2+}	52.8	SO_4^{2-}	80.0

2.1.3 Dissolution rate constant

Dissolution rate is the amount of solid substance that goes in solution per unit time under standardized conditions of liquid/solid interface, temperature and solvent composition.

Dissolution rate constant

The definition of dissolution rate is based on empirical arguments like those used in developing Fick's law. In Equation 2-3, the amount of solid transferred into liquid is proportional to the concentration difference and interfacial area. The proportionality is summarized by K_A , called the dissolution rate constant.

The physical meaning of the dissolution rate is: it is the rate constant for moving one species from the boundary into the bulk of the phase [18]. A large value of K_A implies fast mass transfer, and a small one means slow mass transfer. It is written per area relative to an interface, as a result, its dimensions are of velocity, not of reciprocal time.

The dissolution rate quantifies the speed of the dissolution process. It depends on the nature of the solvent and solute, temperature, degree of undersaturation, presence of mixing, interfacial surface area and presence of inhibitors (e.g. a substance adsorbed on the surface).

Dissolution rates vary by orders of magnitude between different systems. Typically, very low dissolution rates parallel low solubilities, and substance with high solubilites exhibit high dissolution rates, as suggested by Noyes-Whitney equation.

Intrinsic dissolution rate

When the dissolution rate of a pure substance is normalized to the surface area of the solid (which usually changes with time during the dissolution process), then it is expressed in kg/m^{2}s and referred to as "intrinsic dissolution rate". The intrinsic dissolution rate is defined by the United States Pharmacopeia.

2.1.4 Convective mass transfer

In accordance with the movement of the liquid surround the solid, the dissolution can be divided into diffusion-dominated and convection-dominated dissolution. Since this process can also be considered as specific types of certain heterogeneous reactions in which a mass transfer is affected through the net result of escape and deposition of solute molecules at a solid surface, such reactions can be classified according to the following three general types [19]:

a. The reaction at the interface occurs much faster than the rate of transport of reactants to and products from the interface. The rate, therefore, is determined by the transport process. In discussion this would be the diffusion or convective transport of solute from the interfacial boundary to the body of the solution.

b. The rate of reaction at the interface is much slower than the transport processes and hence determines the rate. If this is to occur in dissolution, the actual processes of liberation and deposition of the solute molecules at the interface would determine the rate.

c. Both intrinsic rates or rate constants are of the same order of magnitude so that the over-all rate is a function of both process.

The convective dissolution process (also known as transport-controlled dissolution) in a stirred liquid involves both the reaction at the interface and the transport process.

Disagreed with Nernst and Brunner's stationary film layer theory, some researchers' studies indicated that fluid motion and turbulence extends to within a short distance from the solid surface. Van Name and Hill [20, 21] and King [22] proposed that the fluid motion component perpendicular to the surface becomes small and thus does not affect the transport rate materially. Fage and Townend [23] found essentially only laminar motion parallel to the interface existed in regions close to the interface by measuring velocity profiles. These researchers' work lead to a conclusion that convection would aid solute transport only in the distant areas of the film.

A dimensionless number, Sherwood number (Sh) is introduced to represent the ratio of convective to diffusive mass transport. It is defined as

$$\mathrm{Sh} = \frac{KL}{D} \qquad 2\text{-}11$$

where L is the characteristic length.

The Sherwood number for single spheres can be expressed by Frössling equation:

$$\mathrm{Sh} = 2 + 0.552(\mathrm{Re})^{1/2}(\mathrm{Sc})^{1/3} \qquad 2\text{-}12$$

where Re is particle Reynolds number , Sc is Schmidt number.

There are many different expressions that have been developed to calculate the Sherwood number for a spherical particle that work well under different assumptions mainly related to the relative size of the particle and the laminar/turbulent regime inside the stirred tank reactor. Since a specific powder generally has a broad particle distribution and particle size also changes as particle dissolves, an expression that is valid across the full range of particle sizes is needed.

In a well mixed system, the following expression was developed based on Frössling equation:

$$\mathrm{Sh} = 2 + 0.47 \cdot \left(\frac{\rho_f \cdot \varepsilon^{1/3} \cdot d_p^{4/3}}{\mu_f}\right)^{0.62} \cdot \left(\frac{\mu_f}{\rho_f \cdot D}\right)^{0.36} \cdot \left(\frac{d_{impeller}}{d_{tank}}\right)^{0.17} \qquad 2\text{-}13$$

where ρ_f is fluid density, ε is turbulent energy dissipation rate, d_p is particle diameter, μ_f is fluid viscosity, $d_{impeller}$ is impeller diameter and d_{tank} is tank diameter [24].

Another expression for the Sh number used when particles have higher density than the fluid is the following

$$\mathrm{Sh} = 2 + 0.44 \cdot \left(\frac{\rho_f \cdot u \cdot d_p}{\mu_f}\right)^{0.5} \cdot \left(\frac{\mu_f}{\rho_f \cdot D}\right)^{0.38} \qquad 2\text{-}14$$

where u is the relative velocity between liquid and particle [25].

2.2 Factors affecting dissolution

Obviously, in most instances, dissolution of particles is affected by a variety of factors such as the solution in which the solid is dissolving, the temperature and pH value of the solution, and the affinity for the solid particles to dissolve in the solution. There are numerous other factors, such as different ingredients in particles (surfactant, polymers), particle size, and effective surface area of particles exposed to liquid, for which have significant effects on the rate of dissolution.

2.2.1 Physiochemical related properties

Whether particles dissolve or not in a liquid depends on the nature physiochemical properties of particles and liquid. The solubility, diffusivity, particle shape, particle size and particle surface area, all have a different effect on the dissolution process.

Solubility

Solubility is the property of a solid, liquid, or gaseous chemical substance to dissolve in a solid, liquid, or gaseous solvent to form a homogenous solution of the solute in the solvent.

The reasons why a solute may or may not dissolve in a solvent are related to the forces of attraction between the solute and solvent particles. When the forces of attraction between different particles are stronger than the forces of attraction between like particles in the mixture, a solution forms. The strength of each attraction influences the solubility, or the amount of a solute that dissolves in a solvent.

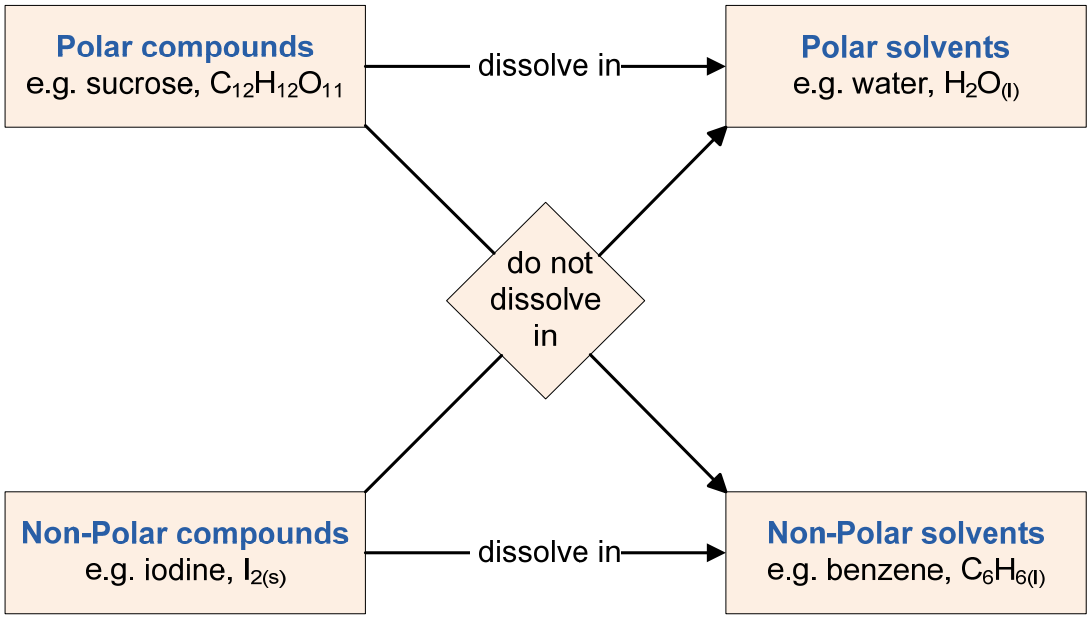

Figure 2. 3 Polar and Non-polar compounds in solution.

The solubility of a substance fundamentally depends on the physical and chemical properties of the used solute and solvent as well as on temperature, pressure and the pH of the solution.

The extent of the solubility of a substance in a specific solvent is measured as the saturation concentration, where adding more solute does not increase the concentration of the solution and begin to precipitate the excess amount of solute.

As predicted by Noyes and Whitney, the dissolution rate is controlled by a layer of saturated solution that forms instantly around a solid particle. In this saturated layer, the amount of solute is the solubility of the solid substance at certain temperature in that solvent. By increasing solubility, the concentration in the saturated layer can be increased, consequently atoms are driven by a higher force due to the bigger concentration gradient between this layer and the bulk solvent.

Diffusivity

In the diffusion layer model, the dissolution rate constant can be related with diffusivity by comparing Equation 2-3 and 2-4:

$$K_A = \frac{D}{\delta} \qquad 2\text{-}15$$

This simplest theory illustrates that the dissolution rate constant is proportional to the diffusion coefficient. Doubling diffusion doubles mass transfer.

The value of D depends on the size of the molecule and the viscosity of the dissolution medium. Increasing the viscosity will decrease the diffusion coefficient and thus the dissolution rate.

Particle shape

Particles come in a variety of shapes and sizes. There are hundreds of shape parameters that are used to describe or represent particle shape. In most cases, the data that scientists use to determine the particle size distribution of their materials assumes that all particles are spheres.

Keith and Bouza dynamically analysed the images of particles during different dissolution stage and used three parameters, smoothness, aspect ratio and equivalent circular area to analyses particle dissolution process [26]. Their research results show that particles become smoother over time.

Jia and Williams used Lattice-Boltzmann method based code *DigiDiss* to model shape effect on particle dissolution [27]. Three different shaped particles with identical surface area dissolve differently. They proposed a reason of spatial distribution of the exposed surface area has an effect on the precise value of C in Equation 2-2.

More recently, Yuan et al simulated the dissolution process of a irregular shaped sugar grain by *DigiDiss* code and observed the process with same sugar grain by optical image analysis [28]. They further discussed the shape effect on dissolution.

The convex parts of particle surface tend to dissolve faster than hollows/gaps on the surface due to the higher diffusion rate and result in round edges and corners.

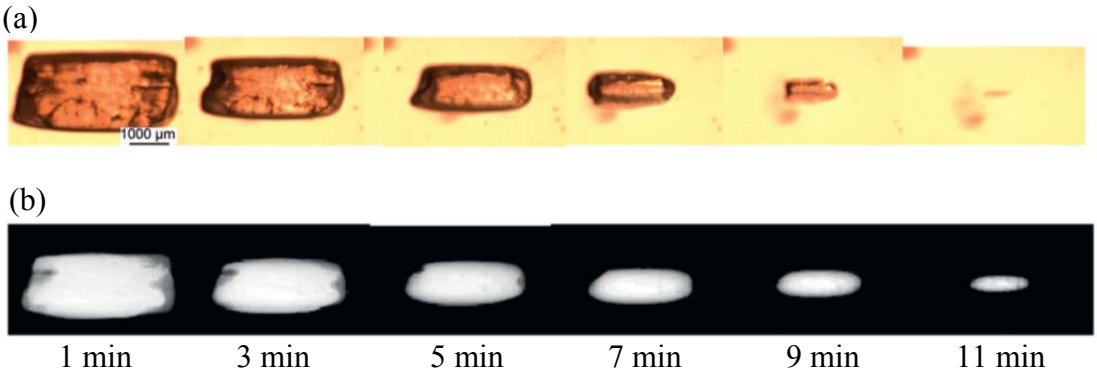

Figure 2. 4 (a) Optical images of a sugar grain dissolving in water at a series of time; (b) projection images of the same sugar grain as simulated by *DigiDiss* [28].

Particle size

Particle size has a significant influence on the dissolution rate. Decreasing the size of the particles increases the rate of dissolving. When a large mass is broken into small masses, the surface area in contact with the solvent increases. This allows the solid to dissolve faster.

According to Brunner's equation, the dissolution rate is directly proportional to the interfacial surface area. Therefore, a decrease in particle size will result in an increase in dissolution rate. However, Bisrat and Nyström has shown that a decrease in particle size results in a higher increase in dissolution rate than can be explained solely by the increase in surface area [29]. In dispersed solid-liquid systems, particle size reduction seems to result in an increase of the dissolution rate of a sparingly soluble material by decreasing the thickness of the diffusion layer around each particle [29, 30] and also by exhibiting a large interfacial surface area [2, 7, 8]. Bisrat and Nyström [29] used the Prandtl boundary layer equation [30] to explain the effect of hydrodynamic boundary layer thickness on the dissolution rate of sparingly soluble materials.

According to the Prandtl boundary layer theory, for solvent flow passing a flat surface, the hydrodynamic boundary layer thickness is proportional to the square root of the length of the surface in the direction of flow l_s, and inversely proportional to the square root of the velocity of the flowing liquid against the flat surface V_s. It is believed that a difference in particle diameter could correspond to a different l_s. Bisrat and Nyström [29] have shown that, for solids dispersed in a liquid medium under agitation, a decrease in particle size probably leads to a decrease in both l_s and V_s. Although these two parameters counteract each other, it was shown that the net effect was a thinner hydrodynamic layer around particles and an increase in the surface specific dissolution rate. This phenomenon is especially pronounced for materials which have a mean particle size less than 5 μm [29].

Later on, Hintz and Johnson took into account of particle size distribution and developed a computer method to describe the theoretical dissolution rate of a polydisperse powder under non-sink conditions based on its percent weight particle size distribution [31].

Then in 1995, Mosharraf and Nyström investigated the combined effects of particle shape (from rounded, isodiametric to flaky or irregular particles) and size (from 1.8 to 3.8 μm) on the dissolution rate of micro sized particles [32]. Their results indicated that the dissolution rates of sparingly soluble drugs are related to the particle shape as well as to the particle size. For particles of the same size, the dissolution rate decreased as the level of flakiness and irregularity increased. This phenomenon can be explained by an increase in the average hydrodynamic boundary layer thickness as the particles become more irregular.

Surface area

It is often preferable that the dissolution rate is expressed in terms of a surface specific value (e.g., in μg/min per cm^2). This can be achieved either by exposing a constant surface area of the solid to the dissolving liquid or by continuously calculating or monitoring the change in surface area, as a function of time. The surface specific dissolution rate is often denoted by G in the literature, and is sometimes also referred to as the intrinsic dissolution rate.

Nicklasson and Brodin [33] postulated the possibility of calculating the maximum dissolution rate of a material from the following equation:

$$\log C_s = \log G + 1.94 \qquad 2\text{-}16$$

Their concept is based on the assumption that the dissolution rate is diffusion controlled. By performing experiments at increasing rotating speeds for a rotating disc they suggested Equation 2-16 was valid for a situation where the diffusional transport could be neglected, i.e., reflecting the maximum dissolution rate.

Particle size and surface area are inversely related to each other. Surface area can be divided into two types, absolute surface area and effective surface area. Absolute surface area is the total surface area of particle, while effective surface area is the area of solid surface exposed to dissolution medium.

The effective surface area is directly related to the dissolution. According to Equation 2-4, the greater the effective surface area is, the more intimate contact between solid surface and aqueous solvent, and hence the faster the dissolution is. It is not certain which area should be used to describe effective surface area. For particles with certain porosity, specific surface area is normally expressed as BET area which includes both internal and external pore areas. Several methods can be

used to measure the surface area of particles, typically BET method Porosimetry. The BET method involves the measurement of the amount of adsorbate or adsorptive gas required to cover the external and the accessible internal pore surfaces of a solid with a complete monolayer of adsorbate. The Porosimetry technique involves the intrusion of a non-wetting liquid (often mercury) at high pressure into a material through the use of a porosimeter. The pore size can be determined based on the external pressure needed to force the liquid into a pore against the opposing force of the liquid's surface tension.

2.2.2 Fluid related properties

Besides the nature physiochemical properties of particle and liquid, the properties of solution also have apparent effects on the dissolution rate.

Temperature

For most solid solutes, the rate of dissolving is greater at higher temperatures. At higher temperatures, the solvent molecules have greater kinetic energy. Thus, they collide with the undissolved solid molecules more frequently. This increases their rate of dissolving.

Solvent temperature has a very significant influence on both solid solubility and dissolution rate. If ideal conditions are assumed, solubility can be estimated using the equation [18]

$$\ln x_B = -(\frac{\Delta_{\text{fus}} H}{R})(\frac{1}{T} - \frac{1}{T^*}) \qquad 2\text{-}17$$

From the energy point of view, increasing solution temperature means adding energy into dissolution system, as a result increases molecular motion. Added energy in the dissolution system increases moving speed of solvent molecules,

makes more of them contact with solute molecules, and pull on them with more force, which eventually resulting in more dissolving.

Since different substances are made from different atoms, ions, or molecules, increasing temperature will affect their dissolving to different extents.

pH value

The dissolution rate of solid in a reactive media is always complicated. Since pH value is one of the factors that influence the solubility of a compound, the pH value of the dissolution medium has a significant effect on the percentage of dissolved active substance. Several conflicting reports have been published by researchers throughout the world.

Brigante et al. [34] analyzed the effect of solution pH on the dissolution kinetics of humic acid particles. Such particles are made by large primary particles which are held together by different interaction forces. By immersing these particles in a dissolving aqueous solution, the forces are weakened and disaggregation takes place which enhances the dissolution process. Their results reflects the strong effects of pH on the dissolution rate of humic acid particles due to reactions that take place at the surface of particles. In Figure 2.5 (a) α is release percentage, and in (b) R is dissolution rate.

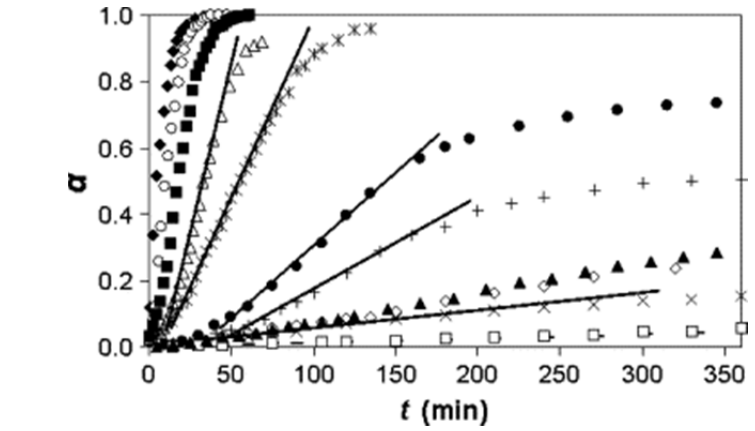

(a)

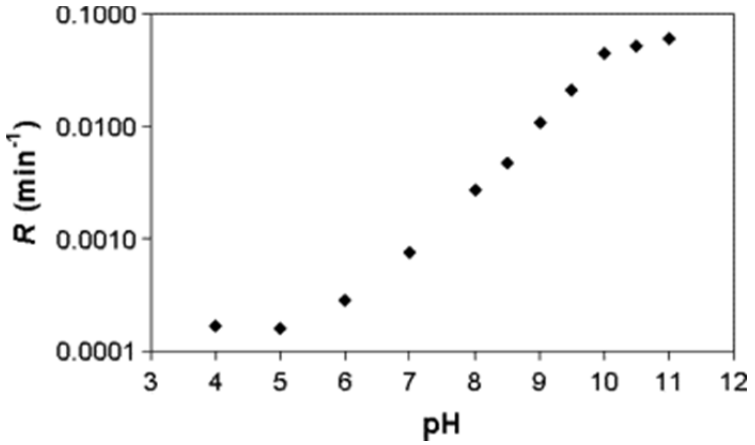

(b)

Figure 2. 5 Effect of pH on (a) the dissolution curves and (b) dissolution rate of the studied particles[35]. For (a), pH: solid diamonds, 11; open circles, 10.5; solid squares, 10; open triangles, 9.5; stars, 9; solid circles, 8.5; plus signs, 8; open diamonds and solid triangles, 7; crosses, 6; slashes, 5; open squares, 4.

Serajuddin and Jarowski systematically investigated the mechanism of the dissolution of pharmaceutical acids and their sodium salts by correlating their pH-dissolution rate profiles with their pH-solubility profiles [36, 37]. When the solubility values under pH conditions, the diffusion layer thickness δ approaches zero ($C_{s,\delta=0}$) were used rather than solubilities under pH conditions of the bulk media (C_s), good conformity with Noyes-Whitney equation was demonstrated and a simple method was developed to predict the dissolution rate of an acid or a salt at different pH values.

Agitation

Agitating a mixture by stirring or by shaking the container increases the rate of dissolving. Agitation brings fresh solvent into contact with undissolved solid.

Some of the investigation involving agitation have led to the empirical relationship:

$$K = a(N)^b \qquad 2\text{-}18$$

where N is the agitation, a and b are constants. If the dissolution is diffusion controlled, then the value of b should be 1 or near 1. This is in accord with the Nernst-Brunner film theory [7], which stated that the thickness of the film was inversely proportional to the stirring speed. For the dissolution controlled by the rate of the interfacial reaction, it would be expected that the agitation intensity would not influence the reaction rate, and b should approach zero. If both processes are influential in the control of the rate, b should vary between zero and 1 if a sufficiently wide range of agitation intensities are employed.

Inasmuch as the motion of the fluid changes from laminar to turbulent as the distance from the interface increases, the value of the exponent b also may vary with the type of agitation used. Hixon and Baum [38] observed this when they employed measurements obtained on the dissolution of benzoic acid pellets as criteria for agitation efficiency. By a dimensional analysis they assigned a Reynolds number to the point where the relationship between the variables changed. They attributed this change to the turbulence and obtained separate relationships for high and low Reynolds number values. In a subsequent study [39], by changing only the type of stirring, they found that another empirical relationship must be assigned.

In 1975, Nelson and Shah proposed a convective diffusion model (see Figure 2.6) for a transport-controlled dissolution rate process [40] and verified by a rotating-

filter-stationary basket experiment. Combining diffusion and convection, a mathematical expression for mass transport was developed to give a "convective diffusion" differential equation. By selecting appropriate boundary conditions and solving the differential equation utilizing these boundary conditions, an expression for the dissolution rate was developed and verified experimentally. For a rectangular tablet of length L_T (in the direction of flow) and width b_w, initial dissolution rate K was written as

$$K = 0.808 D^{2/3} C_s \dot{\gamma}^{1/3} b_w L_T^{2/3} \qquad 2\text{-}19$$

For a circular tablet of radius r, K was written as

$$K = 2.157 D^{2/3} C_s \dot{\gamma}^{1/3} r^{5/3} \qquad 2\text{-}20$$

where $\dot{\gamma}$ is the shear rate in the boundary layer.

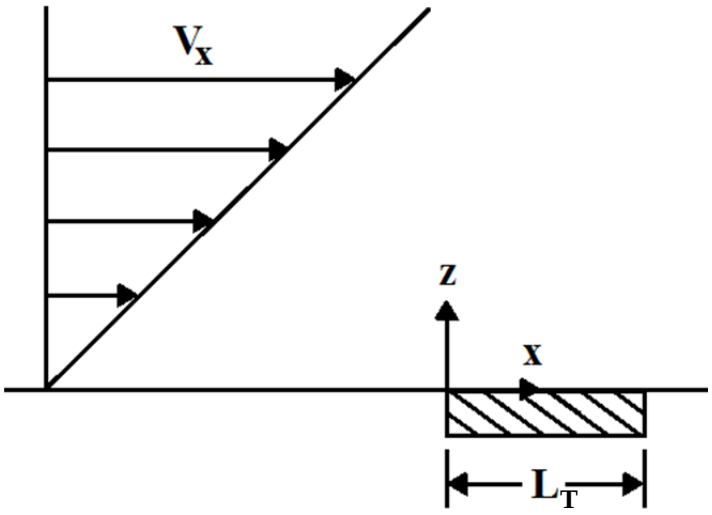

Figure 2. 6 Convective diffusion model [40].

2.3 Dissolution of structured particles

For a porous granule, its dissolution behaviour depends on the solubility of granule ingredients in a given liquid. According to this parameter, particles can be simply

divided into two types, dissolvable and non-dissolvable. However, most granules in modern industry contain different chemical ingredients which have different solubilities. Meanwhile, the multi-ingredients granules are often in the forms of porous media. In this case, the dissolution kinetics is very much different from one ingredient solid particle dissolving in liquid, it is much more complicate.

The dissolving process of solid particles in liquid can broadly be divided into two steps: the escape of solute molecules from the solid surface and the diffusion of these molecules toward the bulk liquid phase [1]. For a porous medium, for example washing powder, the dissolving of active ingredients consists of several steps (see Figure 2.7): i) wetting of granules followed by penetration of liquid into pores in the granules due to capillary forces; ii) immersion of the granule into the liquid; iii) the dissolution of the solid bridges between the primary particles followed by the dispersion of the primary particles within the liquid; and iv) the dissolution of soluble primary particles [41].

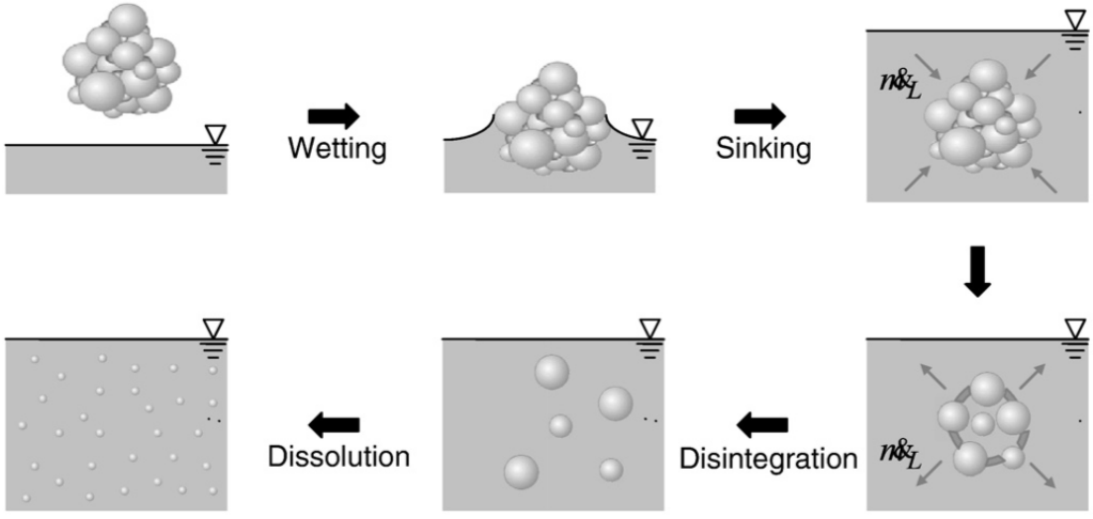

Figure 2. 7 Schematic diagram of agglomerate dissolution [41].

It is important to note that in real processes these steps are difficult to be clearly isolated from each other. They may not happen sequentially, but rather occur

simultaneously, and affect each other. Therefore, analysis and modelling of these processes remains difficult.

2.3.1 Capillary filling of liquid into porous granules

Capillary filling is the ability of liquid to flow against gravity where liquid spontaneously rises in a narrow space such as between the hairs of a paint brush, in a thin tube, in porous materials such as paper or in non-porous material such as liquefied carbon fibre. It occurs because of inter-molecular attractive forces between the liquid and solid surrounding surfaces.

Modern detergent powders usually can be taken as porous media. The first stage of a washing powder dissolving in water is the penetration of water into the powder through pores connecting to the surface. The first step in the process of dissolution is wetting of the dissolving surface, which is in contact with the dissolution medium. The condition for complete wetting of a solid surface is that the contact angle should be zero.

There are two different types of pores, close-ended pores which only extend into the centre to a certain depth, and open-ended pores which connect inside the granules and form a channel network. Once a granule sinks into water, water will penetrate inside it due to the capillary force from both close-ended and open-ended pores [42].

As applied to a viscous noncompressible liquid in a long cylindrical capillary, the Newton dynamics equation can be expressed as

$$\rho[hh'' + (h')^2] = \frac{2}{r}\gamma\cos\theta - \frac{8}{r^2}\mu hh' - \rho gh \qquad 2\text{-}21$$

where ρ is the density, μ is the viscosity, γ is the surface tension, θ is the wetting angle of the liquid, h is the height of capillary rise, r is the capillary

radius, and g is the acceleration of gravity [43]. The equation assumes the Poiseuille flow profile throughout the capillary. The capillary liquid will rise to a equilibrium level h_{eq}, established by the balance of gravity and capillarity,

$$h_{eq} = \frac{2\gamma \cos\theta_{eq}}{\rho g r} \qquad 2\text{-}22$$

where θ_{eq} is the equilibrium contact angle [44]. By measuring the equilibrium height of each penetration through the video of high speed camera, using Equation 2-22, θ_{eq} can be calculated.

Neglecting variations of the dynamic contact line with speed, and assuming it constant equal θ to the equilibrium contact angle θ_{eq}, Lucas and Washburn [42, 45] obtained capillary penetration equation for vertical tubes as

$$h = \sqrt{\frac{\gamma r}{2\mu} \cos\theta_{eq} t} \qquad 2\text{-}23$$

in which, the height of capillary rise $h^2 \propto t$. It is well known that in this equation, some terms for example the gravity effect, the kinetic effect, the viscous loss in liquid below the tube, and the viscous loss associated with the entrance effect, have been neglected [46]. Consequently, this equation cannot be used for the initial capillary dynamics.

2.3.2 Dissolution of soluble ingredients in granules

Modern detergent granules can be considered as an object consisting of constituent particles held together by a binder. Such granules contain several water soluble components and three main ingredients are builders (~ 50 wt %), alkylbenzenesulfonate surfactant (~15 wt %), and bleaches (~ 7 wt %) [47]. Typical

builders are sodium carbonate, sodium triphosphate and sodium sulphate. Most bleach in washing powder is oxidizer, e.g., sodium perborate or sodium hypochlorite. Granules can have different structures, one is that builders act as a core and the rest ingredients layer coating outside, and the other is that the granules are formed from a mixture of all ingredients. Upon sunk in water, the water soluble ingredients dissolve into water from both inside and the surface, depending on the structure of granules, primary particle size, water penetrating rate, dissolution rate of each of the ingredients and their interactions. However, which factor dominates the dissolution process and how interactions take place remains scientific challenges. This makes various industrial sectors particularly enthusiastic to investigate these phenomena.

2.3.3 Granule disintegration

According to the binder type, granules can be broadly divided into three types. The first type is that constituent particles are held together by micro-scale forces, typically van der Waals forces, and this type of granules is termed binderless granules. The second type is that the constituent particles are held together by solid bonds (solid bridge), and this type of granules is named as solid granules. The third type is that a granule contains liquid interstitially, which is the so called wet granules [48]. Of course, drying of the wet granules can give either the first type or the second type granules, these types of granules are expected to exhibit different disintegration behaviour due to the different nature of the particle binding forces.

Once granules sink into water, the water soluble constituents including binders dissolve simultaneously but different rates, depends on various factors such as binder type, binder content, primary particle size and shape, pore structure and

granule homogeneity. After a certain time, granules break into smaller agglomerates or primary particles.

2.4 Experiment method of dissolution

In the past centuries, the experiment of dissolution has developed into a very commercial aspect. Two basic techniques, stirred beaker method and flow through procedure, as long as some other non-official apparatus have been evolved for dissolution testing.

2.4.1 Stirred Beaker Method

The most common dissolution apparatus used throughout the world are (1) the basket method and (2) the paddle method. This system places the test specimen and a fixed volume of fluid in a vessel, and stirring provides mechanical (hydrodynamic) agitation. It was adopted as the official dissolution method in United States Pharmacopeia (USP) XVIII in 1970 and described as the rotating basket method, USP Apparatus 1. Then the rotating paddle method was adopted as an official dissolution method by the USP several years later and became the USP Apparatus 2.

These methods are simple and robust and are generally flexible enough to allow dissolution test for a wide variety of products. For this reason, Apparatus 1 and 2 are recommended for dissolution method development.

A typical PTWS 610 testing equipment is shown in Figure 2.8. By switching correspondingly shafts, the equipment can be used as 2.9 (a) Rotating Basket Method and 2.9 (b) Rotating Paddle Method. Two different vessels are normally used in rotating basket method, the hemispheric shaped vessel and peak vessel as shown in Figure 2.10.

Figure 2. 8 Six vessel dissolution test apparatus [49].

(a) (b)

Figure 2. 9 (a) Rotating Basket Method and (b) Rotating Paddle Method [49].

Figure 2. 10 On the left are hemispheric shaped vessel made of glass or suitably inert material, 4-Liter, 2-Liter, 1-Liter, 500mL. On the right is peak vessel with an inverted peak incorporated into the bottom of the vessel [50].

2.4.2 Flow Through Procedure

The flow-through system was first adopted by the Deutscher Arzneimittel codex (German Pharmaceutical Codex, DAC) in 1981. Later on two new apparatus were added to the USP in 1990 to overcome some of the experimental difficulties from the use of the single vessel method: Reciprocating Cylinder which is USP Apparatus 3 and Flow-through Cell which is USP Apparatus 4.

Some of the needs for the flow-through type apparatus included a change of pH or any other change in the dissolution medium. Difficulties had also arisen for a number of sparingly soluble drugs which were difficult to investigate with a limited volume of media.

2.4.3 Other dissolution test apparatus

Other dissolution test apparatus categorized by USP as Paddle Over Disk, Rotating Cylinder, and Reciprocating Holder Apparatus are used in a variety area. These apparatus were originally designed and are primarily used for analyse of transdermal delivery systems. Some other unofficial apparatus such as Rotating Bottle and Diffusion Cells are also used for certain circumstance.

2.5 Simulation of dissolution

The simulation of structured particles dissolve in a solution is very complex due to the versatile particle shape, size, ingredient and porosity etc. all might affect the dissolution in a different way. A more practical method is to investigate different steps separately during particle dissolution as Forny et al. [41] described in Figure 2.7.

The first step in the process of dissolution is wetting of the dissolving surface, which is in contact with the dissolution medium. The second step is particle disintegration which should happen as the binders dissolve into solution medium. The last step is particle dissolution. Different numerical methods can be introduced to simulate these steps. A combining model of all the steps is more desirable but too challenge for current numerical simulation conditions.

2.5.1 Modelling of water filling in porous media

The initial stage of granule dissolution involves water penetration into pores due to capillary force. Such a phenomena is associated with the transport phenomena in porous media, which has attracted the attention of many theorists and experimentalists in recent years, due to numerous applications in many engineering and technological areas [51]. Despite the importance, physically and mathematically rigorous equations have not been clearly formulated for the transport phenomena in porous media, especially for multiphase system. As a result, empirical or semi-theoretical relationships have been proposed.

Simulation of water penetration into porous granules must begin with a physical model that captures the main features of flow. Such a physical model will no doubt affect the appropriateness of mathematical formulation and a subsequent numerical model.

From the physics point of view, pore filling process in granules can be regarded as a multiphase flow in a porous medium in which water is one phase, air originally inside granules is another phase, and solids particles made up the granules are the third phase. Numerical simulations of multiphase flows in porous media were originally done with the finite difference scheme, and then finite volume and finite

element methods were used. Followed by recent research upsurge in Lattice-Boltzmann method (LBM), researchers have introduced this method into a variety of applications, one of which is multi-phase flow in porous media.

Network models

Using numerical networks to represent pore structure is the most popular method for theorists to simulate liquid penetrating into porous media [52-61]. These simulations are welcomed by experimentalists in idealized two-dimensional porous media[55, 62-65], where different pore-scale displacement mechanisms could be seen. By using a numerical network to represent the pore structure, researchers can demonstrate a simple site.

The first step to describe a fluid flow system is to define the geometry of the medium, the outlets, the inlets and their flow rates. The fluid flowing into the system is named the new fluid or the invasion fluid [66, 67] and the resident fluid is called the old fluid or the defender fluid. In a network model, new fluid begins to conquer the nearest points of the mesh and push out the resident fluid.

Fatt and Aime (1956) were the first to report the use of network of tubes as a model to represent porous medium. In their work, capillary pressure curves were derived from such a model in order to calculate pore size distributions for porous media [52]. The “pores” roughly corresponded to the larger voids whereas the throats connecting the pores corresponded to the constrictions of the pore space (Figure 2.11).

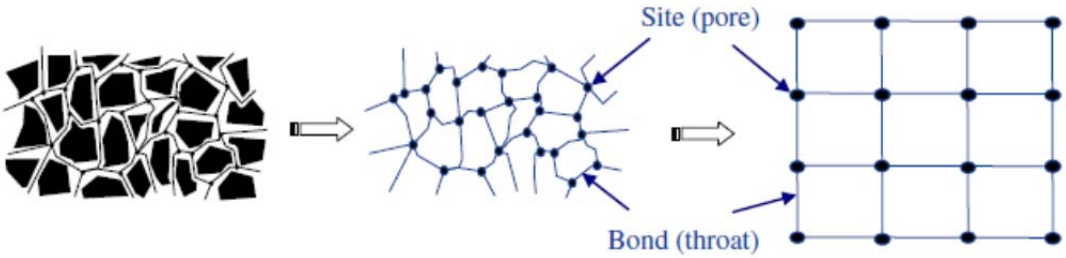

Figure 2. 11 Modelling of pore space by a network of pores (sites) and throats (bonds) [68].

Another way to simulate fluid flow is to create a computational representation of the porous media and then calculate the fluid displacement by solving fluid flow equations as a function of the medium properties. This process was illustrated by Ramirez et al [69] to simulate fluid flow through anisotropic material like filters, membranes, walls, oil reservoirs, etc (see results in Figure 2.12). The equation of conservation was used to solve the distribution of the fluid as a function of the new fluid received and the excess of fluid on saturated capacity was redistributed.

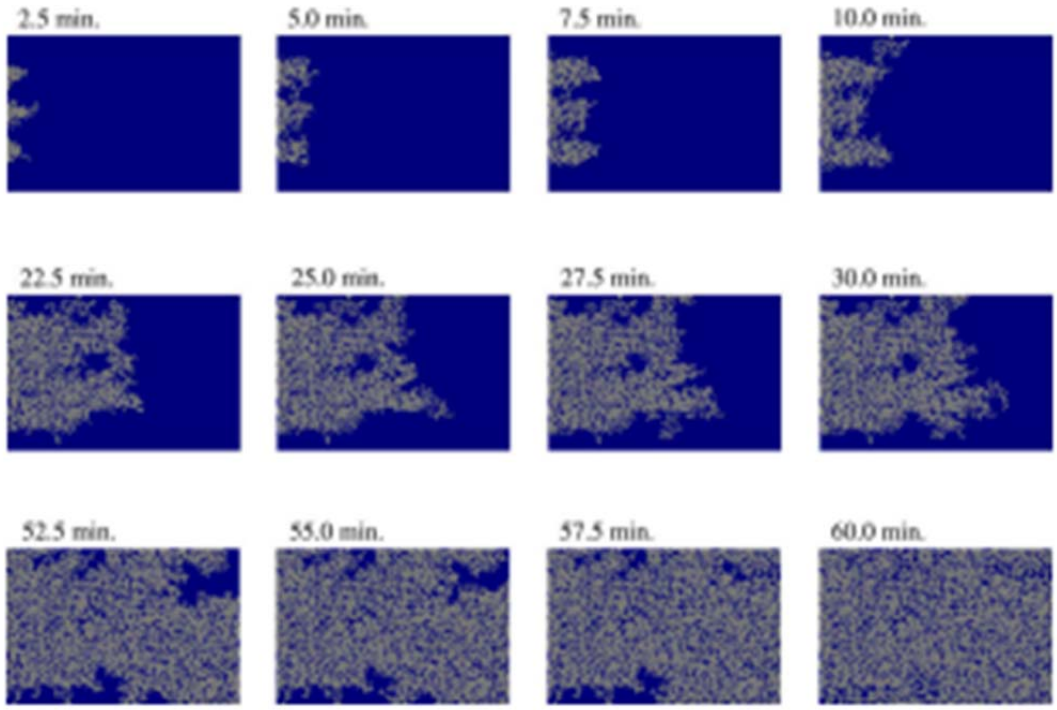

Figure 2. 12 Evolution of the fluid injection inside porous medium [69].

Whilst the displacement mechanisms in modelling 2D experimental porous media are well established, there is still considerable confusion in the literature if the appropriate flow behaviour in 2D medium is able to represent the flow in 3D porous medium.

Lin and Slattery developed a structural model for a porous medium in the form of a randomized 3D network [70]. Such a model, used seven free parameters, was shown to be able to calculate permeability, the drainage and imbibitions capillary pressure, and correlate successfully to the literature data for 100-200 mesh sand, uniform 181 μm glass spheres, and a bed of sintered 200 μm glass beads.

Finite difference and finite element methods

The finite difference approach involves dividing the system under investigation into network of elements, and a set of finite difference equations for the flow into and out of each element can then be developed. As the whole calculation domain is divided into elements, the solution usually requires a high speed computer. For heterogeneous systems with an arbitrary geometry, sometimes this method is too difficult to use and a large amount of computing time may be required.

The finite element method (FEM) was originally developed to solve problems of stress distribution in extremely complex airframe configurations for the aircraft industry [71]. Zienkiewicz et al (1966) were among the earliest to introduce FEM to obtain the steady-state solution to heterogeneous and anisotropic seepage problems [72], later Taylor and Brown (1967) used the method to investigate the steady-state flow problems involving a free surface [73]. Following the work of Gurtin who applied the FEM to the linear initial-value problem [74], Wilson and Nickell extended FEM to transient heat conduction problems [75], and finally, Javandel and

Witherspoon extended the method further to study the transient flow in porous media [76].

In later 1990s, Lewis and Ghafouri developed a mathematical model for multiphase flow through deformable fractured porous media through coupling the governing equations, consisting of the equilibrium and continuity equations in both the fluid phase and the solid phase. In such a model, the solid displacement and fluid pressure are considered as the primary unknowns and may be used to determine other solid parameters such as stresses, saturations, etc [77].

Huber and Helmig compared the classical finite element method and the mixed-hybrid finite element method for modelling multiphase flows in porous media [78], and the results suggested that for cases with large changes in the capillary pressure, the mixed-hybrid finite element method was not suitable. If the changes of the pressure field with respect to the time were small and convective processes were dominant, the method was found to be an efficient choice.

Lattice Boltzmann method

Recently, the LBM has developed into a very promising method for modelling fluid flows and physics in fluids, particularly wherein the system includes interfacial dynamics and complex boundary conditions. LBM uses microscopic models and mesoscopic kinetic equations to incorporate the essential physics of microscopic or mesoscopic processes in order to make the macroscopic averaged properties obey the desired macroscopic equations, which is different to conventional numerical methods based on discretizations of macroscopic continuum equations. As using these simplified kinetic methods, LBM is based on the assumption that the dynamic properties of a fluid can be represented by calculating the whole behaviour of many

microscopic particles in the system and that the macroscopic dynamics is insensitive to the related details in microscopic physics [79].

Lattice Boltzmann multiphase fluid models have been extensively used to simulate multi-component fluid flowing through porous media in order to understand the fundamental physics [80]. This is because LBM is particularly capable of complex geometrical boundary conditions and varying physical parameters, such as viscosities [81] and wettabilities [82]. Martys and Chen [83], Ferreol and Rothman [84], used realistic sandstone geometries from oil fields to observe complicated flow patterns. Their numerical values of the relative permeability as a function of percent saturation of wetting fluid agree with experimental data.

By including the porosity into the equilibrium distribution, and adding a force term to the evolution equation to account for the linear and nonlinear drag forces of the medium, Guo and Zhao [85] proposed a lattice Boltzmann model for isothermal incompressible flows in porous media. Through the Chapman-Enskog procedure, a generalized set of Navier-Stokes equations for incompressible flow in porous media were derived from the present lattice Boltzmann model. Such a model is applicable for a medium with either constant or variable porosity cases, and can be used to solve transient flow problems.

With rapid developments in the computing power, extremely complicated cases can now be handled more accurately. For example, Sullivan et al [86] recently applied a variant of LBM to model non-Newtonian fluids flowing through random complex porous media in 3D. The accuracy to the lattice resolution was related and the results compared very well over a wide range with a known analytical solution for macroscopic flows of power-law fluids through porous media.

2.5.2 Modelling of particle disintegration

Disintegration is a general phenomenon normally happens during the dissolution process of porous particles. As reviewed previously, dissolution rate is strongly related to particle size. Once disintegration happens, particle breaks into smaller size, as a result, dissolution process can be accelerated.

To simulate disintegration, particles have to be treated as discrete elements, meanwhile, liquid needs to be treated as continuous phase. Discrete Element Method (DEM) is a quite popular method for modelling particle breakage [87-91]. Computational Fluid Dynamics (CFD) is the most popular method for simulating fluid [92]. In recent years, the so-called combined CFD and DEM, abbreviated as CCDM, has been developed to simulate gas-solid and liquid-solid systems where fluid–solid phase interface cannot be negligible [93]. It could be a promising method to model particle disintegration during the dissolution process.

Discrete element method

The granular medium usually is not homogeneous and has a discontinuous structure where interaction only occurs at contact part between primary particles [94]. Hence, DEM can be a fundamentally suitable tool to study the macroscopic behaviour of particulate systems, which depend on the discrete behaviour of their constituent primary particles. Impact breakage of granules is one of the examples that DEM simulation can be used to assist more fundamental understanding. The evolution of the structure of a granule impact can be modelled as a dynamic process by tracing the motion of the constituent particles in the granule throughout the impact event using Newton’s law of motion [87].

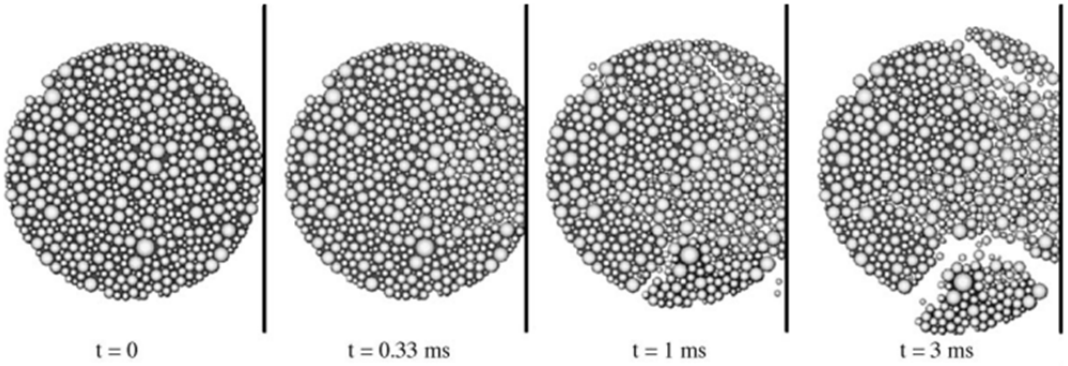

Figure 2. 13 DEM simulation of granule impact breakage [87].

CFD-DEM

The CCDM method treats the solid phase (particles) as a discrete element, and the fluid phase (gas or liquid) as a continuum. In such a method, the motion of individual particles is tracked by using Newton's second law of motion, while the fluid flow is solved by integrating the locally averaged Navior-Stokes equation [95-97].

The CCDM approach has proven to be effective in modelling particle-fluid flow. It provides detailed dynamic information, such as particle trajectories and transient forces acting on the individual particles. The forces that can be considered are briefly outlined in the following.

Collisional Force The collisional force arises from direct particle-particle collisions, which are accompanied by the deformation of the particles at contacts. The deformation is represented by the overlaps of the particles at the contacts. The most intuitive model to relate the overlaps to contact forces is the linear spring-dashpot model [98], where the spring represents the elastic contribution to the contact while the dashpot accounts for the energy dissipation by the plastic deformation, as shown in Figure 2.14. In the tangential direction, a limiting condition occurs when the

tangential force exceeds friction force. In such a case, the particle slides over the contact surface.

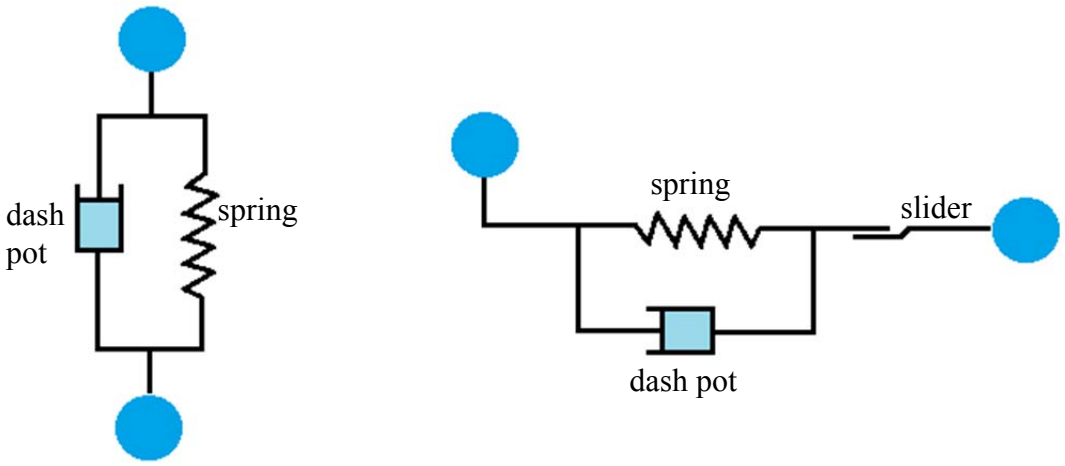

(a) (b)

Figure 2. 14 Models of contact forces: (a) normal force, and (b) tangential force.

Cundall and Strack (1979) represented the kinetic energy loss due to the plastic deformation by the so-called damping force, which is the product of a damping coefficient and the displacement. Tsuji et al [99] showed that for a given coefficient of restitution (e) the damping coefficient (η) can be given by:

$$\eta = 2\sqrt{\frac{mk}{\left(\frac{\pi}{\ln(e)}\right)^2 + 1}} \qquad 2\text{-}24$$

where m is the mass of the particle, and k is the contact stiffness.

Other contact models are also reported in the literature, which have a greater complexity. Most of these models are based on Hertz's theory [100] for the contact in the normal direction and Mindlin-Deresiewics model [101] for the contact of in the tangential direction. Hertz's theory considers a nonlinear relationship between the normal stress and normal displacement; see for example Thornton and Yin [102]. The theory, however, neglects adhesion force between the contacting

particles. This could be accounted for by either the JKR model [103] or DMT model [104]. The JKR and DMT models assume elastic deformation as the only contact mechanics, however it may not be true when plastic deformation is not negligible. More recent normal contact models that considered plastic deformation have been developed [105, 106].

Drag Force The drag force arises from the frictional interaction between the fluid and the particle phases as well as the unbalanced pressure distribution when two phases have different velocities. For a single, isolated sphere, in a Stokesian flow regime, the drag force can be calculated from the well-known Stokes-Einstein equation. For liquid-solid flows where the drag force is influenced by the neighbouring particles, lots of research has been carried out. These studies have led to many drag force relationships. These drag force relationships can be categorized into two categories. One is empirical based, for example Ergun [107], Wen and Yu [108], Di Felice[109], and Mazzei and Lettieri[110] equations. The other is through mathematical modelling using direct numerical simulation (DNS) [111].

The empirical correlations can be sub-divided into two groups. The first group is based on the expression for the drag force in the limit of Stokes flow with an extra term added to account for inertial effects [107]. The second group is based on the expression for the drag force on a single particle at various flow regimes. The presence of other particles was accounted for by a voidage function [109] expressed as $\varepsilon^{-\alpha}$, where the exponent α was regarded as a constant by some researchers [108]. However, others [109] suggested that α is a function of particle Reynolds number. Mazzei and Lettieri[110] compared different methods for determining the α value. They concluded that these drag force relationships usually have a lack of general validity: some of them are limited to certain fluid dynamic regimes; others

only work for a restricted particle concentration range. Authors proposed a new drag force relationship with α depending on both the particle Reynolds number and voidage, which extended the applicability to the whole range of fluid dynamic regimes and for any value of the fluid volume fraction.

Lift Forces Lift forces include Saffman lift force and Magnus lift force, which become important when a particle moves in shear flows such as in the boundary layers where there is a velocity gradient or pressure gradient [112]. Saffman force is caused by the pressure distribution induced by the velocity gradient [113]. The Magnus force is developed by the pressure difference on the surface of the particle, which causes particle rotation and hence a lift force. In slow flows, particle rotation causes fluid entrainment, resulting in an unbalanced velocity profile. The velocity on one side of the particle is greater than that on the other side. This effect causes the particle moves toward the region of higher velocity [114].

2.5.3 Modelling of particle dissolution

The moving boundaries (also known as Stefan problems) are always big challenges of numerical modelling of dissolution. Difficulties in tracking the motion of the interface arise because of the discontinuity in the concentration profile there.

By developing their own codes, researchers have invented different models to simulate the dissolution process of particles. Franstisek Stepanek from Imperial College London constructed a three-dimensional virtual granule model with varying porosity and binders [115]. The model is based on a vector approach, using a surface mesh to represent particle geometry and conventional CFD to calculate the flow. By gradually eroding material from the granule surface, the effective dissolution rate of the granules has been determined by the phase functions, density, solubility and

diffusion coefficient in water (at a given temperature) of each component. The granule dissolution profile is obtained by the solution of the diffusion equation for each species in the liquid phase in and around the granule (Fick's diffusion is considered).

Later on, they further modified their model by introducing two granule design methods Stochastic design method and variational design method into their virtual granule generation steps, hence constructed more complex microstructures[116]. By comparing their simulation result and experiment result, they found out that despite the effects of particle size, radial distribution of components within the granule, granule composition and porosity, granules with a structure of primary particles surrounding by binders dissolve slower than those directly exposed to solution. Their research is directionally valuable for industrial granule design, however they did not present quantitative comparison between their modelling results and experimental results.

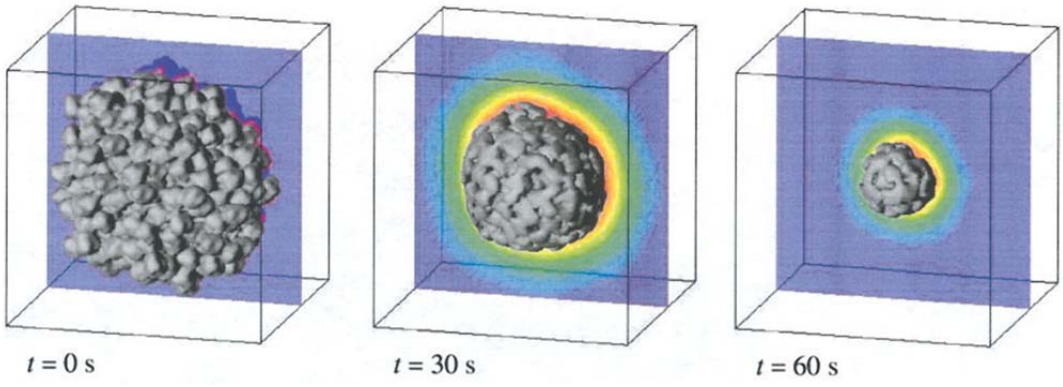

Figure 2. 15 Illustration of the simulation of diffusion-limited dissolution of a virtual granule [116].

LBM are powerful techniques for arbitrarily shaped boundaries and multi-component systems. Kang et al developed a lattice Boltzmann model for simulating the transport and reaction of fluids in porous media. They took into account of the interaction of forced convection, molecular diffusion and surface reaction [117]. In

their model, the evolution of the porous media geometry due to chemical reaction was illustrated and their simulation results suggest that LBM may serve as an alternative reliable quantitative approach to study chemical dissolution in porous media.

By imposing equilibrium concentrations on the interfaces, Arnout et al developed a two-component lattice Boltzmann model [118]. The phases are treated as different computational domains with sharp phase boundaries, captured using a volume-tracking scheme.

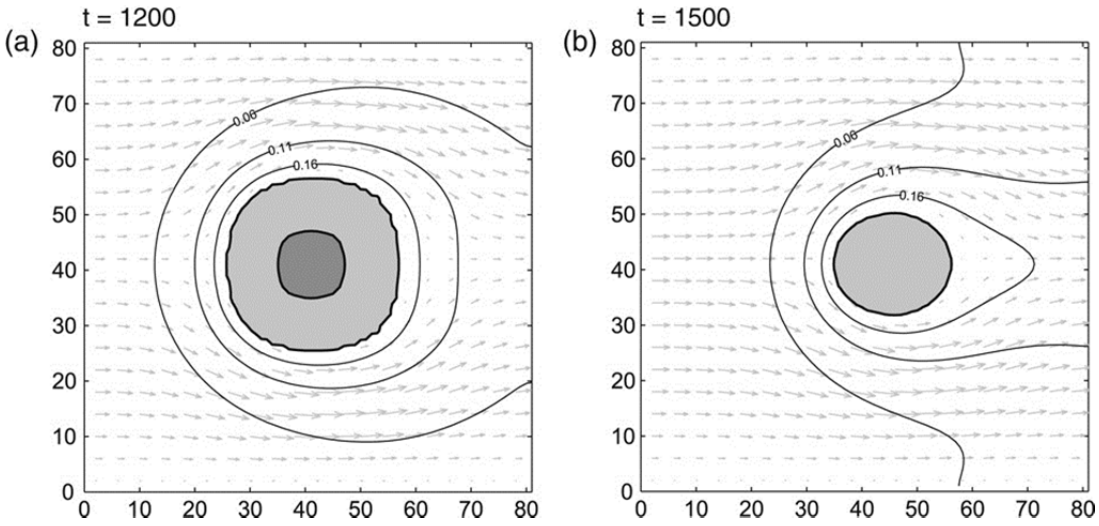

Figure 2. 16 Dissolution of a square box in a channel for $\mathrm{Sc} = 6.7$ **after (a) 1200 and (b) 5000 time steps [118].**

Combining X-ray microtomography (XMT) and LBM, Jia et al. developed a code (known as *DigiDiss*) which can simulate particle dissolution by importing real particle shape scanned from XMT into LBM[119]. The structure is described in a lattice grid which is also used by the LBM simulation. With the finite difference method, the same grid can be used to solve governing equations for dissolution:

$$\frac{\partial C}{\partial t} + (u_x \frac{\partial C}{\partial x} + u_y \frac{\partial C}{\partial y} + u_z \frac{\partial C}{\partial z}) = D(\frac{\partial^2 C}{\partial x^2} + \frac{\partial^2 C}{\partial y^2} + \frac{\partial^2 C}{\partial z^2}) \qquad 2\text{-}25$$

$$\frac{dW}{dt} = -KS(C_s - C) \qquad 2\text{-}26$$

Equation 2-25 is the convection-diffusion equation [120] that describes the concentration distribution in a liquid. (u_x, u_y, u_z) is fluid velocity components and (x, y, z) is spatial coordinates. Equation 2-26, Noyes-Whitney equation is used at the solid/liquid interface.

In this code, discretization of Equation 2-25 is performed following bottom-up finite difference schemes based directly on mass balance, Fick's first law and the Noyes-Whitney equation in a lattice grid cell. And the concentration is updated explicitly at each time step.

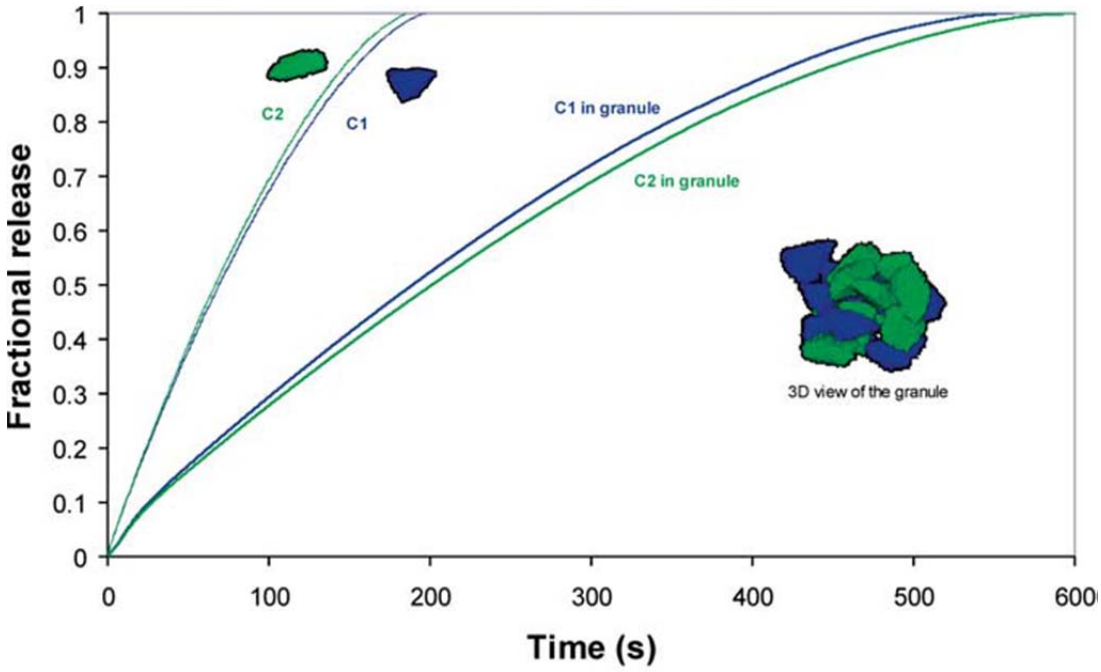

Figure 2. 17 Simulated dissolution profile of standalone component particles and their agglomerate under diffusion-only conditions [27].

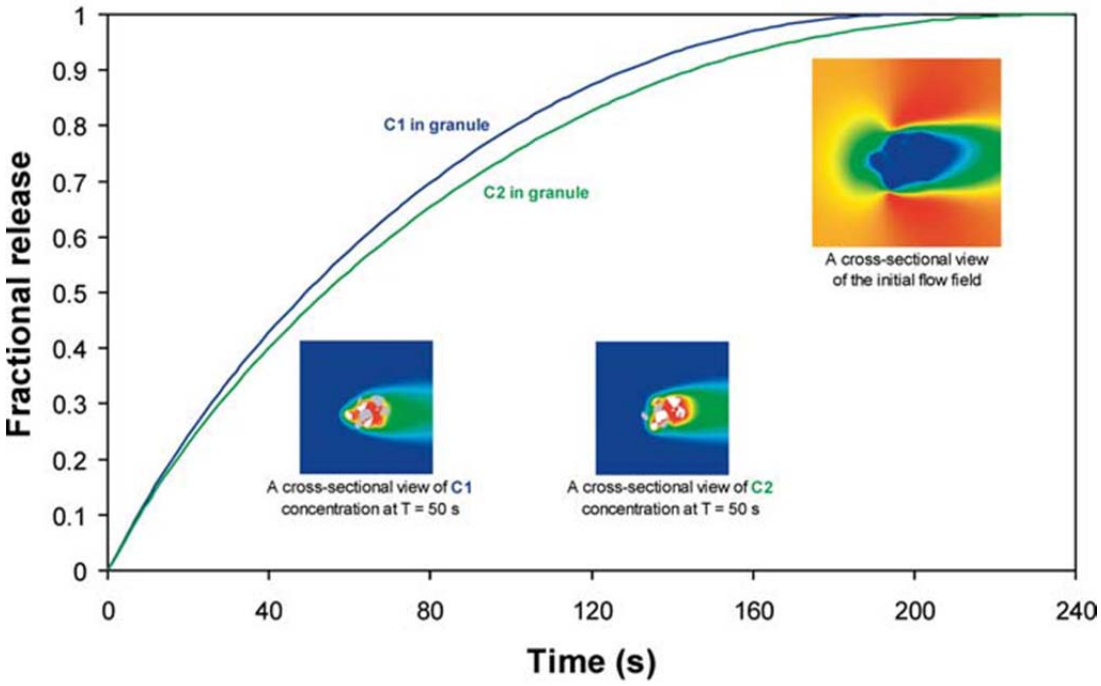

Figure 2. 18 Simulated dissolution profiles of the constituent components of the same agglomerate under flow conditions[27].

More recently, this code was validated by comparing simulation results to experimental results. Single crystals and the cluster were first scanned using XMT to obtain a digital version of the structures and then inputted to their code to run dissolution simulation. Meanwhile, the same particles were dissolved in water and the dissolution process was recorded by video camera and analysed yielding: the overall dissolution times and images of particle size and shape during the dissolution [28].

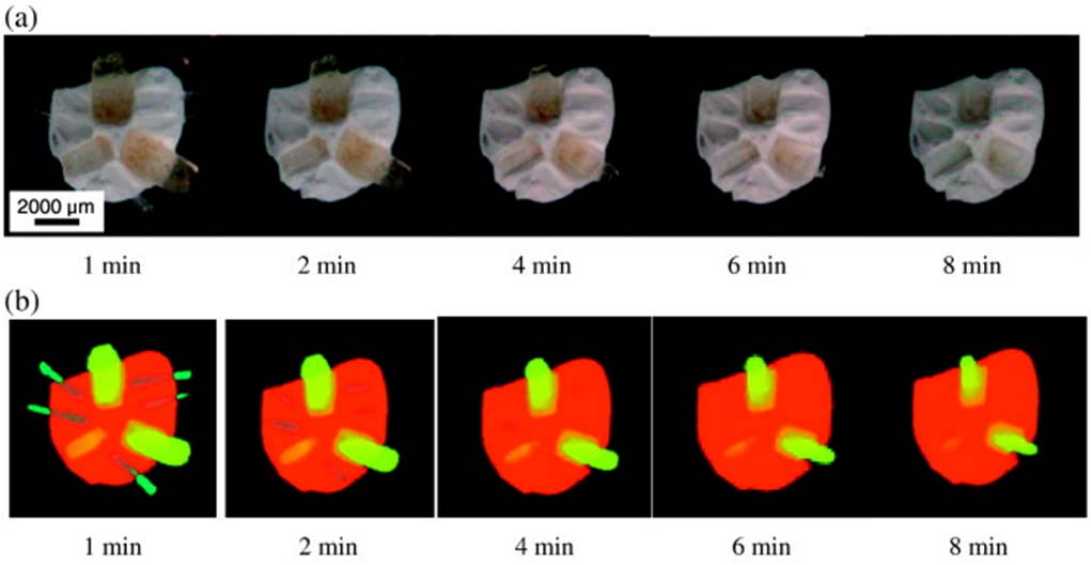

Figure 2. 19 (a) Optical images of dissolution process of a particle cluster of sodium monoglutamate crystals and brown sugar particles granule in water; (b) simulated dissolution process of the cluster structures [28].

CHAPTER 3
METHODOLOGY

The aim in this thesis is to build up a mathematical model to predict porous particle (detergent powder) dissolution in water. It is difficult to distinguish the influences from different parameters, therefore simulation and experiment methods are used to investigate these parameters separately in order to understand which parameters play more important roles than the others.

First, LBM based code *DigiDiss* has been used to simulate single particle dissolves in diffusion dominated system with different particle parameters such as particle shape, surface area to volume ratio, pore structure.

Then, combining *DigiDiss* and COMSOL, single particle with digital structure scanned by X-ray microtomography has been used to simulate particle dissolving in convective condition. Meanwhile, experiment of single particle dissolving in a agitating system with identical geometry in the simulation model has been studied to understand agitation effect on convective dissolution.

And then, wetting process of water penetrating into open-ended straight pore has been statistically studied by both experimental and simulation methods.

Finally, combining simulation and experiment, a modelling framework for linking granule dissolution and system power has been developed (as shown in Figure 3.1), which consists derived equations based on Noyes-Whitney Equation and COMSOL simulation. Some parameters in this framework can be consulted from standard industrial handbook, while the rest of the parameters can be obtained by either numerical simulation or experiment.

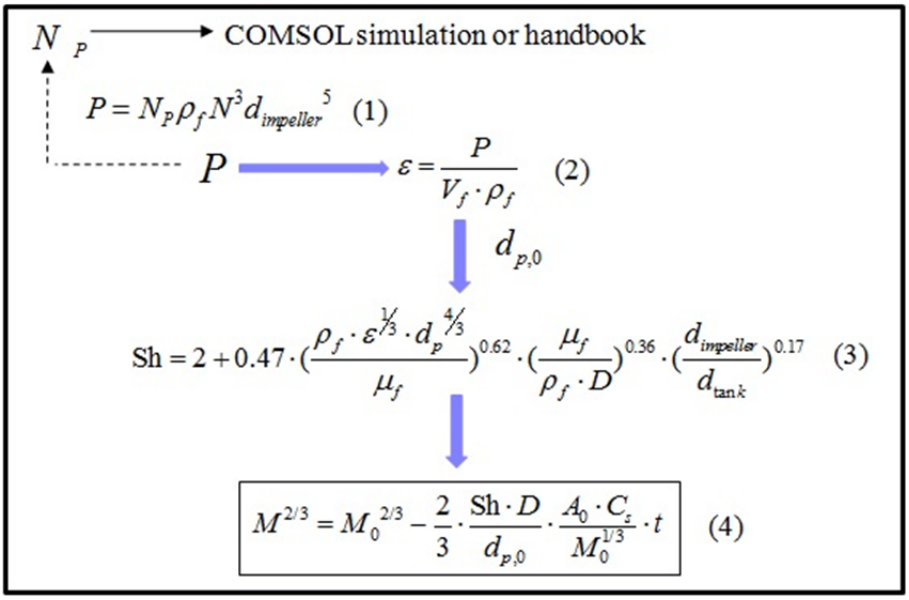

Figure 3. 1 A modelling framework for linking granule dissolution and system power.

Equation (1) is a standard equation from mixing industry which shows the relationship between system power and impeller dimension. The main factor for a mixing system is the power number N_P which can be either obtained from the handbook or calculated by COMSOL CFD module for some cases.

Once the system power is pre-known, the energy dissipation rate ε in the system can be calculated by Equation (2) and then this parameter can be implemented into Equation (3) to calculated the Sherwood number Sh of the system. The method to calculate Sherwood number is not restricted to Equation (3) as reviewed in Chapter 2. In this thesis the listed equation has been used.

Finally, the Sherwood number is implemented into Equation (4) to calculate the dissolution profile of particles which could be either porous or non porous structure. The derivation of Equation (4) will be explained in Chapter 5.

3.1 Modelling set up of *DigiDiss*

DigiDiss is used to simulate particle dissolution with different parameters such as particle shape, surface area to volume (S/V) ratio, pore structure and agitating, in order to understand the effect of these parameters on dissolution.

For the modelling of particle shape and S/V ratio effect, regular artificial particles with different shape and S/V ratio were generated by *DigiUtility*. For the modelling of particle pore structure and agitating, real particle scanned by X-ray Microtomography (XMT) were taken into use.

The structure, either generated using *DigiUtility* or acquired using XMT, is described in a lattice grid which is also used by the LBM simulation to calculate the flow field. With the finite difference method, the same grid can be used to solve the governing equations for dissolution:

$$\frac{\partial C}{\partial t} + (u_x \frac{\partial C}{\partial x} + u_y \frac{\partial C}{\partial y} + u_z \frac{\partial C}{\partial z}) = D(\frac{\partial^2 C}{\partial x^2} + \frac{\partial^2 C}{\partial y^2} + \frac{\partial^2 C}{\partial z^2}) \qquad 2\text{-}18$$

$$\frac{dW}{dt} = -KS(C_s - C) \qquad 2\text{-}19$$

The transient model with and without convection are used. At the solid/liquid interface, dissolution is described as Equation 2-19. Mass balance can be formulated at cell level as shown in Figure 3.2. For clarity the figure is shown as a 2D cell, but the formulation itself is in 3D.

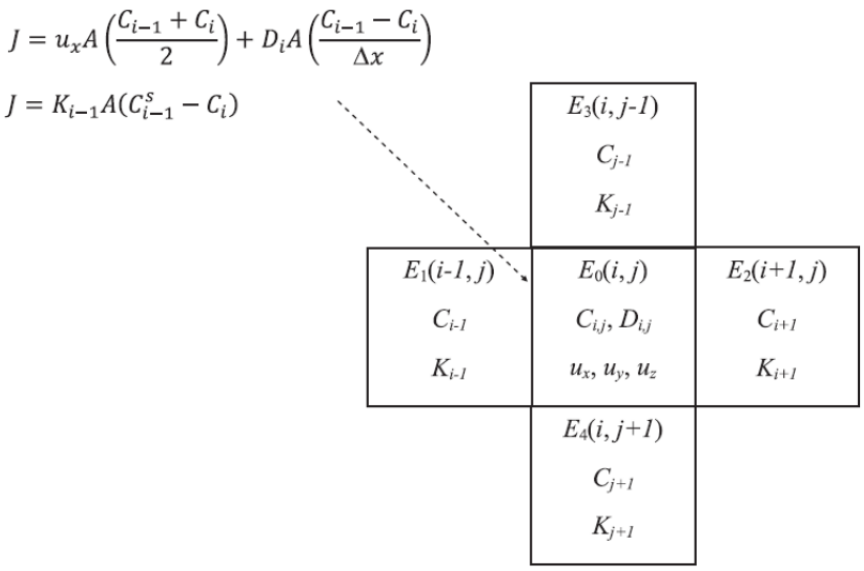

Figure 3. 2 Schematics of mathematical formulation for dissolution [119].

For a general transient mode, the following equations can be written explicitly, which state that the rate of change in mass for a particular component in the fluid cell is the sum of gains and losses of mass due to convection, diffusion and dissolution, on each of the six sides of the cell.

$$
\begin{aligned}
&V\frac{C^{t+\Delta t}-C}{\Delta t} = && \text{mass increase rate}\\
&+uc_x A + uc_y A + uc_z A && \text{convection in } X, Y, Z\\
&+k_{i-1}A(C^s_{i-1}-C) + k_{i+1}A(C^s_{i+1}-C) && \text{dissolution in } X\\
&+k_{j-1}A(C^s_{j-1}-C) + k_{j+1}A(C^s_{j+1}-C) && \text{dissolution in } Y\\
&+k_{k-1}A(C^s_{k-1}-C) + k_{k+1}A(C^s_{k+1}-C) && \text{dissolution in } Z\\
&+DA\left(\frac{C_{i-1}-C}{\Delta x}+\frac{C_{i+1}-C}{\Delta x}\right) && \text{diffusion in } X\\
&+DA\left(\frac{C_{j-1}-C}{\Delta x}+\frac{C_{j+1}-C}{\Delta x}\right) && \text{diffusion in } Y\\
&+DA\left(\frac{C_{k-1}-C}{\Delta x}+\frac{C_{k+1}-C}{\Delta x}\right) && \text{diffusion in } Z
\end{aligned}
\qquad \text{3-1}
$$

in which $V = (\Delta x)^3$, $A = (\Delta x)^2$, $\Delta x = \Delta y = \Delta z$,

$$uc_x = \begin{cases} |u_x|(C_{i-1} - C) & \text{if } u_x > 0 \\ |u_x|(C_{i+1} - C) & \text{if } u_x < 0 \end{cases}$$

$$uc_y = \begin{cases} |u_y|(C_{j-1} - C) & \text{if } u_y > 0 \\ |u_y|(C_{j+1} - C) & \text{if } u_y < 0 \end{cases}$$

$$uc_z = \begin{cases} |u_z|(C_{k-1} - C) & \text{if } u_z > 0 \\ |u_z|(C_{k+1} - C) & \text{if } u_z < 0 \end{cases}$$

and

$$\begin{aligned} C^{t+1} = C + \frac{\Delta t}{\Delta x}[uc_x + uc_y + uc_z] + \frac{\Delta t}{\Delta x}[k_{i-1}(C^s_{i-1} - C) + k_{i+1}(C^s_{i+1} - C) + k_{j-1}(C^s_{j-1} - C) \\ + k_{j+1}(C^s_{j+1} - C) + k_{k-1}(C^s_{k-1} - C) + k_{k+1}(C^s_{k+1} - C)] + \frac{D\Delta t}{\Delta x^2}[(C_{i-1} - C) + (C_{i+1} - C) \\ + (C_{j-1} - C) + (C_{j+1} - C) + (C_{k-1} - C) + (C_{k+1} - C)] \end{aligned} .$$

Equation 3-1 update the concentration explicitly at each time step. The formulations is first-order accurate in space and time. A small time step that meets the Courant-Friedrichs-Lewy rule is required for numerical stability [121]. In practice, the following check is built into the computer code to warn against numerical instability and oscillation (when flow is involved) for each component, and a fraction of the critical value (maximum liquid velocity $u_{\max}$) is actually used:

$$\begin{aligned} \Delta t &\le \min\left(\frac{\Delta x^2}{6D}, \frac{\Delta x}{6K}\right) \\ \Delta x &\le \frac{2D}{|u_{\max}|} \end{aligned} \qquad 3\text{-}2$$

Solid wall is used as domain boundary condition throughout the simulation. The Noyes-Whitney equation is used explicitly to specify boundary condition at solid-liquid interfaces, which implies that dissolution and diffusion are considered as two separate processes. The computing precision and the balance between time scale, model pixel numbers and steady state are explained in [119]. Figure 3.3 shows three typical geometric models of *DigiDiss*. In the pictures, the red objects represent regular shaped solid particles which are generated by *DigiUtility*. The black box around the particle represents water domain.

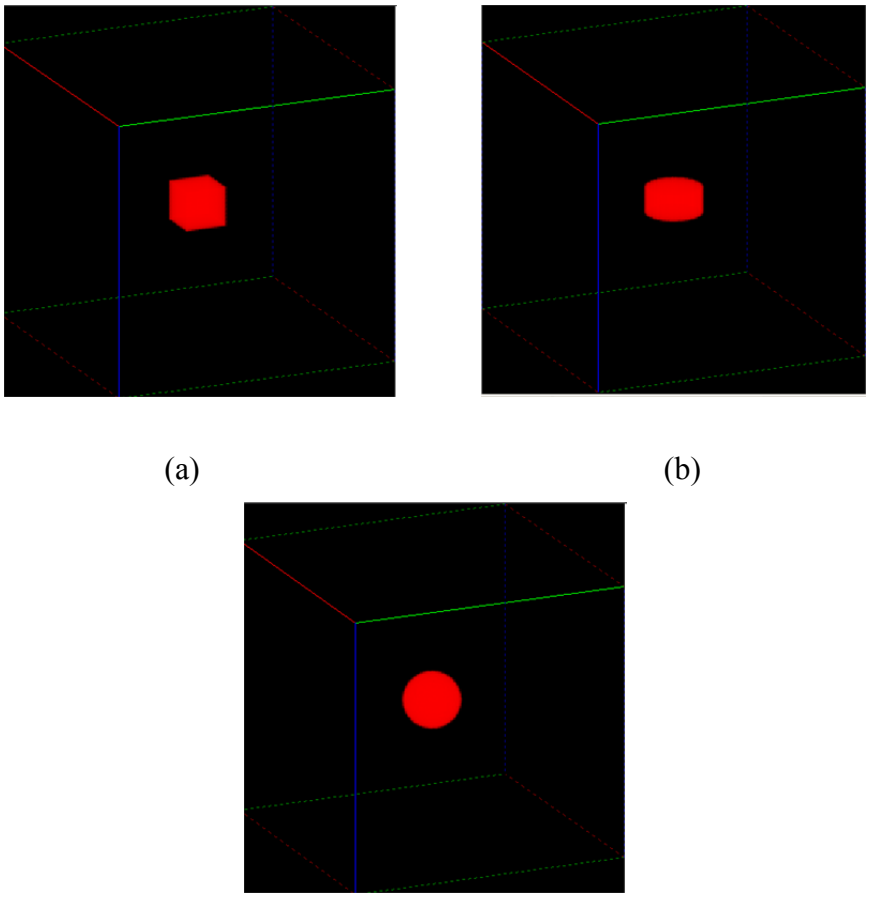

(a) (b)

(c)

Figure 3. 3 Geometric models of DigiDiss: (a) cubic particle (edge 1.447 mm), (b) cylindrical particle (radius 1 mm, height 1 mm) and (c) spherical particle (radius 1mm).

The unique advantage of *DigiDiss* is the capability of importing real particle structure scanned by X-ray Microtomography (XMT) (Phoenix Nanotom) into the model. Figure 3.4 is the geometry of a real particle scanned by XMT. As a result, different pore structures are created in the cross-section (Figure 3.5) to simulate the effect of pores on solid release during the dissolution.

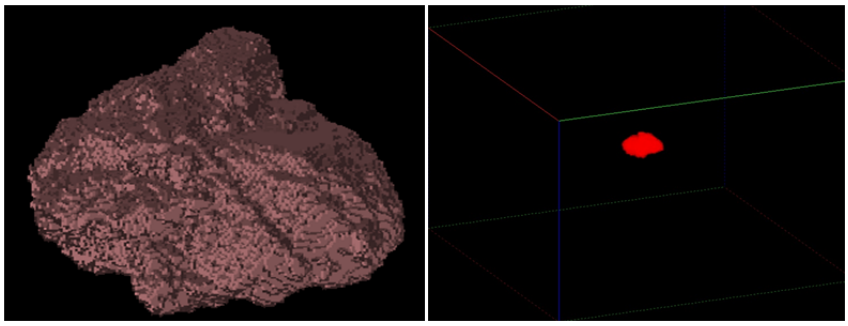

(a) (b)

Figure 3. 4 (a) 3D digital geometry of a real particle scanned by XMT. (b) Digital particle in water domain.

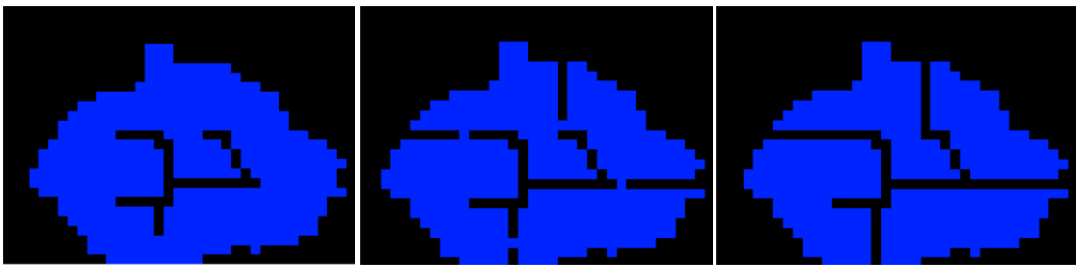

(a) (b) (c)

Figure 3. 5 Cross-section of different pore structures (a) inner pores (b) inner pores with surface pores and (c) throughout pores.

3.2 Modelling and experiment set up of wetting process

Surface tension and wall adhesive forces play a very important role in wetting process. It's always difficult to track two-phase interface in a porous media. As reviewed in Chapter 2, researchers have developed different simulation methods to model this phenomenon. In this research, as the particle dissolves in water immediately when wetting process happens, it's very challenge to couple these two processes in one model, so a simple model is used to simulate how surface tension and wall adhesive forces affect the wetting process regardless the effect of wetting process.

First, a macro sized straight channel is generated by COMSOL Multiphysics. The Two-Phase Flow, Laminar, Level Set module is used to simulate the movement of

air/liquid interface as a function of time by capillary force. According to Lucas-Washburn equation (Equation 2-22), four main parameters, liquid surface tension γ, channel width r, liquid viscosity μ and contact angle of liquid on channel wall θ are used in the model as either material property or boundary conditions to investigate how these parameters affect the wetting process.

Then, experiments of the wetting process of respectively capillary tubes are carried out with a high speed camera to capture the movement of the air/liquid interface as a function of time. Experiment results are compared to the simulation result to validate the model.

At last, models with micro sized channels are simulated to observe the wetting process in particle related channel width.

3.2.1 Modelling set up in COMSOL Multiphysics

The Two-Phase Flow, Laminar, Level Set module is used for the wetting process. The model consists of a capillary channel of radius 0.34 mm, 0.45 mm and 0.56 mm attached to a reservoir. Because both the channel and the reservoir are cylindrical, a axisymmetric geometry can be used illustrated in Figure 3.6. Initially, the thin cylinder is filled with air. Wall adhesion causes water to creep up along the cylinder boundaries. The deformation of the water surface induces surface tension at the air/water interface, which in turn creates a pressure jump across the interface. The pressure variations cause water and air to move upward. The fluids continue to rises in the channel until the equilibrium between capillary force, adhesion force and gravity force is achieved.

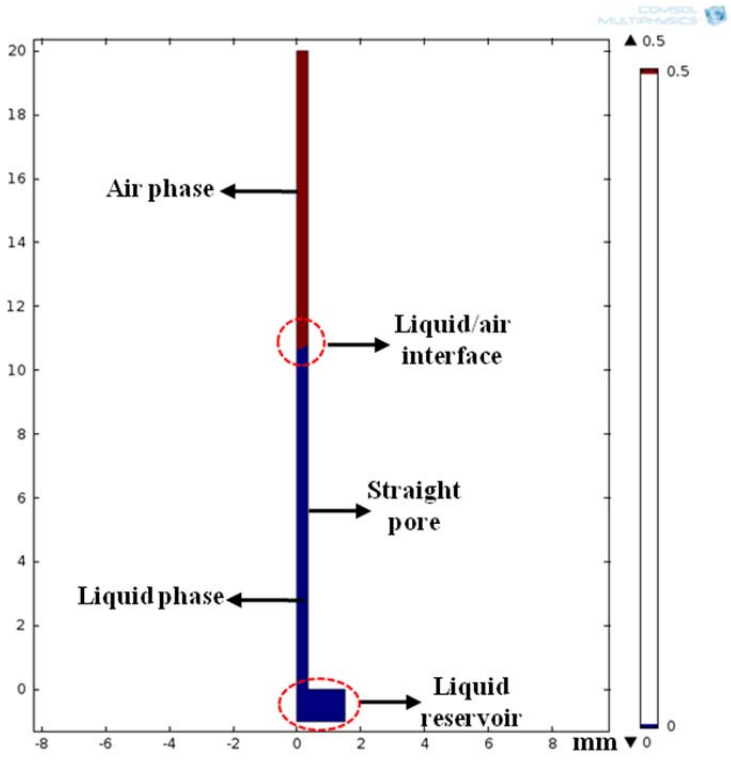

(a)

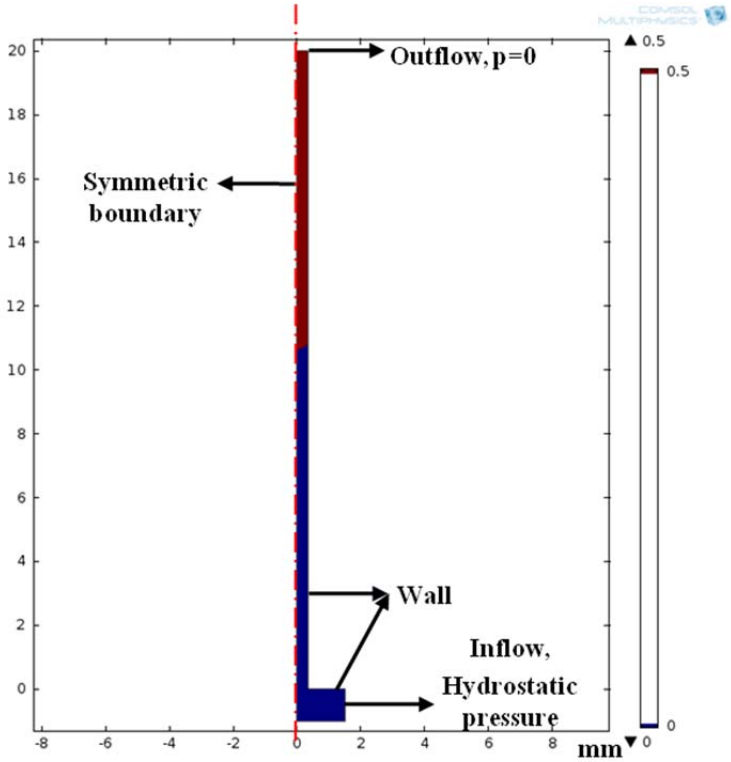

(b)

Figure 3. 6 (a) Axisymmetric geometry description and (b) boundary conditions.

Mass and Momentum Transport The Navier-Stokes equation describes the transport of mass and momentum for fluids of constant density. In order to account for capillary effects, it is crucial to include surface tension in the model. The Navier-Stokes equations are then

$$\rho\frac{\partial u}{\partial t}+\rho(u\cdot\nabla)u=\nabla\cdot[-p\mathrm{I}+\mu(\nabla u+(\nabla u)^{T})]+F_{st}+\rho g \qquad 3\text{-}3$$
$$\nabla\cdot u=0$$

where ρ is fluid density, μ is fluid dynamic viscosity, u is velocity, p is pressure, I is the identity matrix, and g is gravity vector. F_{st} is the surface tension force acting at the air/water interface. Finite element method is used to solve the Navier-Stokes equations.

Surface Tension The surface tension force is computed as

$$F_{st}=\nabla\cdot(\sigma(\mathrm{I}-(\mathrm{nn}^{T}))\delta') \qquad 3\text{-}4$$

where n is the interface normal, σ is the surface tension coefficient, and δ' is a Dirac delta function that is nonzero only at the fluid interface. An integral of F_{st} over the computational domain plus a boundary integral of the form

$\int_{\partial\Omega}\mathrm{test}(u)\cdot[\sigma(\mathrm{n}_{wall}-(\mathrm{ncos}\theta))\delta']dS$ with a test function is used to multiply Equation 3-4. θ is the contact angle (see Figure 3.7). The wetted wall boundary condition makes the specify of the contact angle possible and allows a small amount of slip.

Level Set Method The Two-Phase Flow, Laminar, Level Set application mode automatically sets up the equations for the convection of the interface. The application mode represents the interface as the 0.5 contour of the level set function ϕ . In air $\phi=0$ and in water $\phi=1$. The level set function can thus be thought of as

the volume fraction of water. The transport of the fluid interface separating the two phases is given by

$$\frac{\partial \phi}{\partial t} + u \cdot \nabla \phi = \dot{\gamma} \nabla \cdot (\xi \nabla \phi - \phi(1-\phi)\frac{\nabla \phi}{|\nabla \phi|}) \qquad 3\text{-}5$$

The ξ parameter determines the thickness of the interface. When stabilization is used for the level set equation, a typically thickness of $\xi = h_c / 2$ can be used, where h_c is the characteristic mesh size in the region passed by the interface. The $\dot{\gamma}$ parameter determines the amount of reinitialization.

The application mode uses the level set function ϕ to smooth the density and viscosity jump across the interface by letting

$$\begin{aligned} \rho &= \rho_{air} + (\rho_{water} - \rho_{air})\phi \\ \mu &= \mu_{air} + (\mu_{water} - \mu_{air})\phi \end{aligned} \qquad 3\text{-}6$$

The delta function in Equation 3-4 is approximated by $\delta' = 6|\phi(1-\phi)||\nabla \phi|$ and the interface normal is calculated from $\mathrm{n} = \frac{\nabla \phi}{|\nabla \phi|}$.

Initial Conditions Initially, the reservoir is filled with water and the capillary channel is filled with air. The initial velocity is zero.

Boundary Conditions At the inlet, the hydrostatic pressure $p = \rho g z$ gives the pressure at the inflow boundary. Only water enters through the inlet, so the level set function (which is the volume fraction of water) here is 1.

At the outlet, the pressure is equal to zero, which is equal to the pressure at the top of the inflow boundary and there's no need to set the level set function.

The Wetted wall boundary condition is suitable for solid walls in contact with a fluid interface. It sets the velocity component normal to the wall to zero, and adds a frictional boundary force $F_{fr} = -\frac{\mu}{\beta}$ where β is the slip length.

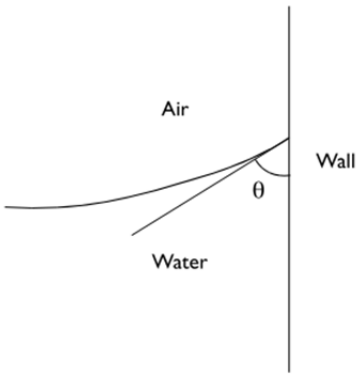

Figure 3. 7 Definition of the contact angle θ .

3.2.2 Experiment set up

The wetting rates of water/ethanol mixtures into capillary glass tubes are observed by recording the wetting process using high speed camera to capture the movement of air/liquid interface as a function of time.

Materials

Capillaries The capillaries used in the experiments were glass capillaries purchased from World Precision Instruments Ltd (radii: 0.34mm, 0.45mm and 0.56mm). Before measurements, the capillaries were cleaned with pure ethanol, rinsed in deionised water, and dried in clean air atmosphere at 60°C. Hydrophobic capillaries were obtained by exposing (for several hours) the clean glass capillaries to Trimethylchlorosilane (Sigma-Aldrich, purity > 99%) reacting with the silanol groups present at the surface of glass at room temperature. The hydrophobized

capillaries were thoroughly rinsed with ethanol and deionised water and dried at 60°C.

Chemicals Deionised water and pure ethanol were mixed with different ratio as in Table 1. Physical properties of these mixtures are measure with relevant equipments for example Density meter (DMA Generation M, Anton Paar), Rheometer (MCR Series, Anton Paar) and Contact Angle Measuring System (EasyDrop, KRUSS).

Table 3. 1 Physical properties measuring results of water/ethanol mixtures by volume fraction at 20°C in atmosphere.

Liquid	**Water**	**80% Water & 20% Ethanol**	**60% Water & 40% Ethanol**	**40% Water & 60% Ethanol**	**20% Water & 80% Ethanol**	**Ethanol**
Density ρ (10^3 kg/m3)	0.9982	0.9733	0.9460	0.9043	0.8551	0.7884
Viscosity μ (10^{-3} Pa·s)	1.002	1.9316	2.7917	2.7855	2.1807	1.144
Surface tension γ (10^{-3} N/m)	72.75	41.48	32.47	27.76	24.87	22.27

Methods

Capillary dynamics The capillary rise dynamics was followed from the moment the capillary was put in contact with the liquid. The liquid was placed in a cylindrical glass dish filled slightly over the rim to allow imaging immediately from the moment the capillary touches the liquid. Fast rise processes were monitored with a high speed camera (FASTCAM SA 5, Photron Ltd) connected to a computer. The camera can capture up to 2000 frames per second with full resolution. Slower

processes were followed with a standard CCD video camera. The images were analyzed by an image software combined with the high speed camera.

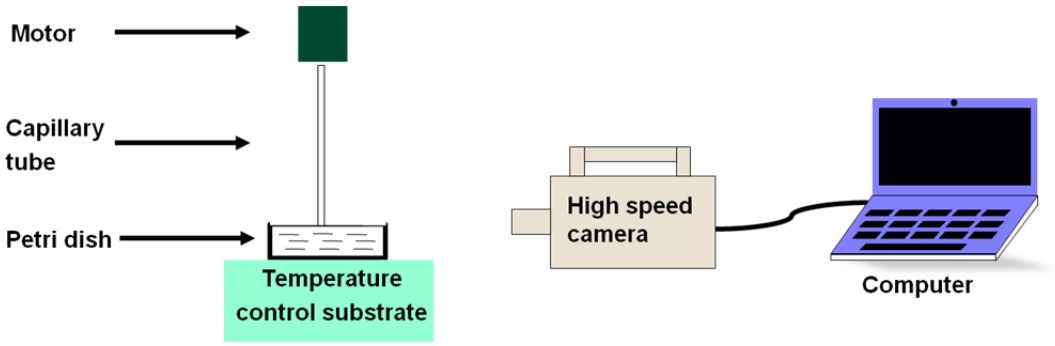

Figure 3. 8 Schematic of capillary dynamics experiment.

Surface morphology The surface morphology of capillaries before and after coating process was scanned by AFM in order to investigate whether this coating process will change the surface tomography. The images were recorded at 2 μm planar in contact mode.

3.3 Modelling and experiment set up of convective dissolution

The research strategy for convective dissolution is divided into two methods according to the particle quantity.

For single particle, optical image analyse of particle dissolving in a cubic cuvette with magnetic stir is used to investigate how shear rate around particle affect the mass transfer rate. The respective simulation combining COMSOL CFD module and *DigiDiss* code is modelled to analyse the relationship between shear rate and mass transfer rate.

For a population of particles, mass transfer equation including particle size distribution is derived from Noyes-Whitney equation. Energy dissipation rate in the stirring tank simulated by COMSOL CFD module is employed into the equation as Sherwood number to link power consuming and convective dissolution of particles.

Experiments of a population of particles dissolve in water at different rpm and temperature are carried out to validate the relationship.

3.2.1 Single particle

Experiment

A high speed camera (FASTCAM SA 5, Photron Ltd) with macro lens is used to focus on the single particle inside a transparent cubic cuvette. The size of the cuvette is 15 mm x 15 mm x 15 mm. First, 1.8 mL DI water is added into the cuvette and the magnetic stir is switched on. Then particle is loaded into a holder made by copper wire simply to for the particle to sit on. The wire is attached to a motor to drive the particle into water steadily. Once particle touches water, it starts dissolving and before it totally dissolves, particle falls off the wire due to the drag force from water. High speed camera records the whole process by 500 frame per second and then the video is analyzed by free software ImageJ. The information of particle shape change as a function of time is extracted by the software. Figure 3.9 shows the dissolution experiment of a single particle sitting on the wire and positioned at different places around the magnetic stir.

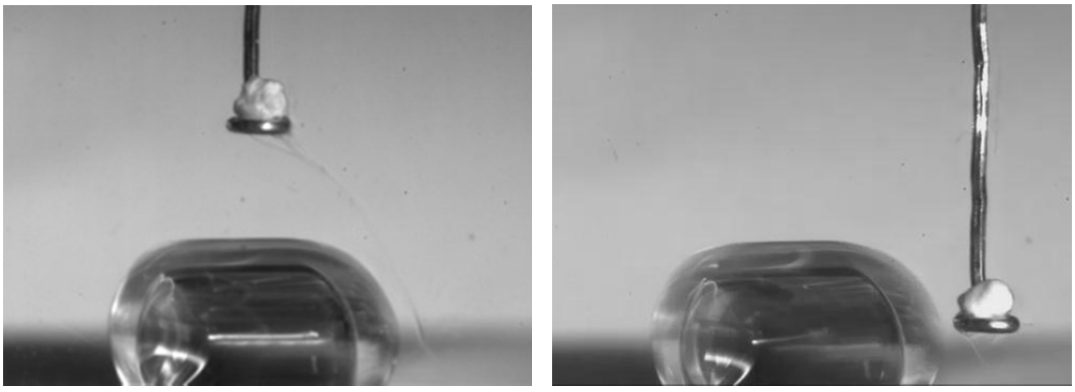

(a) (b)

Figure 3. 9 Dissolution experiment of a single particle at different position (a) on top of the stir and (b) beside the stir.

Simulation in COMSOL

In order to simulate single particle dissolving under convective condition, COMSOL Multiphysics Rotating Machinery, Laminar Flow module is used to first calculate the velocity distribution of stirring tank. Then the velocity is imported into *DigiDiss*.

The Rotating Machinery in COMSOL CFD module allows moving rotating parts in stirred tanks, mixers and pumps etc. It formulates the Navier-Stockes equations in a rotating coordinate system. Parts that are not rotated are expressed in the fixed material coordinate system. The rotating and fixed parts are coupled together by an identity pair, where a flux continuity boundary conditions is applied.

Figure 3.10 shows the geometry of the model. The geometry is divided into two parts. The outer cylinder is a fixed part, and the inner cylinder with a magnetic stir is defined as rotating part. The magnetic stir rotates counter clockwise at a speed of 100 rpm and 200 rpm. Navier-Stokes equations formulates both in the rotating frame in the inner domain and the fixed coordinated in the outer one. Between outer domain and inner domain, walls are assembled as identity pair. All the other walls are set as non slip boundary conditions. Water property is applied through the whole domain. Mesh size between 0.02 mm and 0.05 mm is applied.

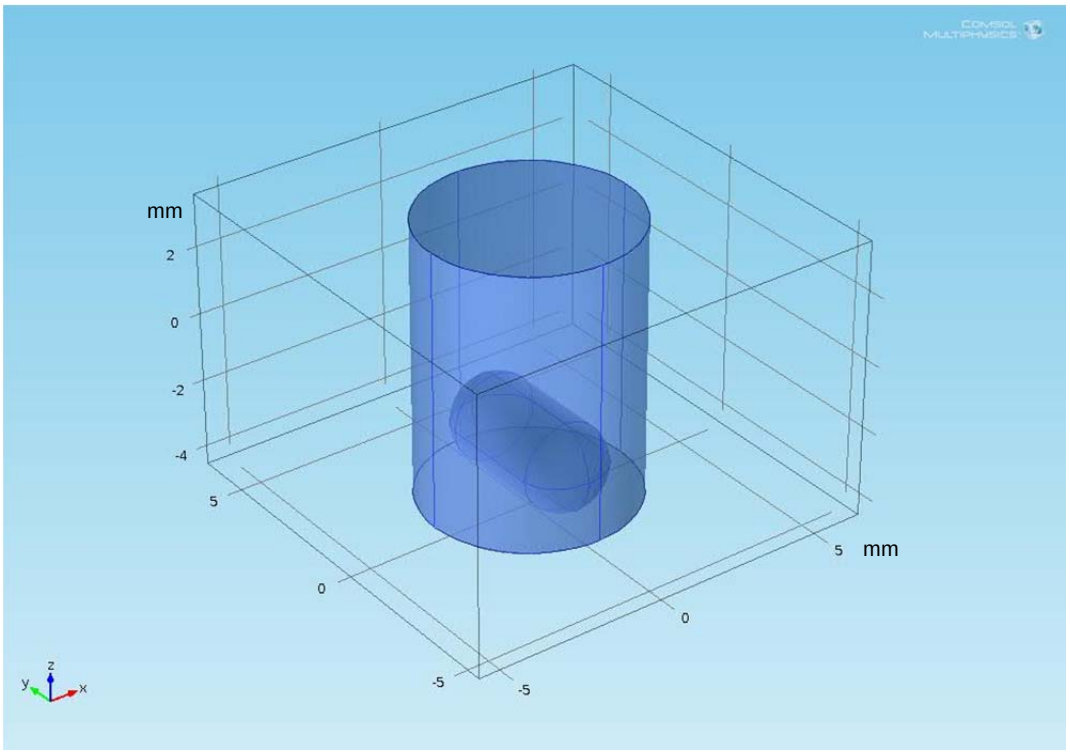

Figure 3. 10 Geometry of the magnetic stirred cuvette.

After the stir runs with full speed for a certain time (which will be explained later in the result and discussion chapter), the velocity distribution inside the whole domain is exported as text file and then imported into *DigiDiss* as initial condition.

Simulation in DigiDiss

The digital structure of a single particle is scanned by X-ray microtomography and imported into *DigiDiss*. After velocity distribution calculated by COMSOL is imported into the model as initial condition, simulation is set to run with particles at different positions according to the experiment. The dissolution profile and concentration distribution inside water domain is plotted by *DigiDiss* in order to understand how the share rate affects particle dissolution.

3.2.2 A population of particles

The relationship between system power and dissolution rate of a population of particles is linked by introducing Sherwood number and PSD into Noyes-Whitney equation as showing in Figure 3.1. Some parameters in Equation (4) are measured by experiment, some are calculated by COMSOL Multiphysics. And the dissolution test of a population of particles dissolving in a stirring tank at different temperature and rpm is carried out to validate the developed framework. Non porous single ingredients particle sodium carbonate granule (batch number 1009260NM-019) and porous multi ingredients particle PANDORA (including sodium carbonate, sodium sulphate, sodium silicate and linear alkylbenzene sulfonates) are used in this thesis, and all the samples are provided by Procter & Gamble Newcastle Innovation Center.

Experiment

Liquid density Water density at different temperature is measured by Density meter (DMA Generation M, Anton Paar).

Liquid viscosity Water viscosity at different temperature is measured by Rheometer (MCR Series, Anton Paar).

Particle size distribution Particle size distribution is measured by gravity dispersion for image analysis (GRADIS/L, Sympatec GmbH).

Solubility The solubility PANDOR agglomerate are measured by adding certain amount of samples into water each time and measuring solution conductivity (Conductivity meter, JENWAY 470) as a function of sample mass until the conductivity stops changing with mass. The solubility of sample particles is measured at 20 dC, 40dC and 60 dC.

Specific surface area The specific surface area of sample particles are measured by BET method (TriStar 3000, Micromeritics).

Dissolution test A population of particles are added into dissolution apparatus shown as in Figure 2.8. The experiment is carried out in Proctor & Gamble Newcastle Innovation Center. 0.15g particles are used in the test. Solution conductivity is measured as a function of time. Each sample is tested at three different temperatures 20 dC, 40 dC and 60 dC with 100 rpm, 200 rpm and 300 rpm respectively. Experiment data is then used to validate the framework in Figure 3.1

Simulation in COMSOL

Same module as single granule simulation in COMSOL is used in order to calculate the energy dissipation in the stirring tank, but for turbulent flow. This is because in the dissolution apparatus, for all the rotating speed used in this thesis, the flow is turbulent flow. The calculation of Reynolds number in the stirring tank will be explained later in the results and discussion chapters.

Figure 3.11 shows the geometry of the model. Similar setting up is applied to this model. Rotating speed of 100 rpm, 200 rpm and 300 rpm are calculated at 20 dC, 40 dC and 60 dC respectively.

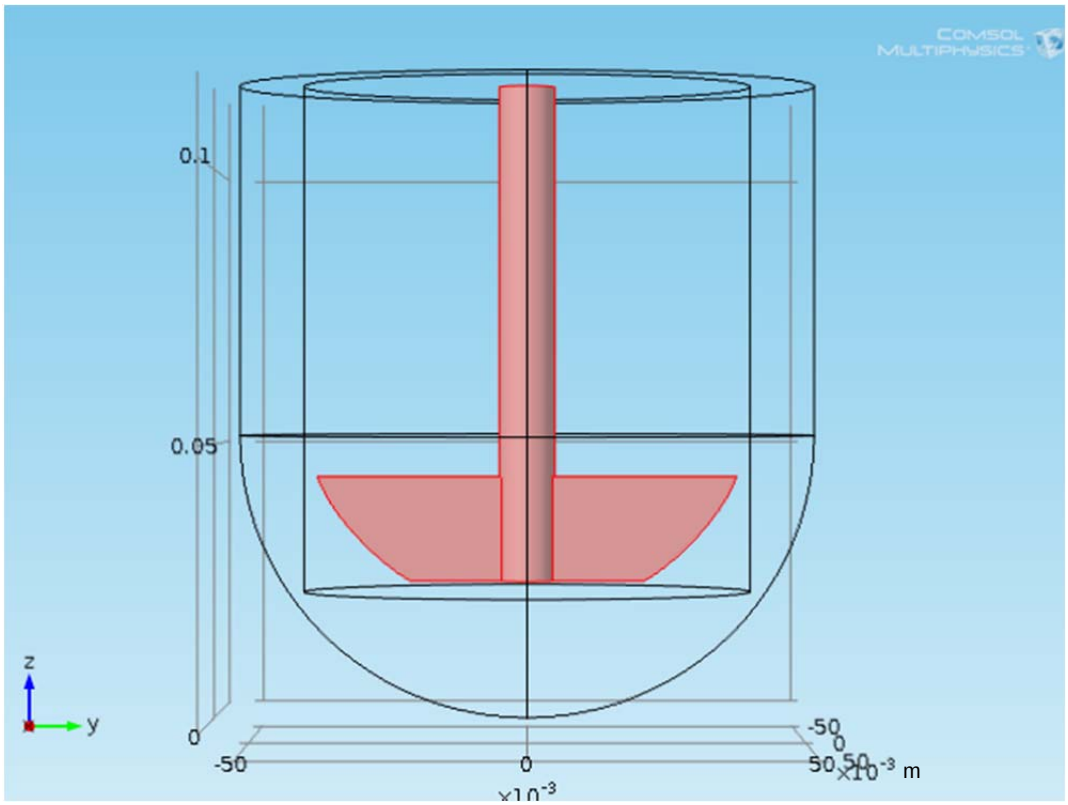

Figure 3. 11 Geometry of the dissolution tank.

For general case, if the impeller power number can be found from the industrial mixing handbook, the power on the impeller in a stirring tank can be calculated by

$$P = N_P \rho_f N^3 d_{impeller}{}^5 \qquad 3\text{-}7$$

where N_P is the impeller power number, N is the rotating speed in rpm. While the flow is turbulent, Equation 3-7 shows that power number N_p is independent of Reynolds number.

The energy dissipation inside the tank can be calculated by

$$\varepsilon = \frac{P}{V_f \cdot \rho_f} \qquad 3\text{-}8$$

then Sherwood number can be calculated by Equation 2-12.

However, for some cases while the power number information of the impeller cannot be found in the handbook, for example in this thesis, the power on the impeller can be calculated by adding the Equation 3-9 to COMSOL post-process.

$$P = \int_A \Omega \cdot \Gamma dA = \int_A \Omega \cdot (\mathrm{r} \times \mathrm{F}_{impeller}) dA_{impeller}$$
$$r = \{x, y, z\} \qquad 3\text{-}9$$
$$\Omega = 2\pi N$$

in which $F_{impeller}$ is the force acting on each point of impeller surface, Ω is rotating speed in 1/s, $A_{impeller}$ is impeller surface area, Γ is torque on impeller and $\{x, y, z\}$ is coordinate. Since the impeller shaft is parallel to the z-axis in the model, Equation 3-9 can be reduced to

$$P = \int_A 2\pi N (xF_y - yF_x) dA_{impeller} \qquad 3\text{-}10$$

As a result, the impeller power can be calculated by integrating the force on the whole impeller surface. Once the impeller power is integrated, the Sherwood number can be calculated as the general case.

CHAPTER 4
SIMULATION OF PARAMETERS AFFECT DISSOLUTION

Particle dissolution rate can be affected by a variety of parameters, for example physiochemcial related properties solubility, diffusivity, particle shape, size, surface area, internal structure (pores), and fluid related properties liquid temperature, pH value, agitation etc.

In this chapter, *DigiDiss* is used to investigate the effect of particle shape, surface area to volume ratio and pore structure under diffusion dominated dissolution. Then the coupling of *DigiDiss* and COMSOL is used to investigate agitation effect on convective dissolution. COMSOL is also used to simulate the wetting process and model is validated by experiment.

4.1 Simulation of particle shape effect on diffusion dominated dissolution

Three regular shaped particles, cubic, cylindrical and spherical were generated by *DigiUtility* and imported into *DigiDiss* to simulate the particle shape effect on dissolution with diffusion module. Particle properties were set as sodium carbonate (shown in Table 4.1). After particle releases 25 %, 50 % and 75 % of the total mass, concentration distribution in solution was plotted to illustrate the morphology change of particle shape respectively.

Figure 4.1 shows the simulated release profile. The complete dissolution time for different particles are different according to the total mass of particles. The implemented images show the concentration distribution of Na_2CO_3 in the water. Within the images, four colour zones can be seen. The white in the middle is the solid Na_2CO_3. The red region next to the solid Na_2CO_3 is the high concentration zone of dissolved Na_2CO_3. Further out as the Na_2CO_3 concentration decreases, there

are yellowish, greenish and blue zone. The images suggest that Na_2CO_3 dissolves faster than it diffuses away so that a significant high concentration zone is formed.

By comparing concentration distribution figures implemented in Figure 4.1, one can find out that both (a) cube and (b) cylinder have very clear shape changes at 25 % and 50 %. At 25 %, particles remain more or less the same shape as original. When 50 % of the mass dissolving into water, the corners of cubic particle disappear. At 75 %, the edges of cubic particle disappear as well, and particle becomes more like a sphere. Similar phenomena happens on cylinder particle. These results indicate that mass transfer rate on the corners and edges are faster than on the face. A simple conclusion can be made from these results, that particles with different shapes shrink from the outside into the center of the particle. After a certain time, particle become smoother and smoother, corner and edge structure disappears. Similar phenomena was also observed by Dr Yuan [28].

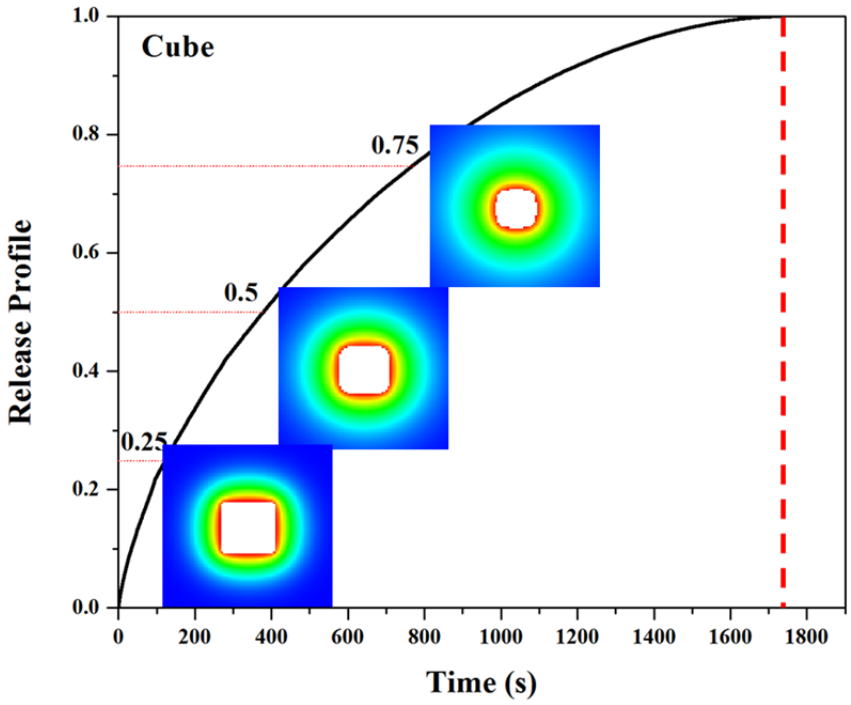

(a)

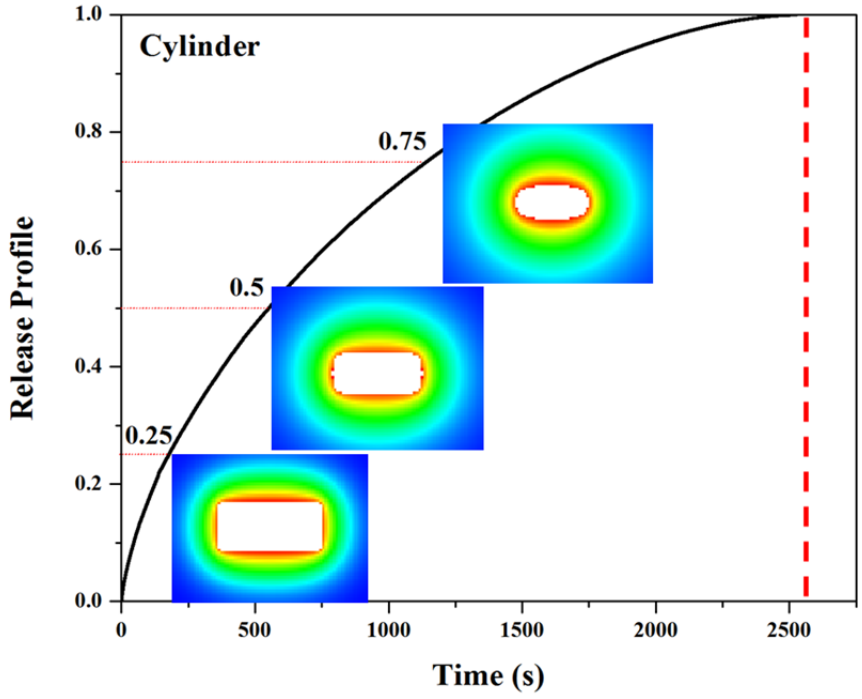

(b)

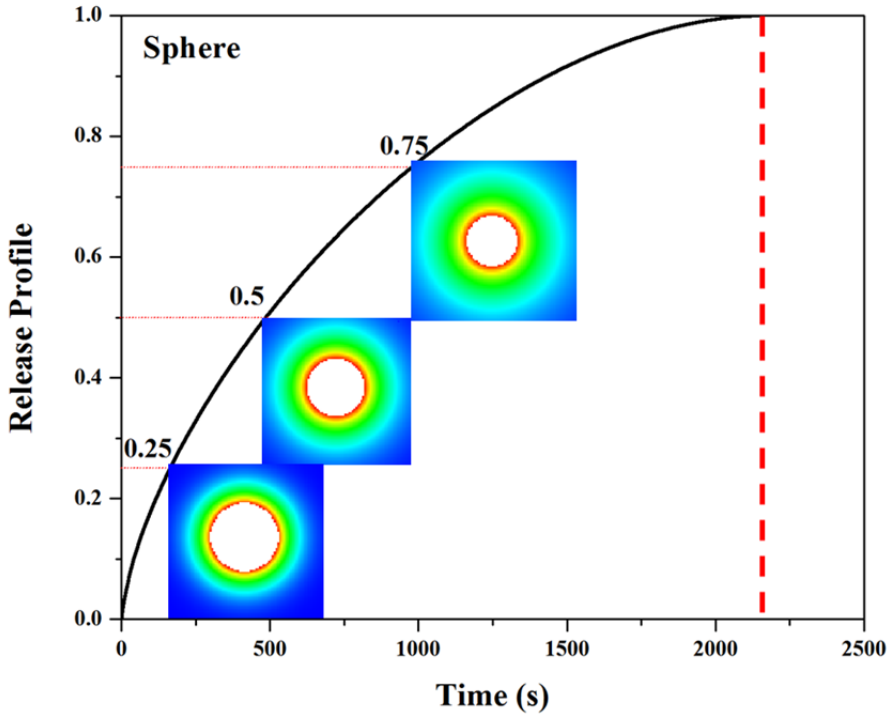

(c)

Figure 4. 1 Dissolution profile of different regular shaped particles under diffusion condition: (a) cube, (b) cylinder, and (c) sphere. Inserted pictures are concentration distribution of particles in water at different release percentage, 0.25, 0.5 and 0.75 respectively.

4.2 Simulation of surface area to volume ratio effect on diffusion dominated dissolution

Particles with the same volume but different surface area dissolve in different rate. It is difficult to quantify particle S/V ratio while keeping other parameters unique such as particle shape, weight. In this section, three Na_2CO_3 particles with identical volume were generated by *DigiUtility* and imported into *DigiDiss* to simulate the particle S/V ratio effect on dissolution with diffusion module.

Particle geometry information was listed in Table 4.1. From Rod to Disc, particles radius and height changes, but the volume are more or less the same, which indicates the weight of three particles are more or less the same. The S/V ratio from Rod to Tablet slightly increases, but from Rod to Disc increases nearly three times. Particle properties and parameters were set to the same as in previous section.

Table 4. 1 Different surface area to volume ratio (S/V ratio).

	Radius (mm)	**Height (mm)**	**S/V ratio**
Rod	0.3	1.6	7.92
Tablet	0.6	0.4	8.33
Disc	1.2	0.1	21.67

Figure 4.2 shows the simulation results of particles release profile. Three lines represent three particles. Implemented pictures are the image captures of particles generated by *DigiUtility*. The total release time for Disc shaped particle is 143 s. Tablet shaped particle is 619s and Rod shapes particle is 642 s. It is very clear in the figure that Disc shaped particle dissolves much faster than the other two. As the S/V ratio increases nearly three times from Rod shape to Disc shape, the total dissolution

time decreases almost 4.5 times. These results indicate that S/V ratio can affect dissolution significantly.

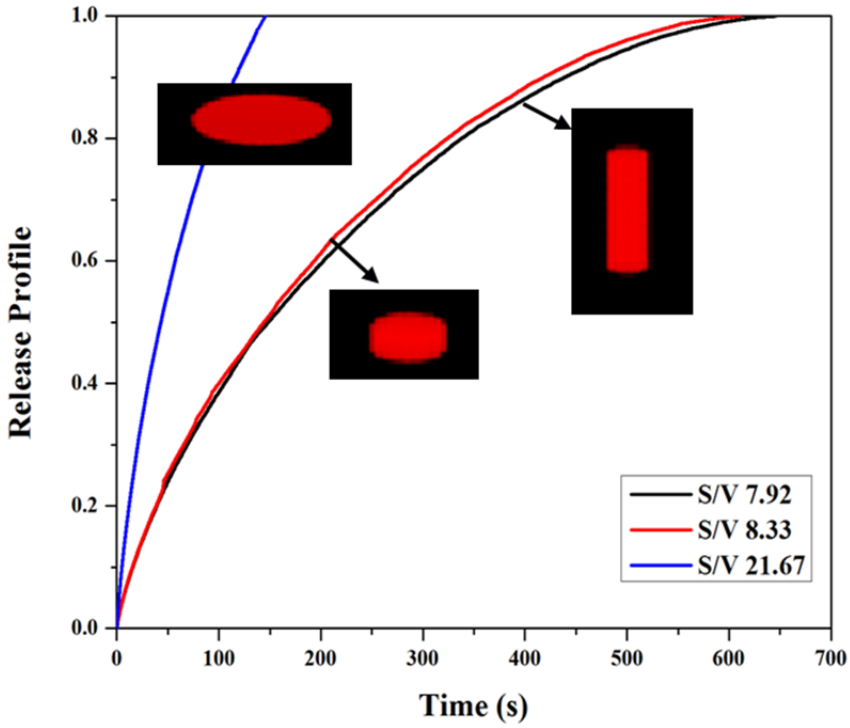

Figure 4. 2 Dissolution profile of different surface area to volume ratio particles under diffusion condition.

4.3 Simulation of pore structure effect on diffusion dominated dissolution

Pore structure is another important effect in particle dissolution. Depends on the location of pores on the particles, they can be classified into two different types. One is close-ended pore, they normally distribute on the surface of particles or inside particles without connection to the outer medium. The other one is open-ended pore, they normally through one side of particle to another, and water can penetrate into this type pores by capillary force.

The dissolution behaviour of porous particle is a complex process depending on the pore structure of the particle. For the close-ended pores, as water cannot penetrate into these type pores, whether solid on the wall of the pore dissolves or not is difficult to conclude. On the other hand, for the open-ended pores, water can easily penetrate inside by capillary force. Once water goes inside the pores, solid on the wall start dissolving. However, weather this part dissolution significantly affect the whole dissolution, or solution inside pores become saturated immediately and stop solid dissolving into water hence not contribute to the whole dissolution, remains difficult to conclude.

In this chapter, three models have been built and simulated in *DigiDiss* in order to understand how pore structure affect dissolution.

A non-porous single Na_2CO_3 granule (provided by Procter and Gamble Newcastle Innovation Center) was scanned by X-ray microtomography (XRT) and reconstructered into a digital 3D model as shown in Figure 4.3. Then, a cross-section was chosen to artificially create different type pores inside this granule by *DigiUtility*. In Figure 4.4, from top to bottom, the first column shows close-ended pore inside particle, close-ended pore inside and on surface of particle, open-ended pore respectively. Models with different type pore structure were then imported into *DigiDiss* to simulate dissolution process. Same particle properties and diffusion model were set up as previous chapters.

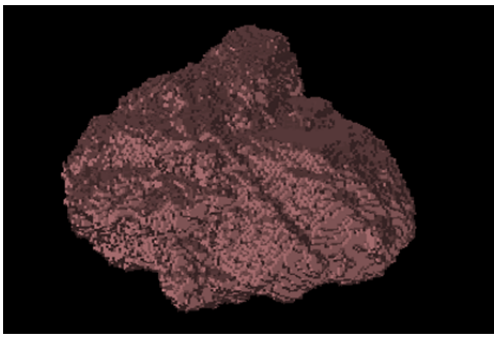

Figure 4. 3 3D structure of Na2CO3 granule scanned by XRT.

The concentration distribution on cross-section where the pores were created were plotted at dissolution time of 0.3 s, 1 s and 800 s for each model. In Figure 4.4, the three rows pictures show from the beginning to nearly the end of dissolution, concentration distribution of solid in water changes as a function of time. The top row is close-ended pore inside particle, second row is close-ended pore inside and on the surface of particle, and the bottom row is open-ended pore.

Once the model was imported into *DigiDiss*, the pores were automatically filled by water, showing in the first column in Figure 4.4 as black part, same as the outer part of particle. Once particle start dissolving, solid goes into water from everywhere exposed to water, including outer surface of particle and pore surface inside particle (specially in Figure 4.4 (a) where pores are not exposed to outer water), as showing at time 0.3 s. Then the concentration inside pores become saturated at time 1 s (red zones). As dissolution continues, the particle shrinks from outside, those inner pores in Figure 4.4 (a) start contact with water outside which might slightly accelerate the dissolution. However, concentration distribution results at time 800 s, while particle dissolution nearly finishes, pore structure still exists in all the models, which indicates during pure diffusion dissolution process, small pores either on the surface or inside particle does not contribute to the mass transfer comparing to the outside of the particle. This conclusion is confirmed by plotting dissolution release profile in

Figure 4.5. Implemented pictures are magnification of release profile at different stages.

The conclusion from this simulation is based on the assumption that no disintegration happens due to the pore structure. Real disintegration cannot be simulated by *DigiDiss* because of the limitation of the code. However, in most of the cases, disintegration happens when porous particle dissolving in water and the mechanism for disintegration still needs further investigation. Once disintegration happens, particle breaks into smaller parts, and dissolution time significantly changes due to the reduction of particle size. In the other words, pore structure can affect particle dissolution in a considerable way. Further research needs to be investigated in order to fully understand the effect of pore structure on dissolution process.

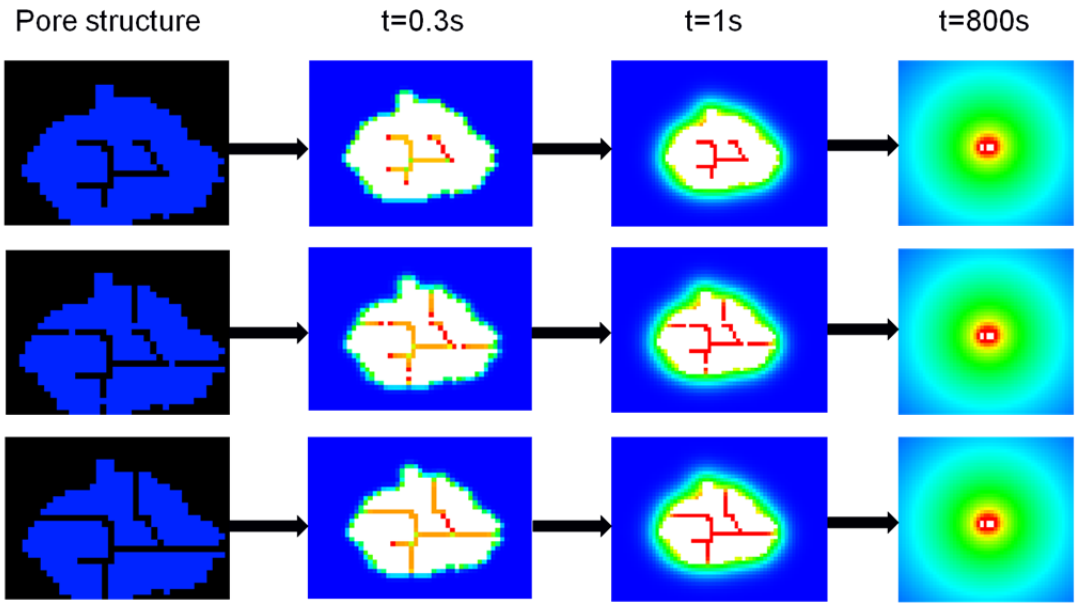

Figure 4. 4 Concentration distribution development as a function of dissolution time on cross-section with pores. Top row is close-end pore inside particle. Second row is close-end pore inside particle and on particle surface. Bottom row is open-end pore.

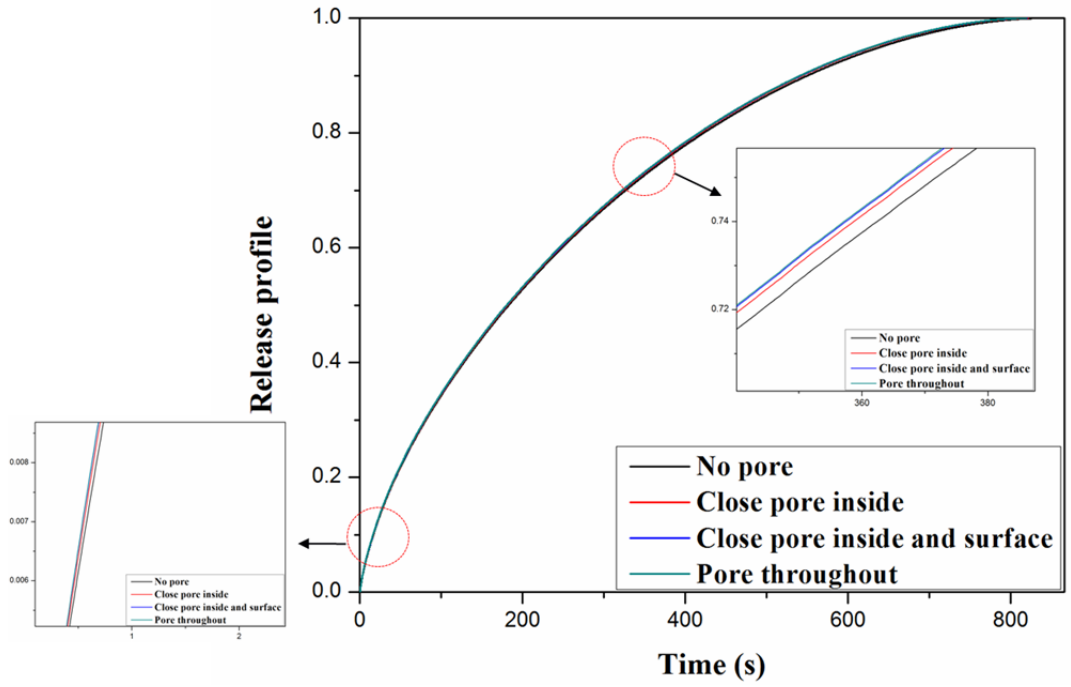

Figure 4. 5 Release profile of Na2CO3 granule with different pore structure. Implemented pictures are magnified pictures of release profile at different stages.

4.4 Experiment and simulation of agitation effect on convective dissolution

In previous sections, all the simulation were run in diffusion model where water was stationary around particle, this is because:

1) by simplifying simulation condition can help to understand how parameters (particle shape, surface area to volume ratio, pore structure etc) affect dissolution independently;

2) mass transfer of convective dissolution is more complex comparing to diffusion dissolution.

In this section, the experiment of convective dissolution was carried out by merging a single granule into stirring water. Then the experiment was simulated by COMSOL to understand how shear rate around particle affect dissolution.

4.4.1 Experiment of single granule convective dissolution

Frame images from high speed camera video are shown in Figure 4.6 where Na_2CO_3 granule sits on top of the magnetic stir with a distance of 2.4 mm between the sample holder and stir. The particle holder was driven to the position by a motor. Once particle touching water, dissolution started. Hence, 1 mm in diameter is chosen as the starting point for analyze. After dissolving 117 s from the starting point, particle was blown away from the holder. By using ImageJ to calculate particle area in the images, result shows that 68% of the total weight is reduced during this time period.

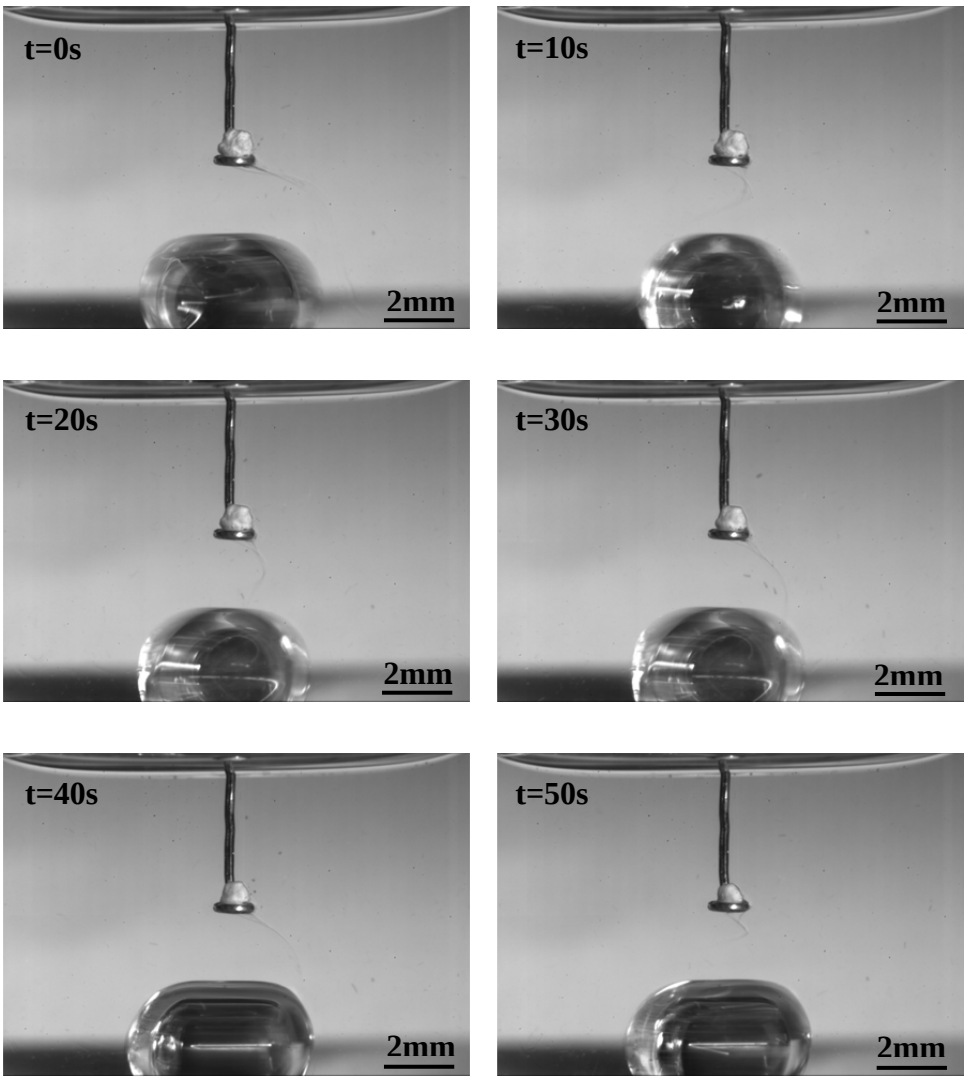

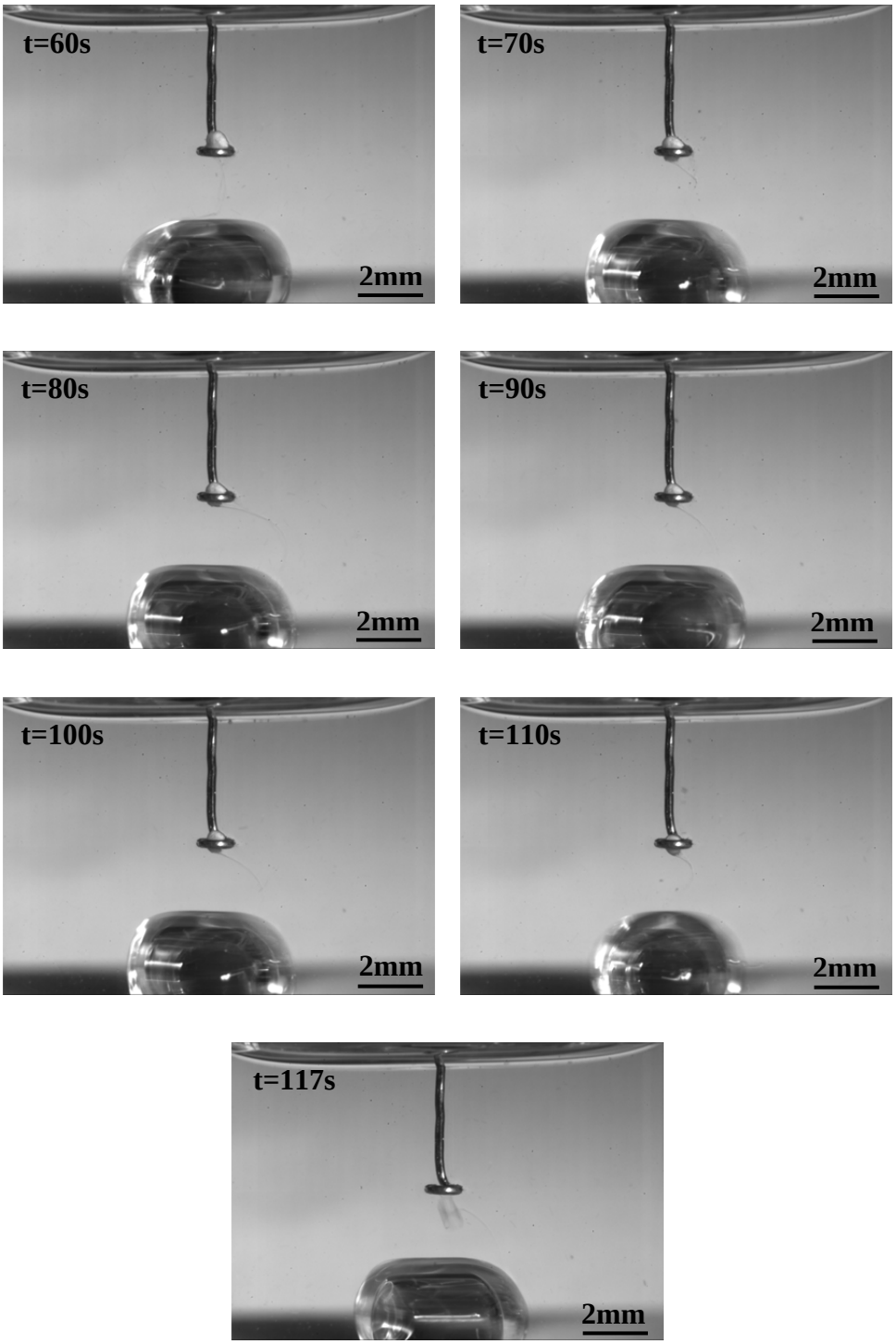

Figure 4. 6 Image snapshots from high speed camera video of Na2CO3 granule dissolves on top of magnetic stir.

Comparing experiment of Na_2CO_3 granule sitting beside the stir are shown in the following Figure 4.7. Same starting point is chosen for analyze. The distance between the tip of stir and sample holder is 0.8 mm. Different from the previous

experiment, after dissolving 91 s, particle was blown away from the holder, which is 16 s faster. ImageJ result shows that 78% of the total weight is reduced.

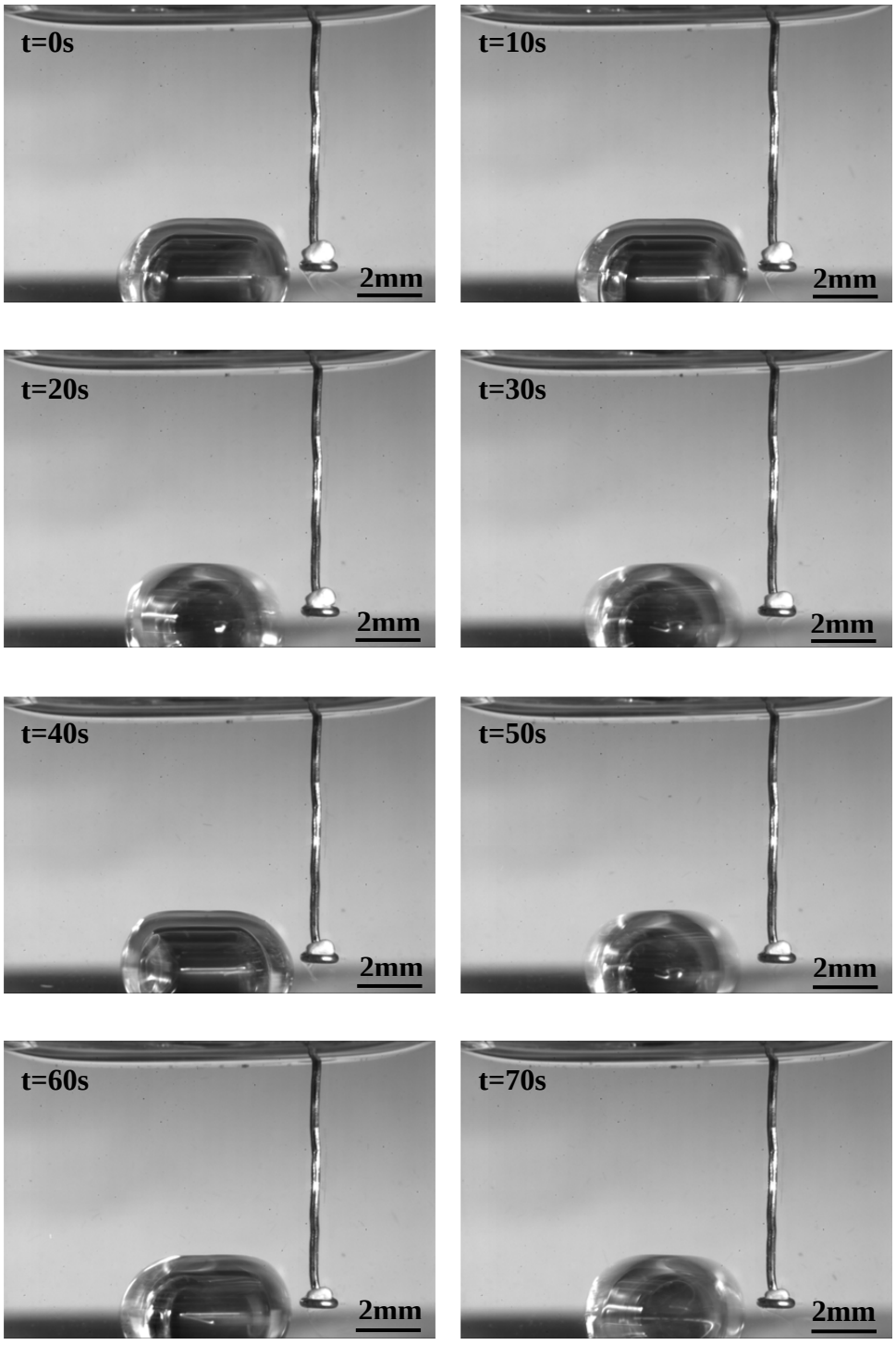

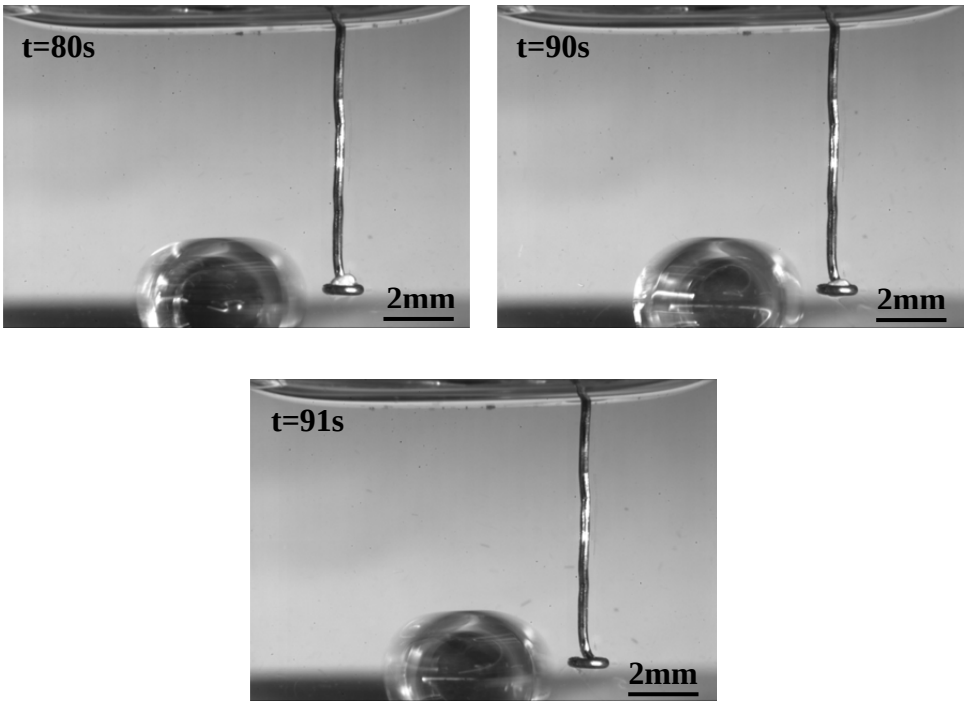

Figure 4. 7 Image snapshots from high speed camera video of Na2CO3 granule dissolves beside magnetic stir.

As reviewed in Chapter 2, agitation plays an important role in dissolution. This is mainly related to the shear rate generated by agitation around particle. When it is on top of the stir, shear rate around the particle is smaller than beside the stir. This is proved by the COMSOL simulation results showing in Figure 4.9 and 4.10. Figure 4.9 and 4.10 also show the velocity magnitude distribution in the stirring system. As an indication that simulation achieving equilibrium state, total volume average shear rate is plotted as a function of time in Figure 4.8. After the stir rotates 4 s, shear rate stops changing and the fluid system achieves the equilibrium state.

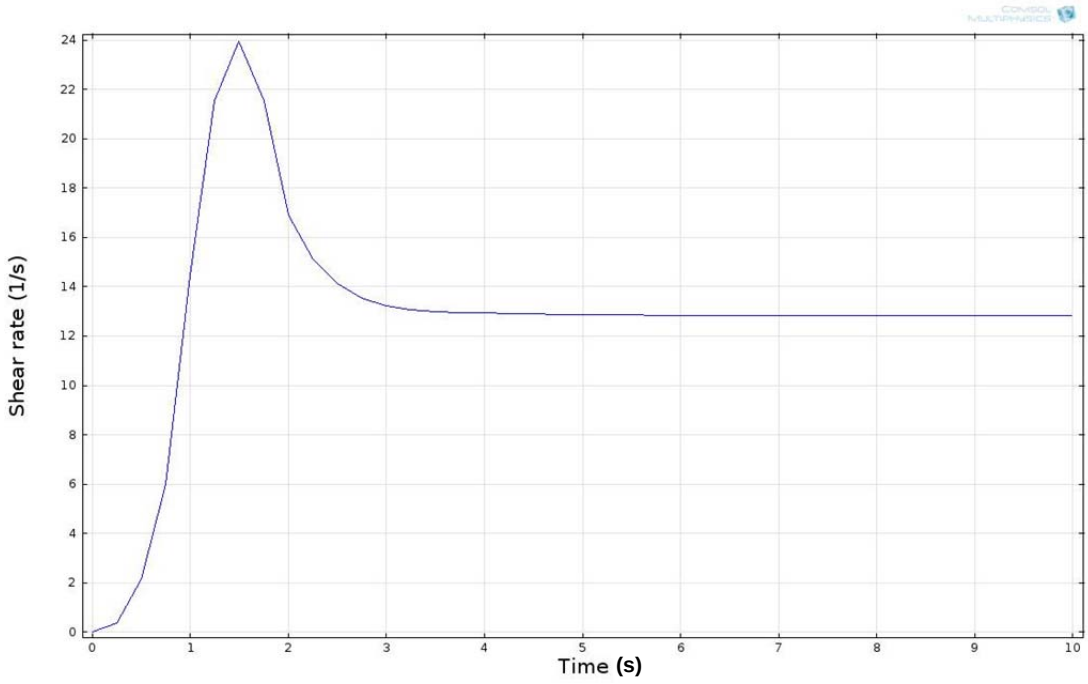

Figure 4. 8 Total volume average shear rate changes as a function of time in stirring crucible.

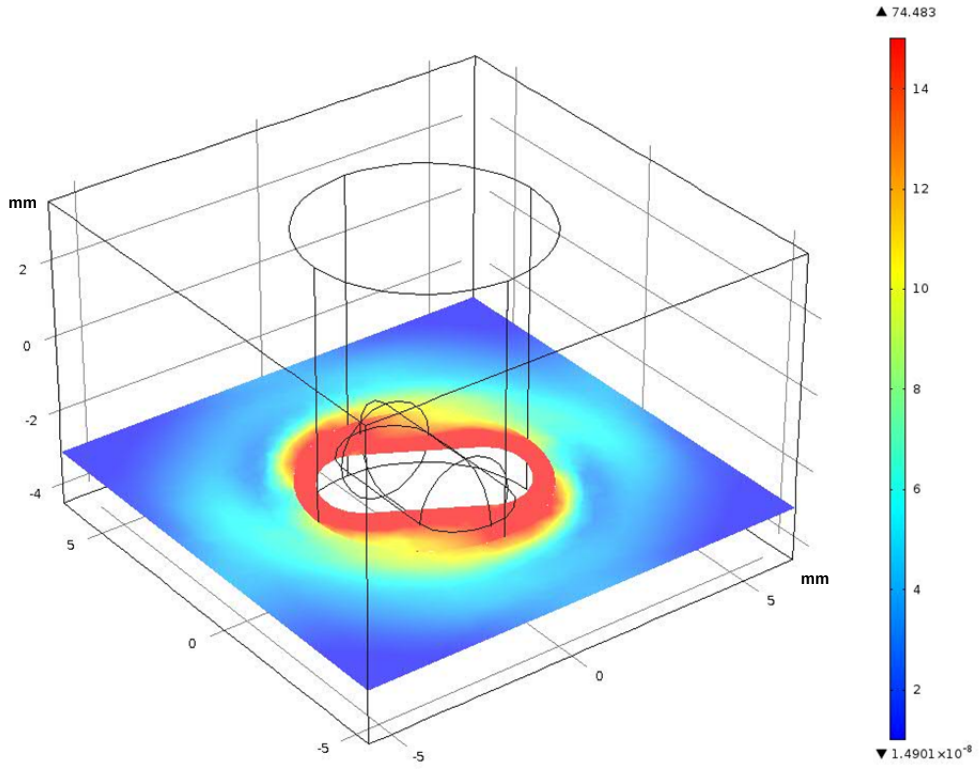

(a)

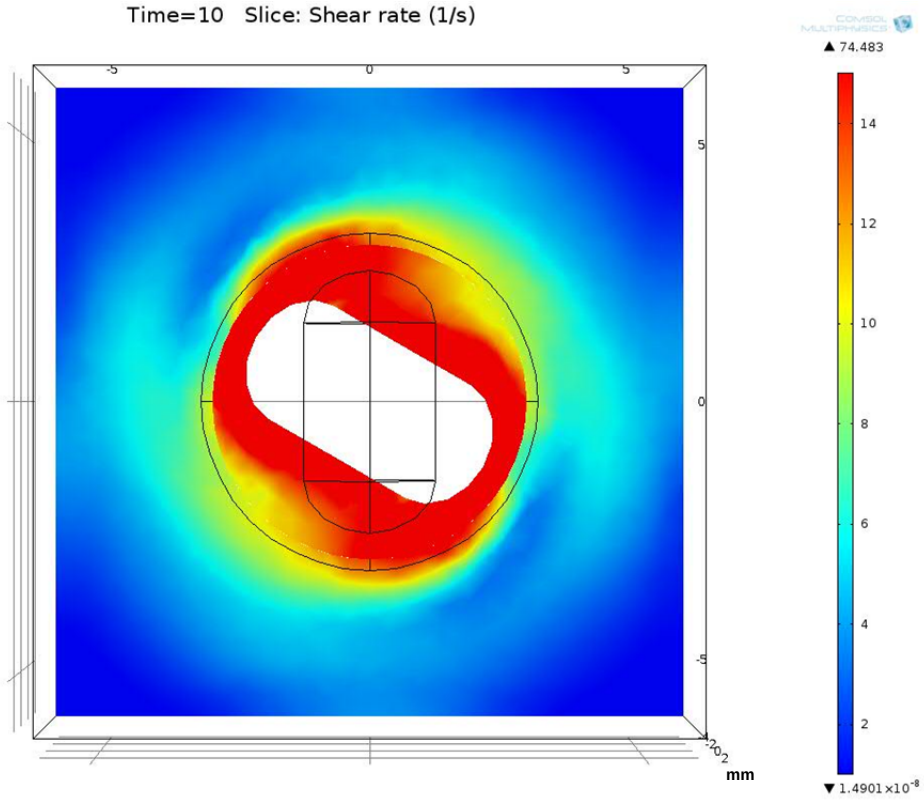

(b)

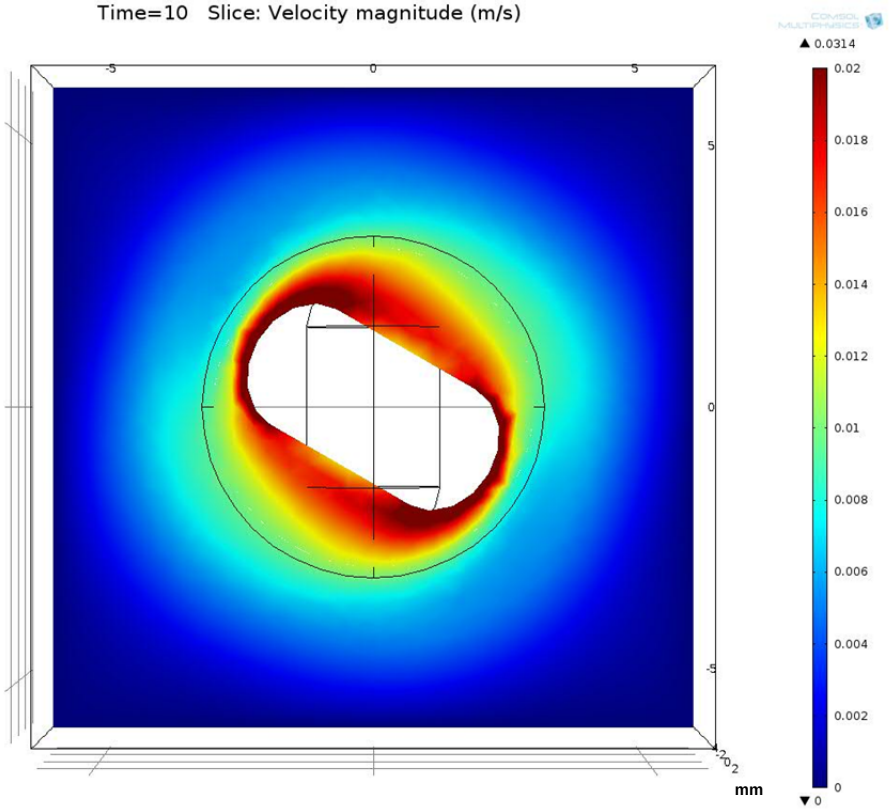

(c)

Figure 4. 9 XY-plane plot of (a), (b) shear rate and (c) velocity at 100 rpm.

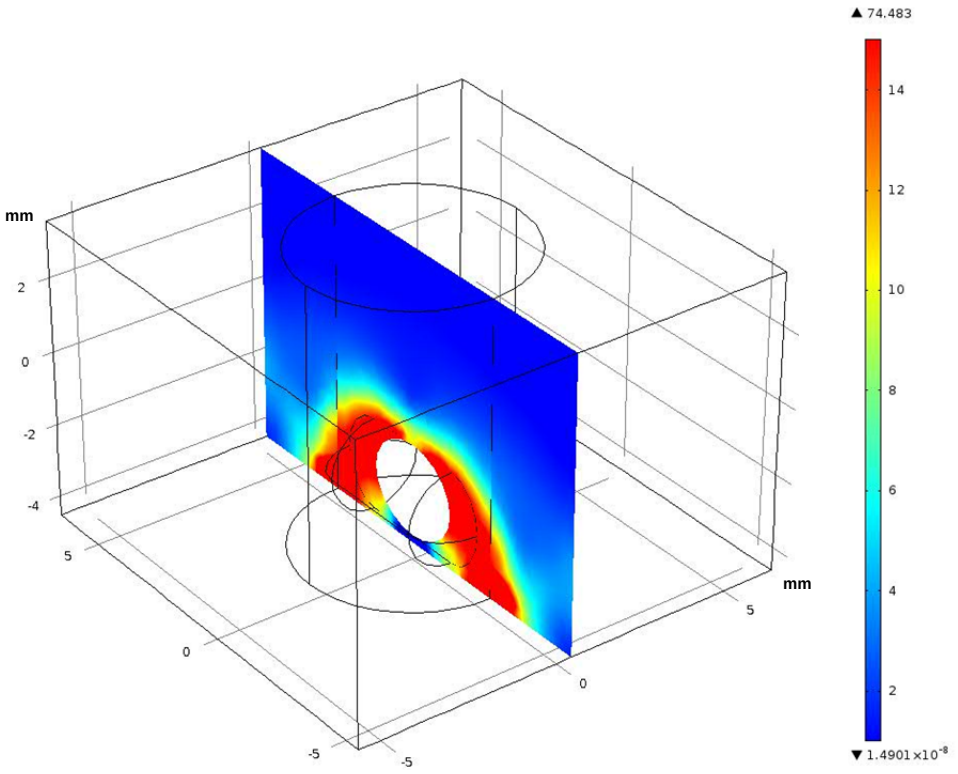
▲ 74.483
14
12
10
8
6
4
2
▼ 1.4901×10⁻⁸
mm
2
0
-2
-4
5
0
-5
-5
0
5
mm

(a)

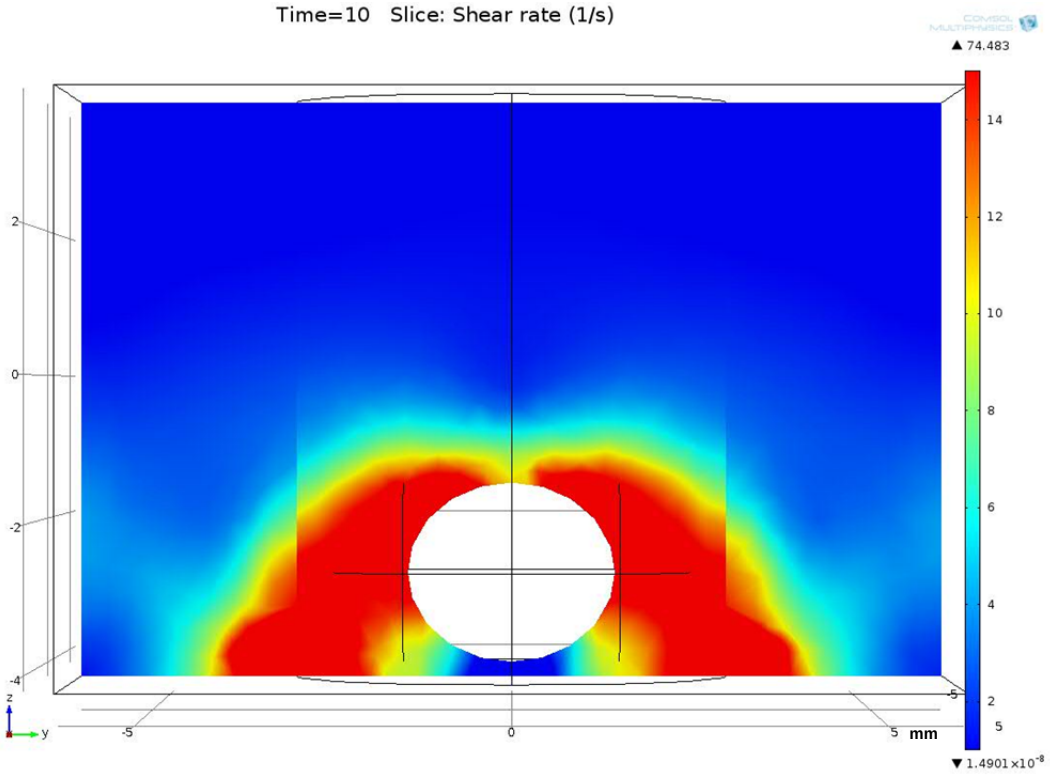
Time=10 Slice: Shear rate (1/s)
▲ 74.483
14
12
10
8
6
4
2
5
▼ 1.4901×10⁻⁸
2
0
-2
-4
z
y
-5
0
5
mm

(b)

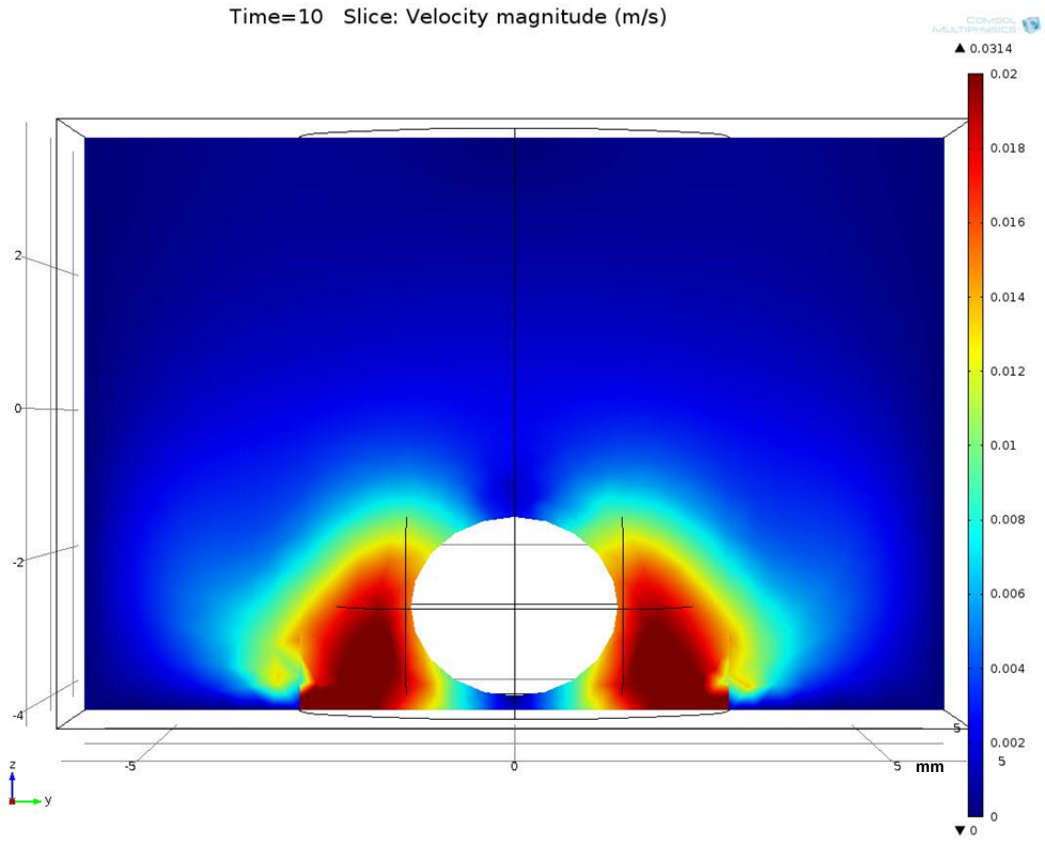

(c)

Figure 4. 10 YZ-plane plot of (a), (b) shear rate and (c) velocity at 100 rpm.

In Figure 4.9 and 4.10, (a) shows the position of the plane chosen for plotting, (b) is the slice plot of shear rate distribution on the plane, and (c) is the velocity distribution. Blue colour represents low value, and red colour represents high value. The whole shear rate in the model distributes from 0 to 74.483 1/s, and velocity magnitude distributes from 0 to 0.0314 m/s. In most of the area far away from the stir, for example on the top of the water surface or the edge (corner) on the crucible bottom, shear rate is around 0 1/s, same as the velocity. The closer to the stir, the higher the shear rate and velocity. At the very close position, for example the circle where the tips of the stir pass through, both shear rate and velocity significantly increase.

It is not difficult to find out from Figure 4.9 and 4.10 that when the particle is 0.8 mm beside the stir, shear rate around it is between 8 to 15 1/s, velocity is 0.008 to

0.012 m/s. While it is 2.4 mm on top of the stir, shear rate is around 1 1/s and velocity is only half or one third of the value beside the stir. Combining experiment results and COMSOL simulation results, one can get a conclusion that high shear rate and velocity around particle make particle dissolves faster.

4.4.2 Simulation of single granule convective dissolution

After looking into the shear rate distribution around particle in detail, the velocity field from COMSOL was imported into *DigiDiss* to simulate convective dissolution of single Na_2CO_3 granule.

The geometry in two models are identical, however, the mesh types are different. *DigiDiss* is LBM, and structured grid hexahedron is chosen in 3D model. COMSOL is a software based on FEM which offering popular options for example tetrahedron, hexahedron and customer defining regarding mesh types.

The mesh type in COMSOL is tetrahedron. When exporting velocity field, regular structured grid is chosen in order to match the grid in *DigiDiss*.

Figure 4.11 shows the velocity field in *DigiDiss* after importing from COMSOL, (a) is 3D view, (b) is cross-section and (c) is top view. Blue colour represents low velocity, red colour is high velocity, and others are in between. The colour legend in Figure 4.11 is slightly different from Figure 4.9 (c) and Figure 4.10 (c). This is mainly due to mesh distribution difference between these two codes and also the set up of colour legend.

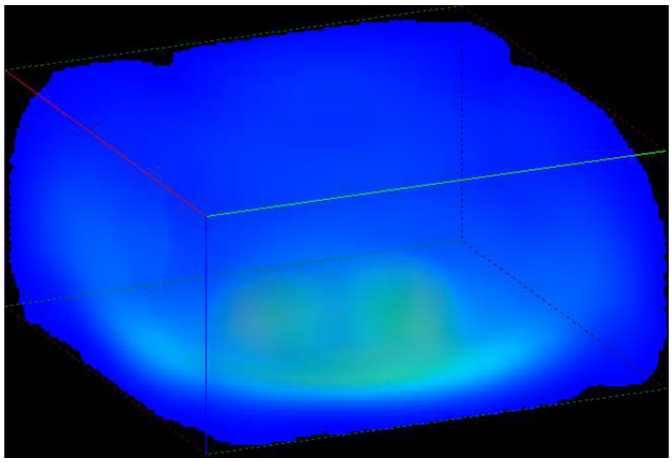

(a)

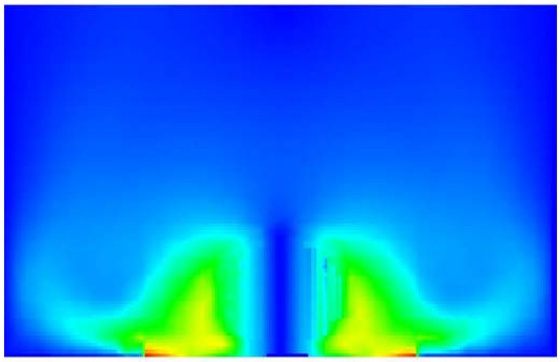

(b)

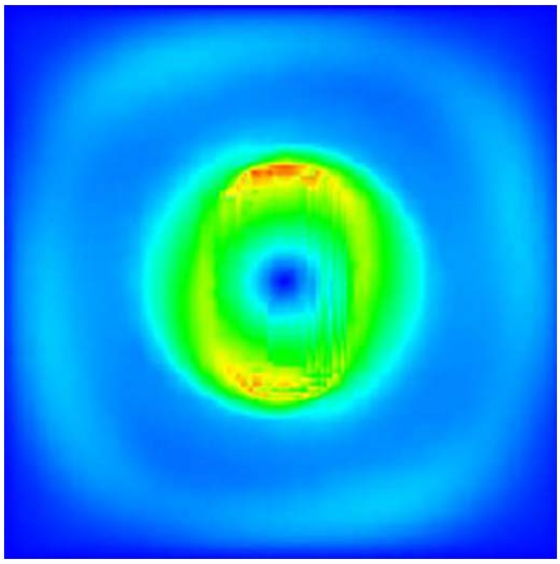

(c)

Figure 4. 11 Velocity field in DigiDiss (a) 3D view (b) cross-section view and (c) top view.

After importing the velocity field, 3D structure of Na_2CO_3 granule scanned from XRT was input into the model at different positions according to the experiment. The simulation results are shown in Figure 4.12. The total dissolution time for 1 mm Na_2CO_3 granule in water without stirring is 837s. With 100 rpm stirring rate, on top of the stir, total dissolving time is 200 s which is 5 s longer comparing to beside the stir. This is due to the different shear rate around the particle which has been explained in the previous section. The simulation results show qualitatively agreement with the experiment results.

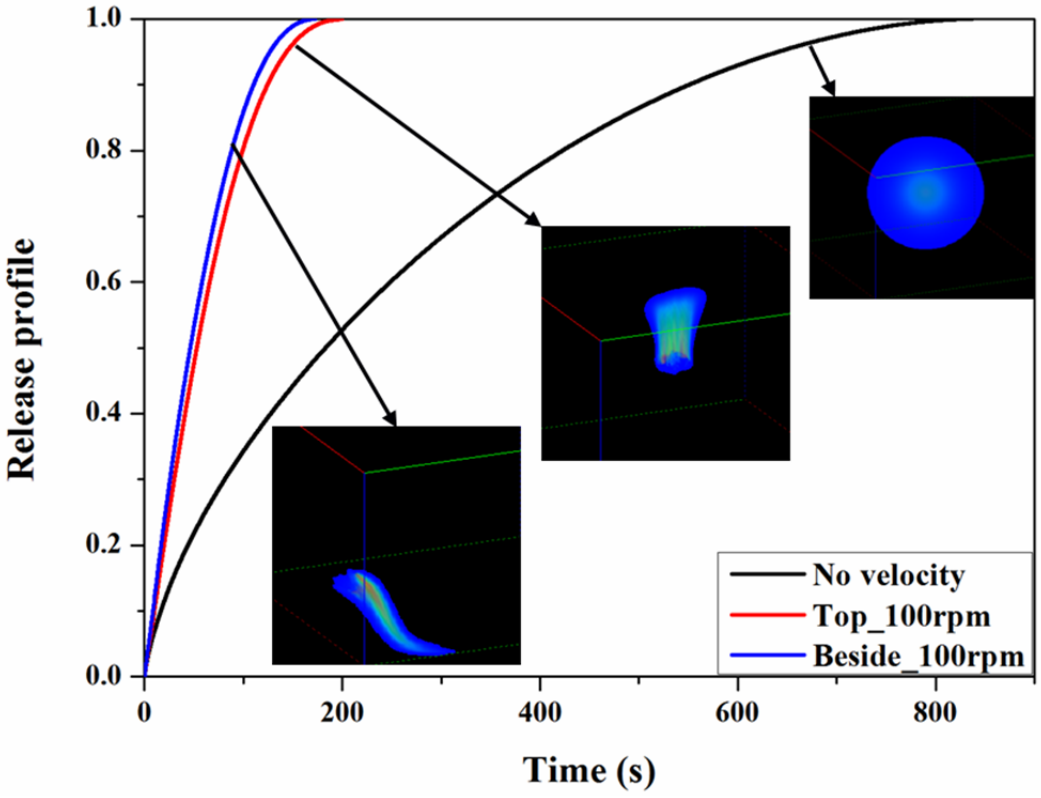

Figure 4. 12 Release profiles from *DigiDiss* simulation results of Na_2CO_3 granule dissolving in a magnetic stir at 100 rpm. The embedded pictures are concentration distribution in water during dissolution, from left to right are granule beside the stir, on top of the stir and no stir.

The embedded pictures are Na_2CO_3 concentration distribution in water. The one on the right represents no stir. Blue colour is where low concentration is, and red is where high concentration is. Without stirring, concentration is uniformly distributed from the center of particle to the water with highest concentration in the middle and

lower in the outside. The other two are in stirring water. With water flowing around particle, the distribution of concentration reflects water flow pattern. The picture on the left is when particle is beside the stir, and the one on the right is when particle is on top of the stir. Because the water flow pattern at these two positions are different, the concentration distribution are different.

Starting from time 0 s, for particle sitting on top of the stir, a comparable 68% weight loss is captured at 84 s (117s in experiment), while for particle sitting beside the stir, after 83 s 78% of particle weight is lost (91s in experiment). Both these two values show that simulation indicates a faster dissolution process. Several reasons are proposed.

Firstly, the dissolution experiment using imaging technique introduces error into results. Particle shape cannot be guaranteed exactly the same from experiment to experiment. Slight particle shape difference can affect dissolution process. For example in the presented two experiments, after losing 68% and 78% of the weight, both of the residual particles went through the hole in the sample holder. By using imaging technique, there is 10% different weight loss between them. This is simply caused by experiment error. While in simulation, conditions are more controllable. Particle shape is exactly the same from one simulation case to another. To calculate the respectively 68% and 78% weight loss in simulation, results can be very accurate.

Secondly, the velocity field coupling from COMSOL to *DigiDiss* might not be very precise. In experiment, particle beside the stir dissolves 26 s faster than on top of the stir. However, in simulation, particle beside the stir dissolves only 1 s faster than on top of the stir. After imported into *DigiDiss*, the velocity field is set as initial condition in the model. Throughout the simulation time, this condition remains constant which means the velocity around particle at each grid point is constantly at

the same value. In experiment, the velocity field around particle is always dynamic which might be the reason that particle dissolves slower than simulation. This can be improved in the future by modifying *DigiDiss* code and adding the function of live-time coupling COMSOL simulation result to *DigiDiss*.

Another simulation case has been done is the agitation speed effect on dissolution. First in COMSOL, same model but 200 rpm has been simulated and the velocity field was imported into *DigiDiss* as initial condition. Results are shown in Figure 4.13.

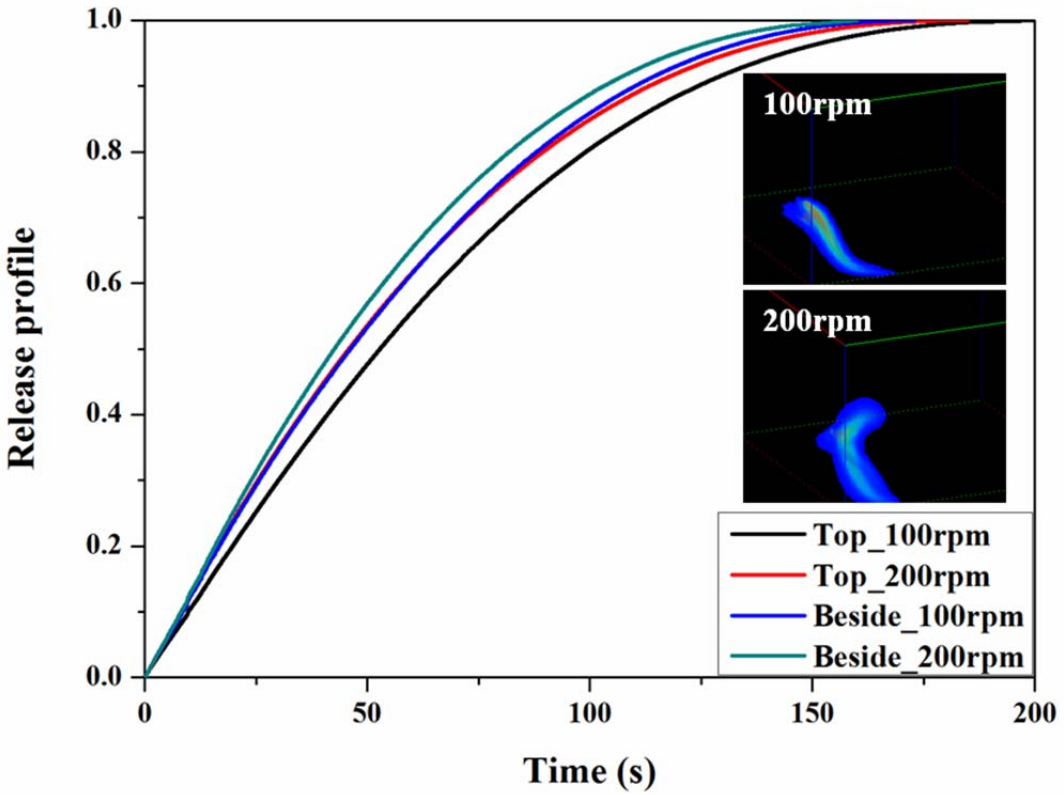

Figure 4. 13 Release profiles from DigiDiss simulation results of Na2CO3 granule dissolving at different agitation speed. The embedded pictures are concentration distribution in water during dissolution, top one is 100 rpm beside stir, bottom one is 200 rpm beside the stir.

It is clearly in Figure 4.13 that with higher agitation speed, dissolution is faster. When the particle is on top of the stir, although shear rate does not change significantly, from about 1 1/s to 2.4 1/s with agitation speed from 100 rpm to 200

rpm, the total dissolution time changes from 200 s to 185 s. Same result is obtained with particle beside the stir.

The embedded pictures are concentration distribution when particles are beside the stir. Top one is 100 rpm and bottom one is 200 rpm. Both of these distribution show agreement to the flow pattern. The 200 rpm one has a wider distribution comparing to the 100 rpm one probably due to the higher shear rate around the particle.

4.5 Experiment and simulation of wetting process

Wetting process plays an important role in detergent powder dissolution. Normally pores size of detergent powder is from 20 μm to 100 μm. With this micro-sized pores, investigation of wetting by experiment is challenging considering powder start dissolving immediately when it contacts water. Besides, parameters for example contact angle, pore size, liquid surface tension all affect wetting speed in different ways.

In this section, experiment of water penetrating into macro-sized capillary tube was carried out. Capillary tube was coated with chemical TMCS (one of the silanol family) to change the surface from hydrophilic to hydrophobic. Then the model of COMSOL simulation was verified by experiment and the prediction of modelling was done to understand wetting of micro-sized pores.

4.5.1 Experiment of capillary penetration

Atomic Force Microscope

After coating with TMCS, small cracked pieces of glass tube was used to perform AFM test. Figure 4.14 are three-dimensional AFM images of the inner side of the glass tube, (a) and (b) are surface without modification, and (c) and (d) are TMCS

modified surface. (a) and (c) are 2D surface morphology, and (b) and (d) are 3D images of the surface. The root-mean-square (RMS) roughness value of the films was analyzed with AFM. The surface of TMCS modified glass tube is slightly rougher than the unmodified one, with a RMS roughness value of 7.8 nm and 15.1 nm, respectively. This result shows that the process of TMCS coating on it doesn't change the surface topography in a remarkable way. However, the silanol groups on capillary surface modified the glass surface from hydrophilic to hydrophobic which affects the wetting process significantly.

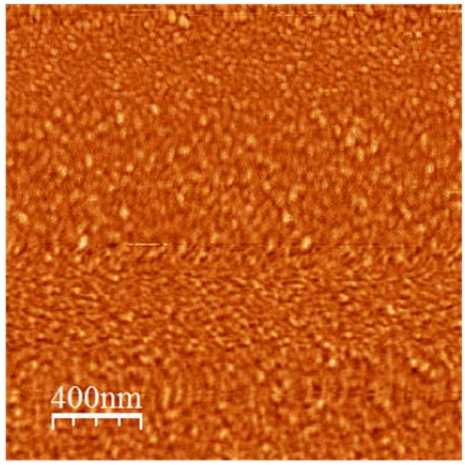

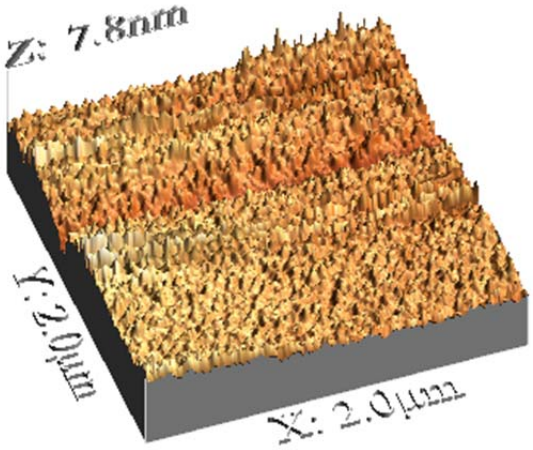

(a) **(b)**

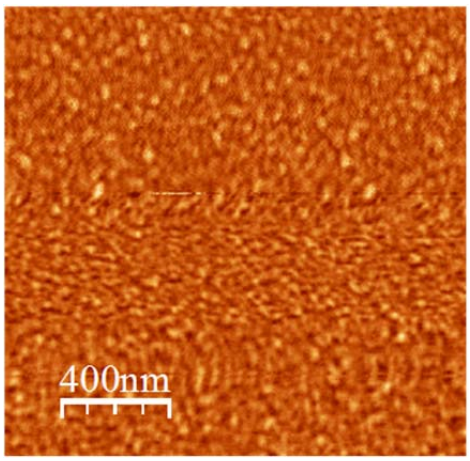

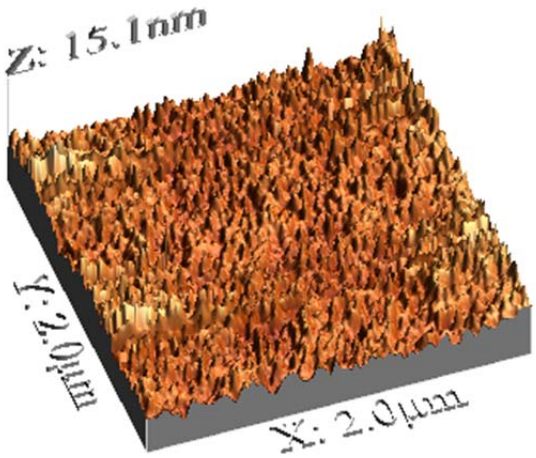

(c) **(d)**

Figure 4. 14 AFM tomographic images of (a) and (b) unmodified capillary tube surface (hydrophilic), (c) and (d) TMCS modified capillary tube surface (hydrophobic).

Capillary Penetration

A set of penetration images are extracted from a typical high speed camera video and shown in Figure 4.15. With 2000 frame per second, it is easy to capture the whole movement of liquid/air interface from initial to equilibrium stage. The track of the interface position was then plotted in diagrams as penetration length (height) vs time.

The experiments were performed in capillary tubes with radius 0.34 mm, 0.45 mm and 0.56 mm. Different aqueous fluids, properties shown in Table 3.1, combining hydrophilic and hydrophobic glass tube, result in very detailed investigation including parameters such as contact angle, surface tension and pore size. Results are shown in Figure 4.16 and 4.17.

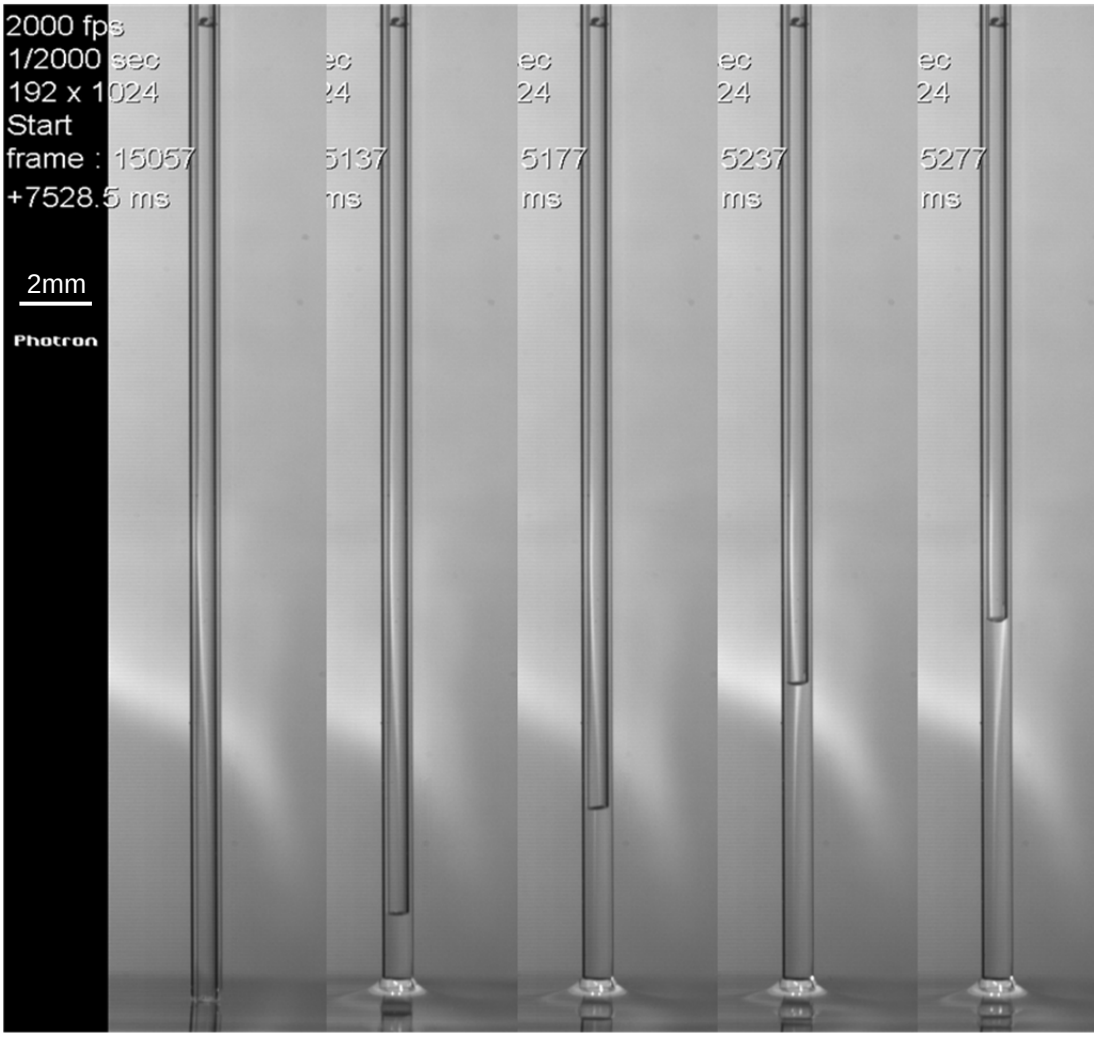
2000 fps
1/2000 sec
192 x 1024
Start
frame : 15057
+7528.5 ms
2mm
Photron

Figure 4. 15 A set of images from high speed camera video show liquid penetrating height changes with time.

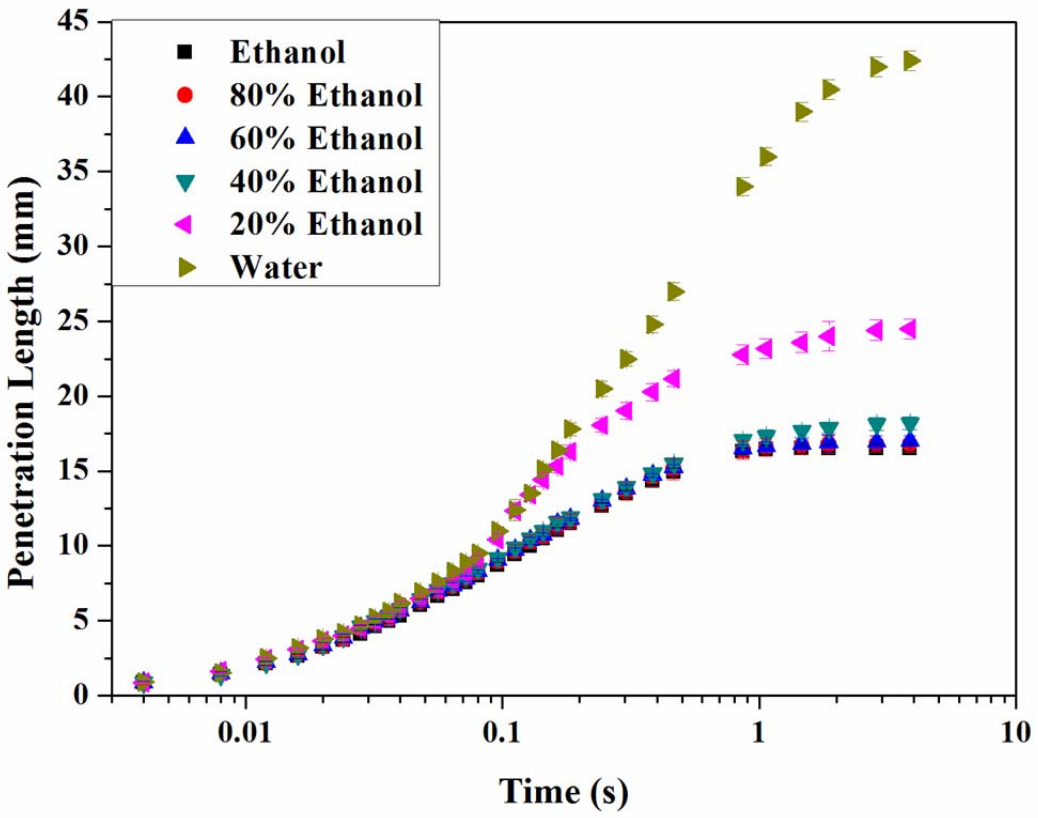
Ethanol
80% Ethanol
60% Ethanol
40% Ethanol
20% Ethanol
Water
Penetration Length (mm)
Time (s)
0
5
10
15
20
25
30
35
40
45
0.01
0.1
1
10

(a)

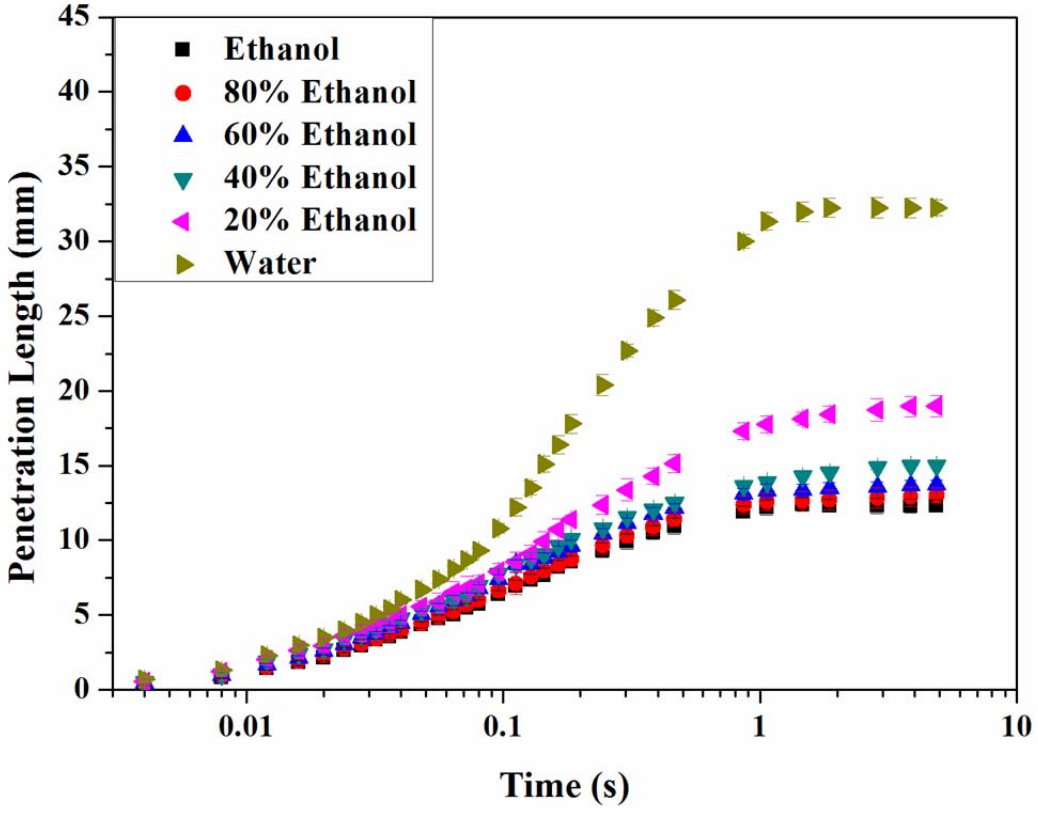
Ethanol
80% Ethanol
60% Ethanol
40% Ethanol
20% Ethanol
Water
Penetration Length (mm)
Time (s)
0
5
10
15
20
25
30
35
40
45
0.01
0.1
1
10

(b)

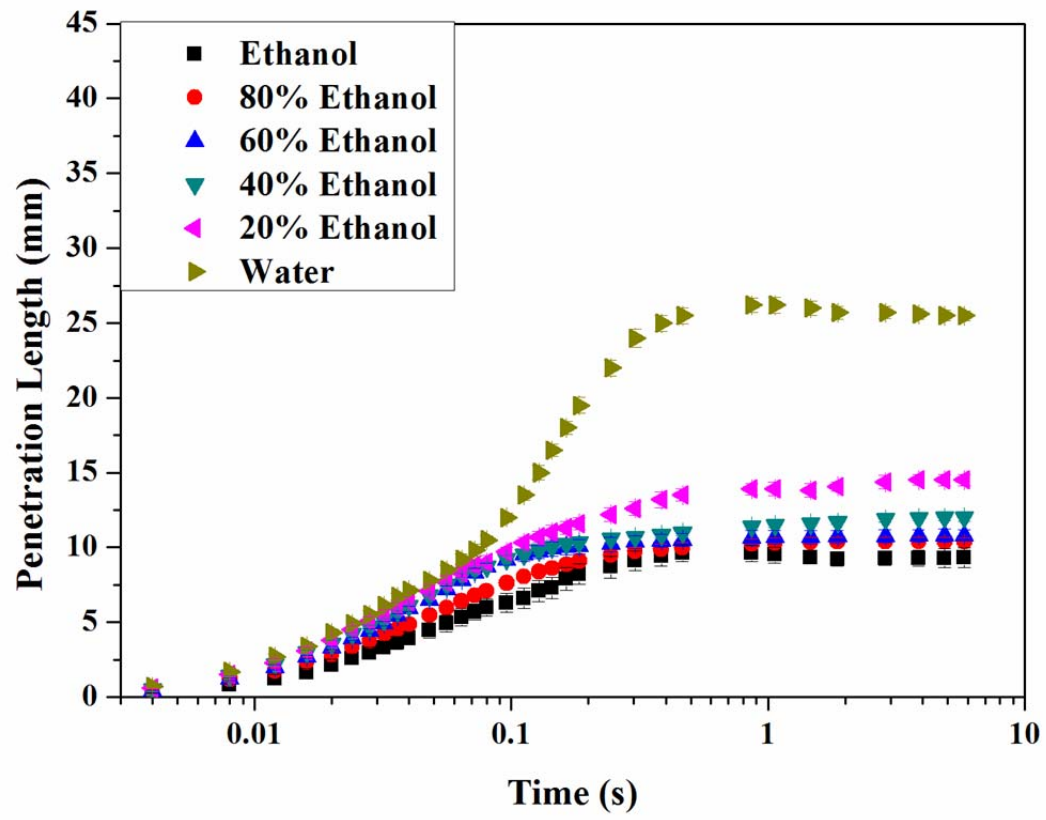

(c)

Figure 4. 16 Experimental results of liquids penetrating into unmodified capillary glass tube for radius of (a) 0.34 mm, (b) 0.45 mm and (c) 0.56 mm.

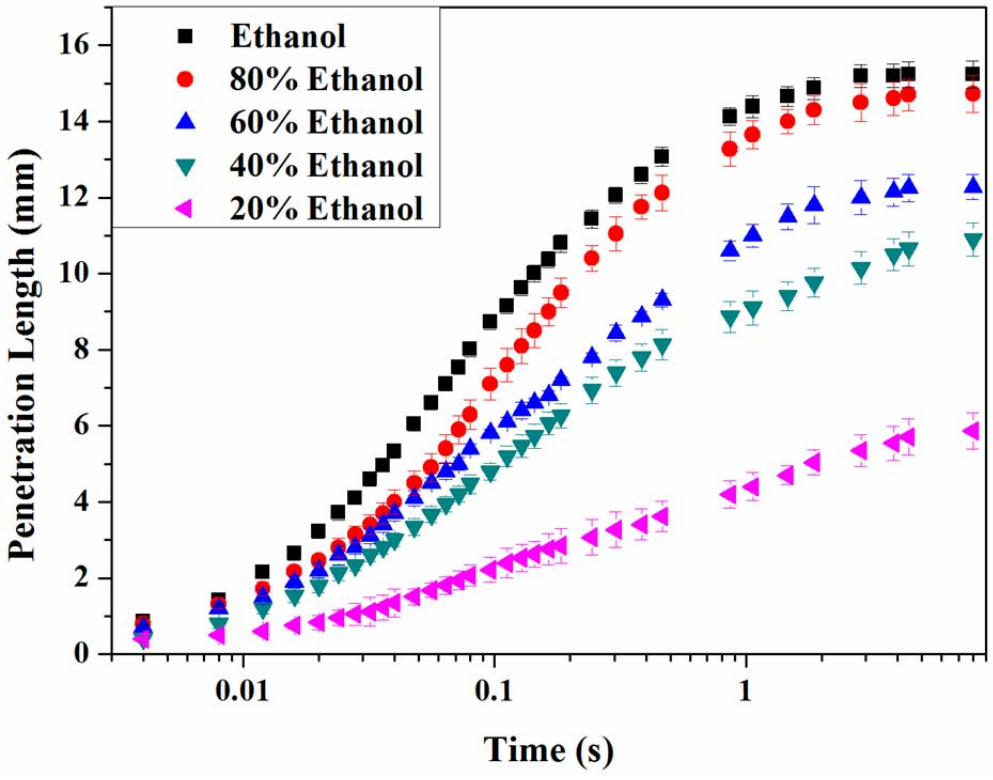

(a)

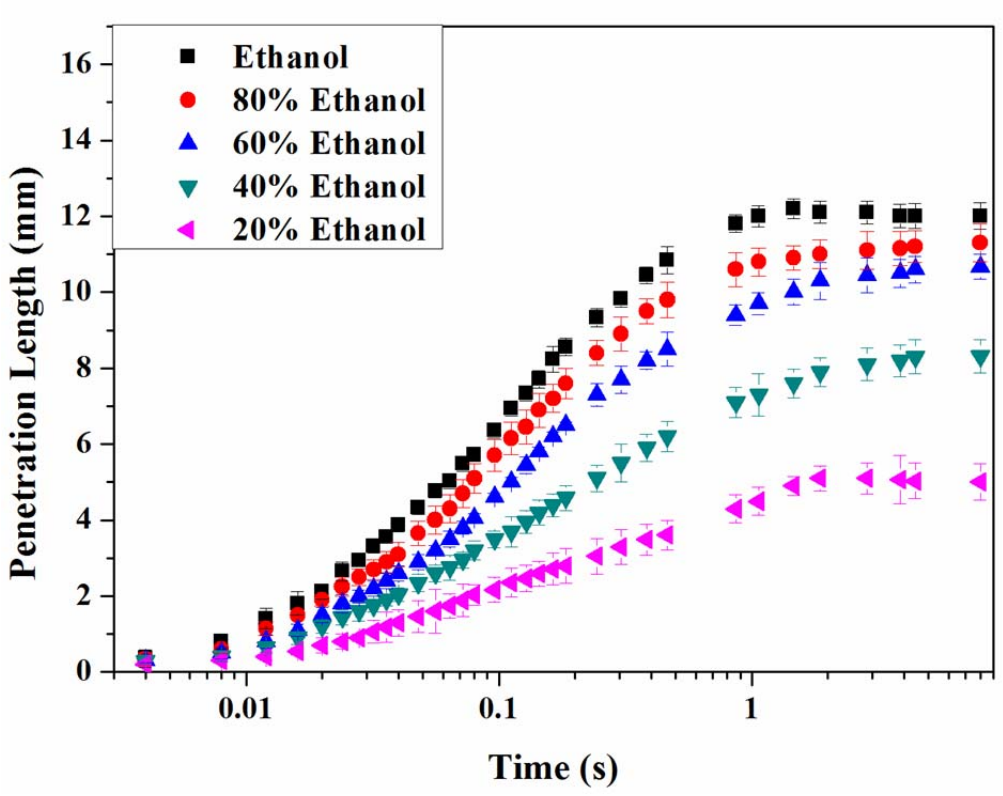

(b)

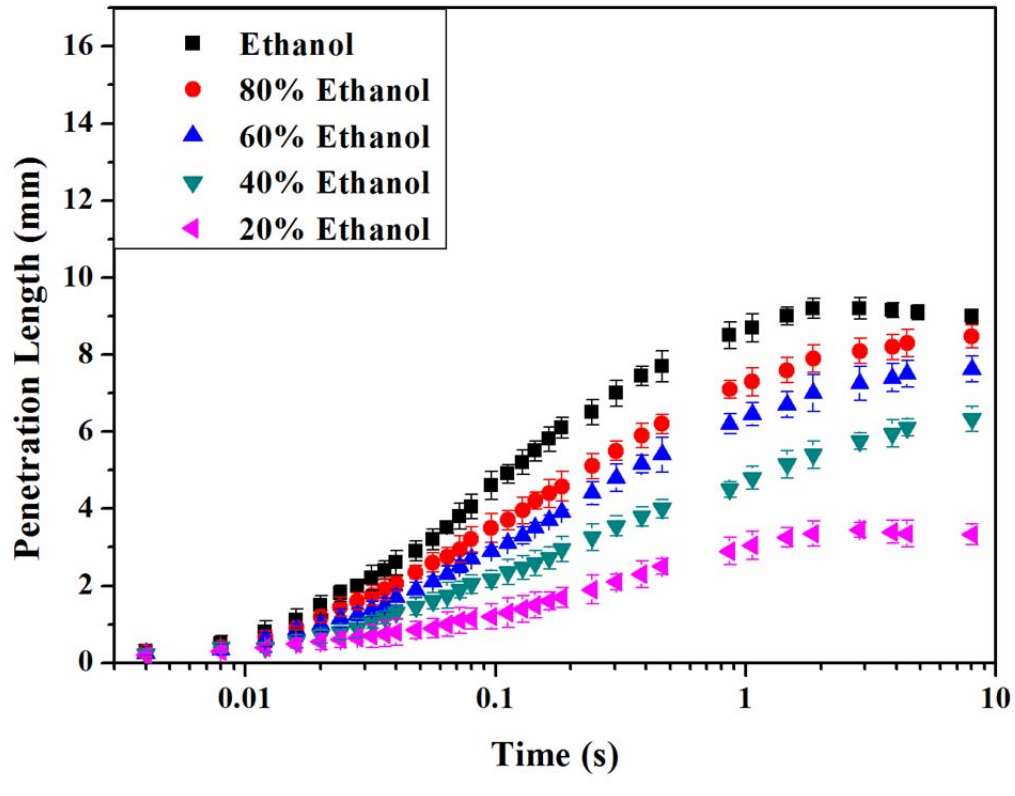

(c)

Figure 4. 17 Experimental results of liquids penetrating into TMCS modified capillary glass tube for radius of (a) 0.34 mm, (b) 0.45 mm and (c) 0.56 mm.

Figure 4.16 shows experiment results of capillary penetration on hydrophilic surface. Figure 4.17 is the results on hydrophobic surface. The diagrams are plotted in Logarithm time mainly to enhance the trends. (a), (b) and (c) are radius of 0.34 mm, 0.45 mm and 0.56 mm respectively. Once liquid goes inside tube, it rises up very fast in the initial stage and then slow down until equilibrium stage is achieved. After measuring the equilibrium height in each case, using Equation 2-21, the equilibrium contact angle θ_{eq} can be calculated.

It is noticeable that, for the same liquid, penetration speed is much higher in hydrophilic surface than hydrophobic surface due to the negative surface energy on hydrophobic surface. Besides, water does not rise up to hydrophobic capillary tube at all suggesting an contact angle for water on TMCS modified surface is bigger than 90°. However, ethanol and ethanol/water mixture can still go into hydrophobic capillary tube.

As reviewed in Chapter 2, Lucas-Washburn equation points out that the dynamic height of capillary rise (vertical penetration) is proportional to $\sqrt{t}$. However the equation neglects variations of the dynamic contact line with speed, and assumes it constantly equalling to the equilibrium contact angle θ_{eq} . In the meantime, some terms for example the gravity effects, the kinetic effects, the viscous loss in liquid below the tube, and the viscous loss associated with the entrance effects, have been neglected [46]. Consequently, this equation cannot be used for the initial capillary dynamics and the equilibrium stage.

By calculating $\gamma \cos\theta_{eq} / \mu$ in Equation 2-22 for different liquid, it is not difficult to find out that this value first decreases with increasing ethanol volume ratio in water and then increases after 60% of ethanol in water. Nevertheless, the experiment

results are different from such a trend, in contradiction with Washburn's approach. On hydrophilic surface, the more ethanol in water, the lower penetration speed is, which is opposite on hydrophobic surface. Researchers have proposed that during capillary rise process, the contact angle, also named as advancing contact angle θ_{ad}, changes significantly before the meniscus stabilize, which could dominate the process [44, 46, 122]. Consequently, advancing contact angle should be used instead of equilibrium contact angle.

Another contradictory result between hydrophilic and hydrophobic capillary is the equilibrium height as a function of ethanol volume ratio in water as plotted in Figure 4.18. On hydrophobic capillary, low ethanol mixtures show lower equilibrium height than high ethanol mixtures which is in the opposite direction of hydrophilic capillary. As increasing ethanol content in mixtures, surface tension reduction governs in hydrophilic capillary. While in hydrophobic capillary, it is the larger drop in contact angle as ethanol increases essentially affects the height.

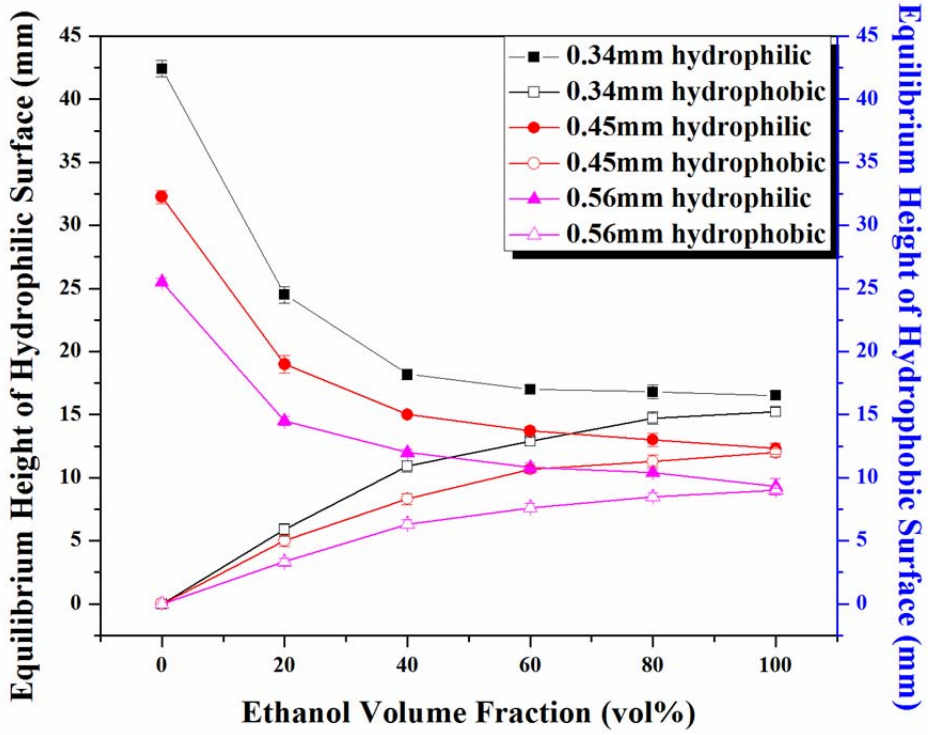

Figure 4. 18 Equilibrium height as a function of ethanol volume ratio on hydrophilic and hydrophobic surface.

It is also seen that throughout the experiment, some oscillation occurred around the equilibrium status. The oscillatory behaviour of liquid column was studied by some researchers [43, 123, 124]. It was shown that kinetic force is the main reason that may cause the oscillation of liquid column. The viscous force is the main reason for damping the oscillatory energy out. It takes time for this kinetic force to damp out by viscous forces, which leads to an oscillatory behaviour at the liquid front around the equilibrium height (Jurin height). The critical radius, R_{cr}, can be determined by:

$$R_{cr} = 2\left(\frac{\mu^2 \gamma \cos\theta_{eq}}{\rho^3 g^2}\right)^{\frac{1}{5}} \qquad 4\text{-}1$$

The Equation 4-1 is identical to an expression reported by Hamraoui and Nylander [123]. The above equation indicates if capillary radius $r > R_{cr}$, the kinetic force is strong enough to rise liquid up the equilibrium height, which leads to oscillation around equilibrium height. According to Equation 4-1, the value of critical radius R_{cr} in the silica capillaries, for water is 0.47 mm, for ethanol is 0.45 mm, and for the mixtures are between 0.56 mm and 0.63 mm. In Figure 4.16 (a) where capillary radius is 0.34 mm, no oscillation occurred around the equilibrium height. In Figure 4.16 (b) where capillary radius is 0.45 mm, a very invisible oscillation occurred of ethanol which can be neglected. However in Figure 4.16 (c) where capillary radius is 0.56 mm, a slightly visible oscillation happened around the Jurin height for both water and ethanol. Similar phenomena happened again in hydrophobic capillaries.

Wettability of hydrophilic and hydrophobic capillaries

In Figure 4.19, the wetting force in the advancing scan, $\gamma \cos\theta_{ad}$ is plotted against the volume ratio of ethanol in the mixtures at time t = 0.1 s. The value of $\gamma \cos\theta_{ad}$ decreased with increasing ethanol concentration for the unmodified capillary tube,

and increased for TMCS modified capillary tube, which agrees very well with the literature [125]. Such a result is more significant by comparing the hydrophilic results to the hydrophobic results in Figure 4.16 and 4.17. The difference of penetration speed for different ethanol/water mixtures of the hydrophobic one is much bigger than the hydrophilic one. Several reasons can be proposed to explain such a phenomenon.

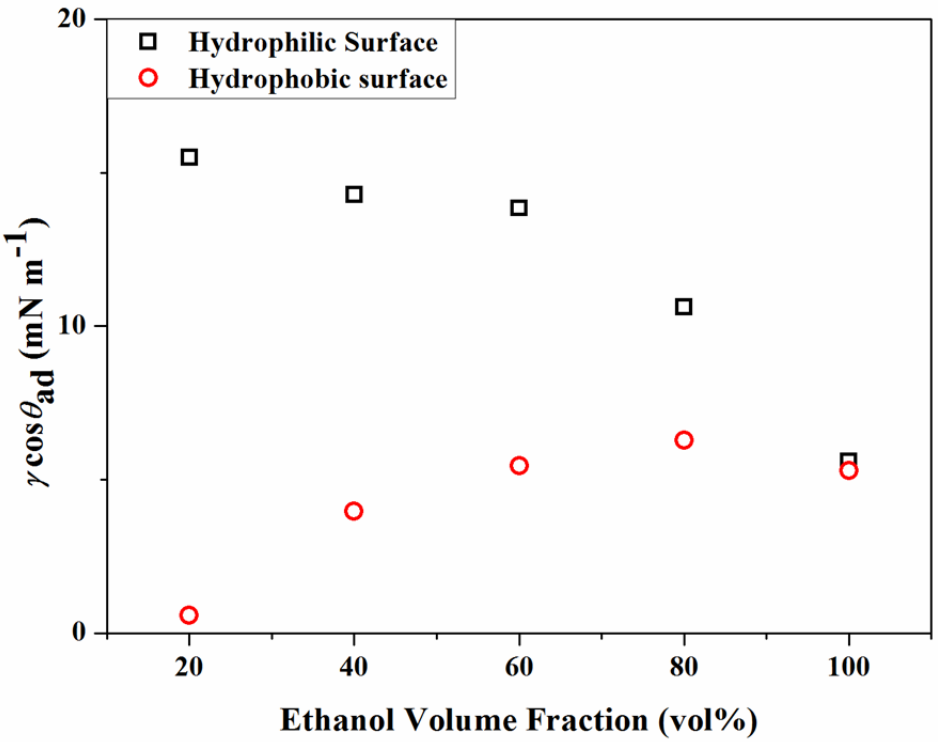

Figure 4. 19 Wetting force as a function of the volume ratio of ethanol in water/ethanol mixtures, at time t = 0.1 s.

After a hydrophilic capillary tube (silica) was silylated by reacting with TMCS, a certain density of silanol groups covered on the tube surface [126] without changing surface tomography as illustrated by AFM results in Figure 4.14. The functional groups (SiOH + TMS) remained quite constant on the surface and made it from hydrophilic to hydrophobic. For the case of pure water penetrating in the unmodified capillary, water can easily form a hydrogen bond on the silica surface due to its high polarity. However, it is difficult for water to form such a monolayer to the surface while it was covered by silanol groups, in which case, water did not penetrate into

the capillary at all. For the case of pure ethanol, the hydroxyl groups (OH) in ethanol molecular can form a weak attractive force on both hydrophilic and hydrophobic surface due to its less polarity. As a result, ethanol can penetrate into both these tubes. However, for the case of water/ethanol mixtures, it is well known that water and ethanol can form different hydrogen-bonding structures. The hydrogen of the OH group on the ethanol may hydrogen bond to an oxygen of a water molecule, form strong hydrogen bonds with water, or hydrogen bond to an oxygen of a ethanol molecule, form a hydrogen bond with another ethanol. Such hydrogen-bonding structures may collapse or dissociate when moving to the different charged surface such as silica, and silanol groups covered silica. According to the results in Figure 4.17, it seems silanol groups prefer less polar OH group in ethanol to water, and caused bigger difference of penetration speed with increasing ethanol volume ratio in water.

4.5.2 Simulation of wetting process

COMSOL Multiphysics two-phase flow module was chosen to simulate liquid penetrating into single straight pore. First the simulation was validated by comparing the results to previous experiment results. Then the model was used to simulate micro-sized pore filling by water.

Validation of capillary filling simulation

The case of 0.34 mm radius experiment was used to validate the model. Three liquid, water, ethanol and mixture of 20 % v/v ethanol and water were used. Both hydrophilic surface and hydrophobic surface was used by setting contact angle in the model as the value calculated from previous experiment. Results are shown in Figure 4.20 and 4.21.

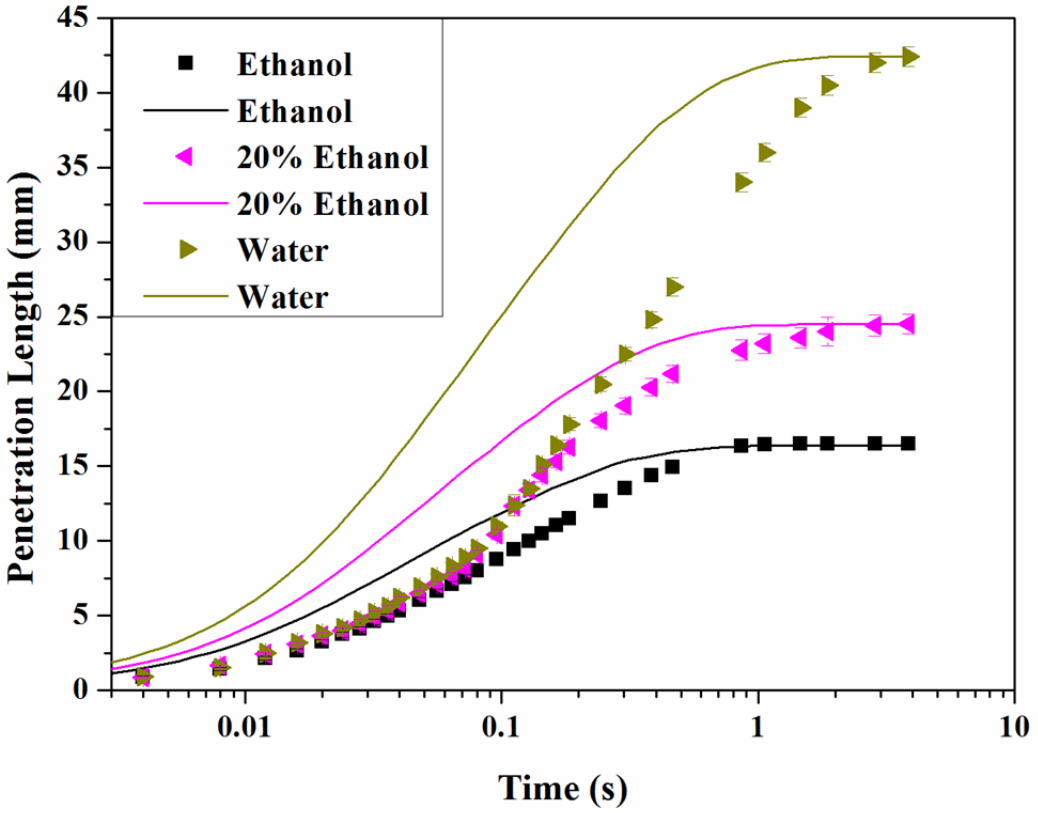

Figure 4. 20 Simulation results compare to experiment results for 0.34 mm radius hydrophilic capillary tube.

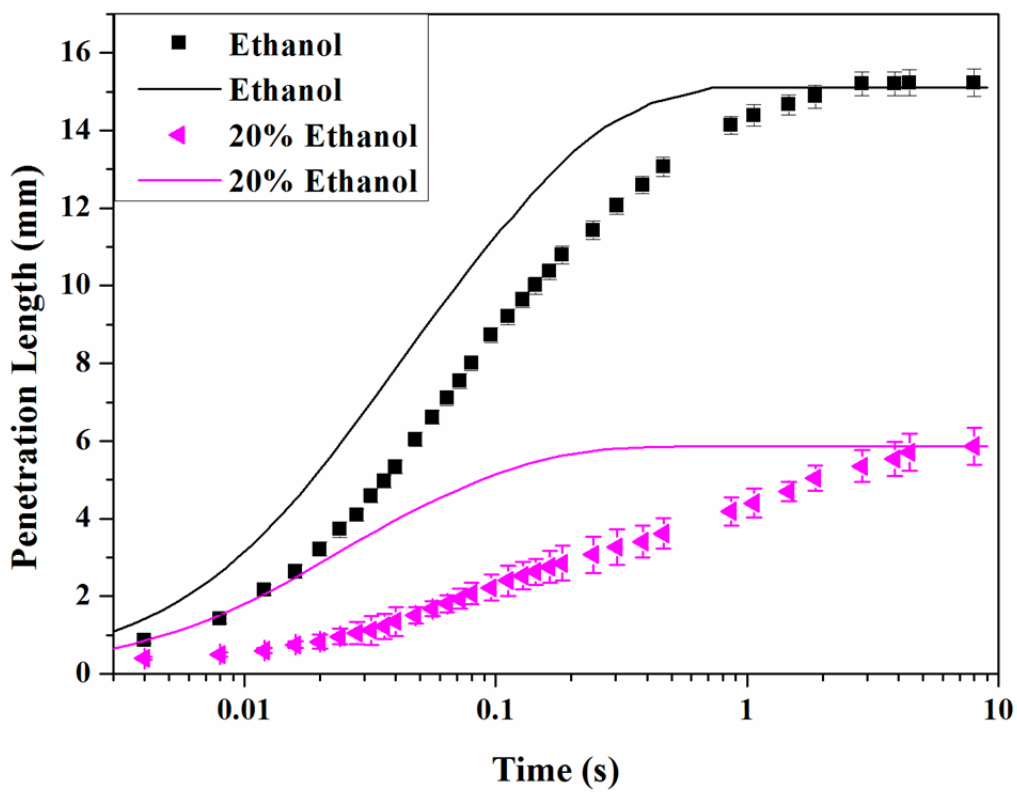

Figure 4. 21 Simulation results compare to experiment results for 0.34 mm radius hydrophobic capillary tube.

Simulation results show same trends as the experiment results that liquid penetrates fast in the beginning, slower later on and finally achieves equilibrium stage. Dots in Figure 4.20 and 4.21 represent experiment data and lines are simulation data. By comparing these data, it is clearly showing that at the final stage, all the lines are with the same height as the dots, which means the equilibrium height from simulation is the same as experiment.

Another noticeable phenomenon is that before achieving equilibrium stage, all the lines are higher than the dots, which indicates that penetrating speed from simulation is faster than experiment. In simulation, liquid reaches equilibrium height earlier than experiment. The main reason which can be used to explain this is the contact angle. As discussed previously, in experiment, advancing contact angle decreasing with time. Contact angle in the modelling was set as the equilibrium contact angle which is a constant value and smaller than advancing contact angle. With a bigger contact angle from the beginning, penetrating speed in experiment is slower.

Simulation of straight pore filling

Although in terms of penetration speeds, simulation results show qualitatively agreement with experiment results instead of quantitatively agreement, the equilibrium height from these two methods are the same. Generally, penetration speed from modelling is faster than experiment, but still in the same order. Therefore, the model was modified to simulate water penetrating into micro-sized pores.

Two typical pore size were chosen, 20 μm and 100 μm in diameter. For this pore size, water can penetrate more than 1 m before achieving equilibrium stage. Pore length in the model was built as 2 mm, far shorter than the equilibrium height, but long enough to represent most of the pore length in detergent powder which

normally has particle size between 100 µm to 2 mm. Contact angle from 0 ° to 60 ° with 20 ° interval were chosen for each case to represent different particle wettability. Simulation results are shown in Figure 4.22 for 20 µm and Figure 4.23 for 100 µm.

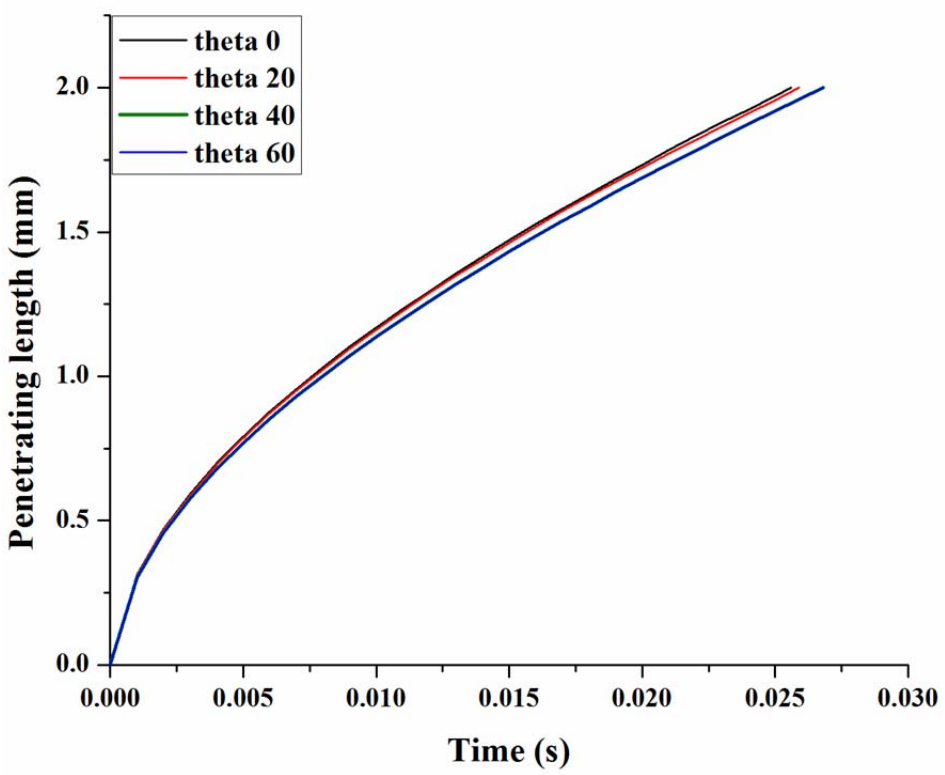

Figure 4. 22 Pore filling simulation of water into 20 µm pore with different wettability.

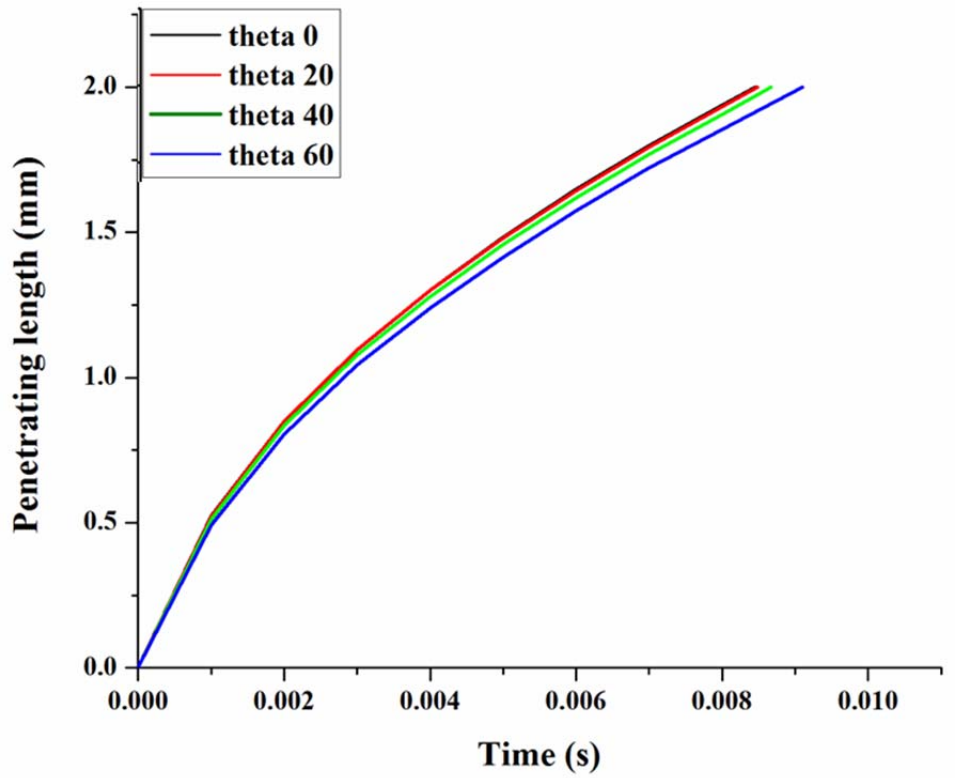

Figure 4. 23 Pore filling simulation of water into 100 µm pore with different wettability.

Both these two figures show logarithmic relationship at the initial stage and develop to nearly linear trends until the pore end. The whole pores were filled by water when simulation finished. The results show that water can penetrate 2 mm in less than 0.03 s for 20 µm pore size and 0.01 s for 100 µm pore size. The total dissolution time for a 1 mm Na2CO3 granule in stirring water is around 100 s according to the experiments carried out in previous section. Obviously the wetting time is negligible comparing to the total dissolution time. Besides, with different contact angles, water penetrating speeds are more or less the same at this pore size range, indicating that wetting process in detergent powder dissolution plays a minor role comparing to other processes.

Considering in the previous *DigiDiss* simulation of pore structure where results show that solid particles dissolve inside pores and saturate the solution instantly, the real importance of the pore structure on particle for dissolution is arguable. However,

whether after water penetrating inside pores and casing disintegration which can affect dissolution significantly, needs further investigation.

4.6 Conclusions

In this chapter, several parameters, particle shape, surface area to volume ratio, pore structure, agitation and pore filling have been investigated by either simulation or both simulation and experiment.

For particle structure related parameters, surface area to volume ratio plays a more important role than particle shape and pore structure. The higher the S/V ratio, the faster particle dissolves.

The experiment and simulation results show that agitation influence particle dissolution significantly mainly due to the shear rate around particle. The higher the shear rate, the faster particle dissolves.

A very detail investigation of wetting process has been done by experiment. Liquid surface tension, pore size, wettability are important when pore size is in millimeter scale. Further simulation of micro-sized pore filling was carried out based on the results from experiment. To the opposite of millimeter sized pores, wetting process in micro-sized range shows less importance by comparing the total pore filling time to detergent powder dissolution time.

CHAPTER 5
DERIVATION OF DISSOLUTION EQUATION

Particle dissolution has been found to be a critical part on detergent performance in washing systems. It is essential to develop a model first to be able to characterize particles in the bench scale, and then extrapolate dissolution performance across any washing system. Such a model can help industry to understand how to better design the particles for improved performance. Previous particle dissolution models use average particle diameters and do not include the effect of agitation in the calculation of the mass transfer coefficient. In this chapter, a new modelling framework combining dissolution equation derived from Noyes-Whitney equation and COMSOL CFD simulation has been developed. Simple particle dissolution profiles are predicted from the framework.

5.1 Derivation of dissolution equation

As reviewed in Chapter 2, when external mass transfer limitation at the particle surface boundary layer controls the particle dissolution rate, it can be modeled by Noyes-Whitney equation:

$$\frac{dM}{dt} = -K \cdot A \cdot (C_s - C) \qquad 5\text{-}1$$

Where K (m/s) is the mass transfer coefficient, M is the remaining mass of particles and C_s is the solubility of the material (saturated concentration). In most detergent powder washing system, $C \ll C_s$.

In convective dissolution condition, the dimensionless number Sherwood number (Sh) is introduced to represent the ratio of convective to diffusive mass transport:

$$\mathrm{Sh} = \frac{K \cdot L}{D} \qquad 2\text{-}11$$

The mass transfer coefficient for a spherical particle can be written as:

$$K = \frac{\mathrm{Sh} \cdot D}{d_p} \qquad 5\text{-}2$$

Where d_p is particle diameter.

Assuming particles are homogeneous, then particle density ρ_p is constant. For particles with a number of $N_{particle}$, the total initial mass of particles M_0 is:

$$M_0 = N_{particle} \cdot \rho_p \cdot \frac{1}{6} \cdot \pi \cdot {d_{p,0}}^3 \qquad 5\text{-}3$$

where $d_{p,0}$ is initial particle diameter. So the particle number $N_{particle}$ can be expressed as:

$$N_{particle} = \frac{6 \cdot M_0}{\rho_p \cdot \pi \cdot {d_{p,0}}^3} \qquad 5\text{-}4$$

So M can be expressed as:

$$M = N_{particle} \cdot \rho_p \cdot \frac{1}{6} \pi \cdot d_p^3 = \left(\frac{6 \cdot M_0}{\pi \cdot \rho_p \cdot d_{p,0}^3} \right) \cdot \rho_p \cdot \frac{1}{6} \cdot \pi \cdot d_p^3 = M_0 \cdot \left(\frac{d_p}{d_{p,0}} \right)^3 \qquad 5\text{-}5$$

Hence $d_p = d_{p,0} \cdot \left(\frac{M}{M_0} \right)^{1/3}$ 5-6

Similarly the total surface area of the particles can be given by

$$A = N_{particle} \cdot \pi \cdot d_p^2 = N_{particle} \cdot \pi \cdot d_{p,0}^2 \left(\frac{M}{M_0} \right)^{2/3} = A_0 \cdot \left(\frac{M}{M_0} \right)^{2/3} \qquad 5\text{-}7$$

where A_0 is initial surface area of particle.

Substituting Equation 5-1 with Equation 5-2 and 5-7, and assuming $C \approx C_s$, Sherwood number can be introduced to Noyes-Whitney equation which gives:

$$\frac{dM}{dt} = -\frac{\mathrm{Sh} \cdot D}{d_p} \cdot A \cdot C_s = -\frac{\mathrm{Sh} \cdot D}{d_{p,0}} \cdot A_0 \cdot C_s \cdot \left(\frac{M}{M_0} \right)^{1/3} \quad 5\text{-}8$$

Assuming the Sherwood number is constant, by integrating Equation 5-8, mass transfer of spherical particles can be expressed as:

$$M^{2/3} = M_0^{2/3} - \frac{2}{3} \frac{\mathrm{Sh} \cdot D}{d_{p,0}} \cdot \frac{A_0 \cdot C_s}{M_0^{1/3}} \cdot t \quad 5\text{-}9$$

There are many different expressions that have been developed to calculate the Sherwood number for a spherical particle that work well under different assumptions. When particles are well mixed inside a stirring tank, as reviewed in Chapter 2, the following expression can be used

$$\mathrm{Sh} = 2 + 0.47 \cdot \left(\frac{\rho_f \cdot \varepsilon^{1/3} \cdot d_p^{4/3}}{\mu_f}\right)^{0.62} \cdot \left(\frac{\mu_f}{\rho_f \cdot D}\right)^{0.36} \cdot \left(\frac{d_{impeller}}{d_{tank}}\right)^{0.17} \quad 2\text{-}12$$

Equation 2-12 includes particle size information and also particle size changes as particle dissolves. It is important to note that Equation 2-12 is valid when using local conditions for turbulent power dissipation rate ε. Under turbulent flow conditions (above all in baffled tanks), a good first approximation is to assume that all the input power dissipates into turbulent energy dissipation rate thus the average turbulent dissipation rate can be estimated by

$$\varepsilon = \frac{P}{V_f \cdot \rho_f} \quad 5\text{-}10$$

which is Equation (2) in Figure 3.1. P is the input power, and V_f is the volume of the fluid and ρ_f is fluid density.

This theory basically indicates that power/mass is the key variable when scaling dissolution mass transfer coefficients across scales. If the particles are not well mixed, local turbulent dissipation rates need to be used.

5.2 Parameters calculation

In summary, the parameters in Equation 2-12, 5-9 and 5-10 can be divided into three categories, the particle related properties, solution related properties and dissolution system geometry.

Particle related properties

In order to apply the framework in particle dissolution, parameters about initial particle size $d_{p,0}$, solubility C_s, diffusivity D, and initial mass M_0 have to be pre-known.

Initial particle size and mass can be measured by experiment methods. For particles with a certain size distribution, gravity dispersion for image analysis can be used to measure PSD see Section 3.2.2 in Chapter 3.

Solubility of particles in water can be either found in literature or measured by experiment method, see Section 3.2.2.

Diffusivity, also called diffusion coefficient, can be calculated by Equation 2-8, 2-10 and Table 2.1.

Solution related properties

Liquid properties for example density ρ_f, viscosity μ_f and volume V_f can be measured by experiment methods. Density meter is for density, rheometer is for viscosity, details see Section 3.2.2.

Dissolution system geometry

Same particles in different dissolution systems can end up with different dissolution behaviour. Small scales for example in the lab, dissolution system could be a magnetic stir in a beaker (see experiment in Section 4.4.1). Large scales for example domestic application, dissolution system could be a washing machine. The power putting into dissolution system P, the geometrical properties such as dissolution tank diameter d_{tank}, impeller diameter $d_{impeller}$, these parameters determine dissolution system is laminar or turbulent, particle is well mixed or aggregate in a local area.

For the case when impeller power number N_P can be found from the industrial mixing handbook, then the power on the impeller in a stirring tank can be calculated by Equation 3-7. Then the energy dissipation rate ε can be calculated by Equation 5-10. For a dissolution system where impeller power number is not known, simulation method based on COMSOL Multiphysics CFD module can be used to obtain this information.

5.3 Prediction of single size particle dissolution

Simple prediction cases will be present in this section. In detergent powder, Sodium carbonate and sodium sulphate are two most common ingredients. Solubility of these two salts in water at different temperature can be found in literature **[127]**, shown in Figure 5.1 and 5.2. Diffusivity of these two salts in water are calculated from Equation 2-8, 2-10 and Table 2.1, shown in Table 5.1 and 5.2.

Table 5. 1 Water viscosity, Na_2CO_3 diffusivity and solubility data.

Temperature (dC)	μ_f (10^{-3} Pa·s)	D (10^{-9} m^2/s)	C_s (kg/m^3) [127]
20	1.002	1.12	218.0
25	0.894	1.28	307.2
40	0.653	1.84	488.1
60	0.466	2.74	464.1

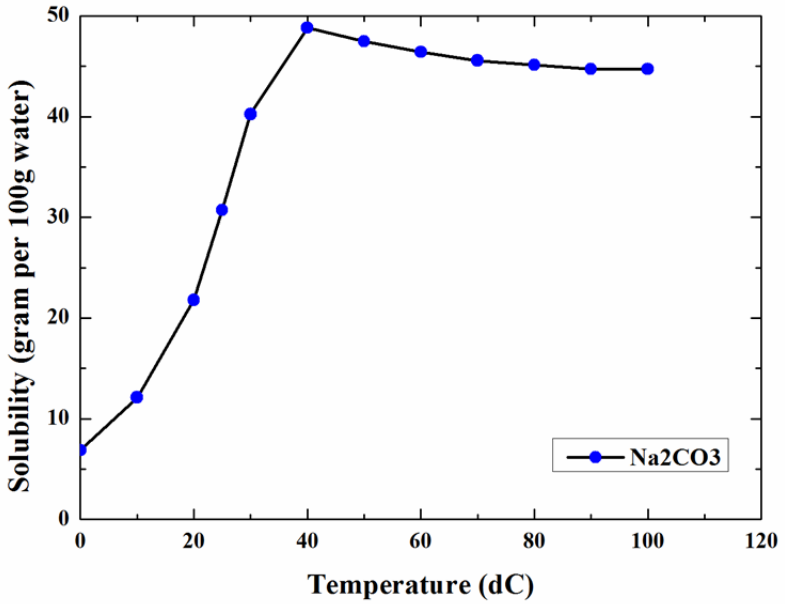

Figure 5. 1 Solubility of sodium carbonate in gram per 100 g H_2O vs temperature (dC) [127].

Table 5. 2 Na_2SO_4 diffusivity and solubility.

Temperature (dC)	D (10^{-9} m^2/s)	C_s (kg/m^3) [127]
20	1.08	192.3
25	1.23	281.1
40	1.77	478.2
60	2.64	447.2

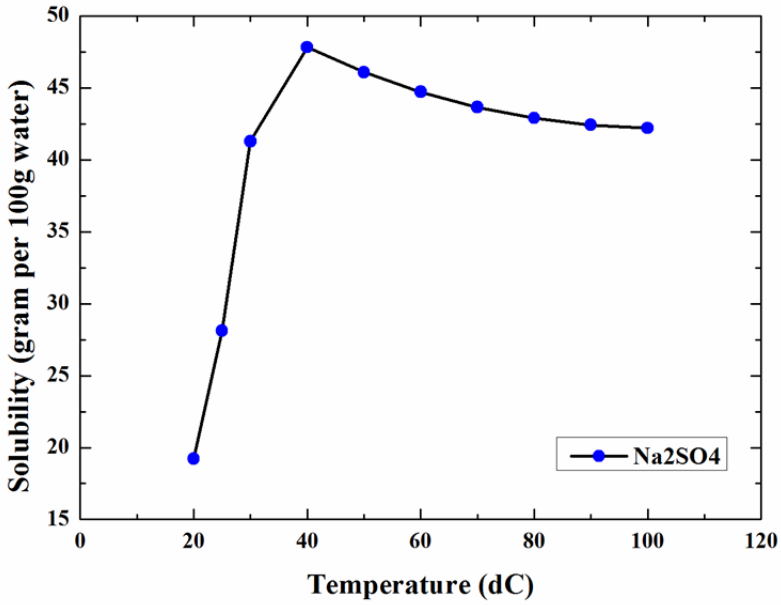

Figure 5. 2 Solubility of sodium sulphate in gram per 100 g H_2O vs temperature (dC) [127].

Assuming in a dissolution system, an impeller of Marine propeller is used with a tip-to-tip diameter as 70 mm. The power number is 0.35 [128]. The dissolution tank has a shape as Figure 2.10 with 103 mm tank diameter.

The power input in such a dissolution system can be calculated by [128]

$$P = N_P \rho_f N^3 d_{impeller}{}^5 \qquad 5\text{-}11$$

For rotating speed of 100 rpm, 200 rpm and 300 rpm, calculating result are shown in Table 5.3 with 0.8 L water in the tank.

Table 5. 3 Calculation of Reynolds number, power input and energy dissipation rate.

Temperature (dC)	N (rpm)	Re (10^4)	P (W)	ε (W/kg)
20	100	0.817	0.556	0.695
	200	1.633	4.446	5.558
	300	2.450	15.006	18.758
40	100	1.241	0.551	0.695
	200	2.481	4.412	5.558
	300	3.722	14.889	18.758
60	100	1.724	0.546	0.695
	200	3.448	4.372	5.558
	300	5.171	14.754	18.758

With initial mass of 0.15 g, particle size of 1 mm, the dissolution profiles of Na_2CO_3 and Na_2SO_4 in this stirring system can be predicted by Equation 2-12 and 5-9. Results are shown in Figure 5.3 and 5.4.

Figure 5.3 (a) is Na_2CO_3 release profiles at 100 rpm, 200 rpm and 300 rpm when temperature is 20 dC. (b) is Na_2CO_3 release profiles at 20 dC, 40 dC and 60 dC when rpm is fixed as 100. Same sequence of Na_2SO_4 release profiles show in Figure 5.4 (a) and (b).

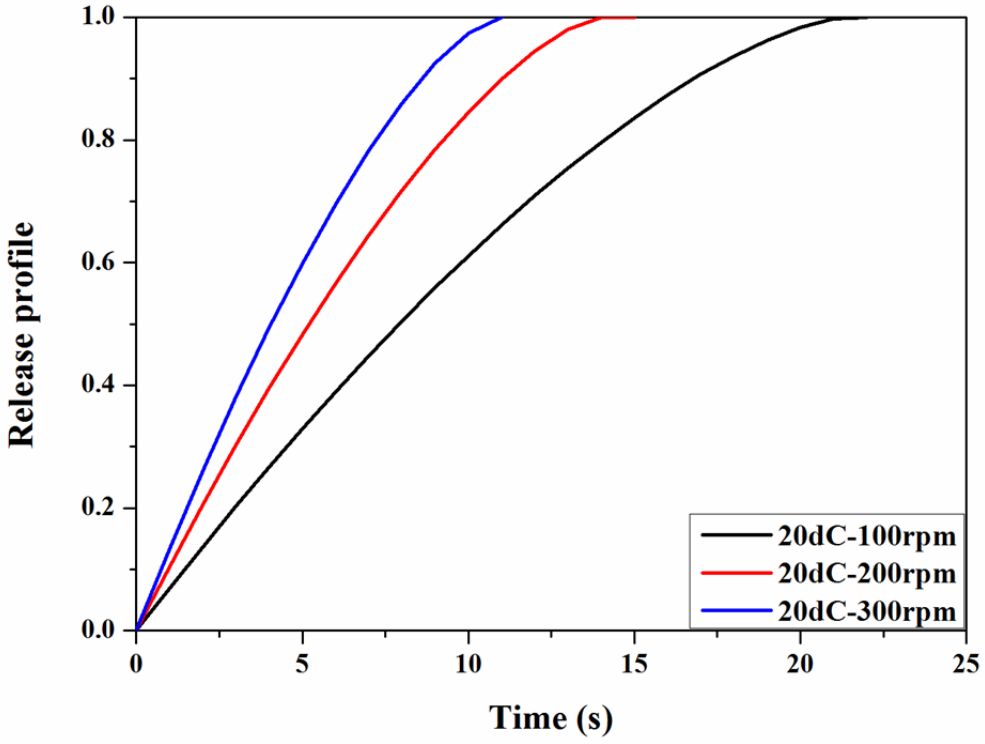

(a)

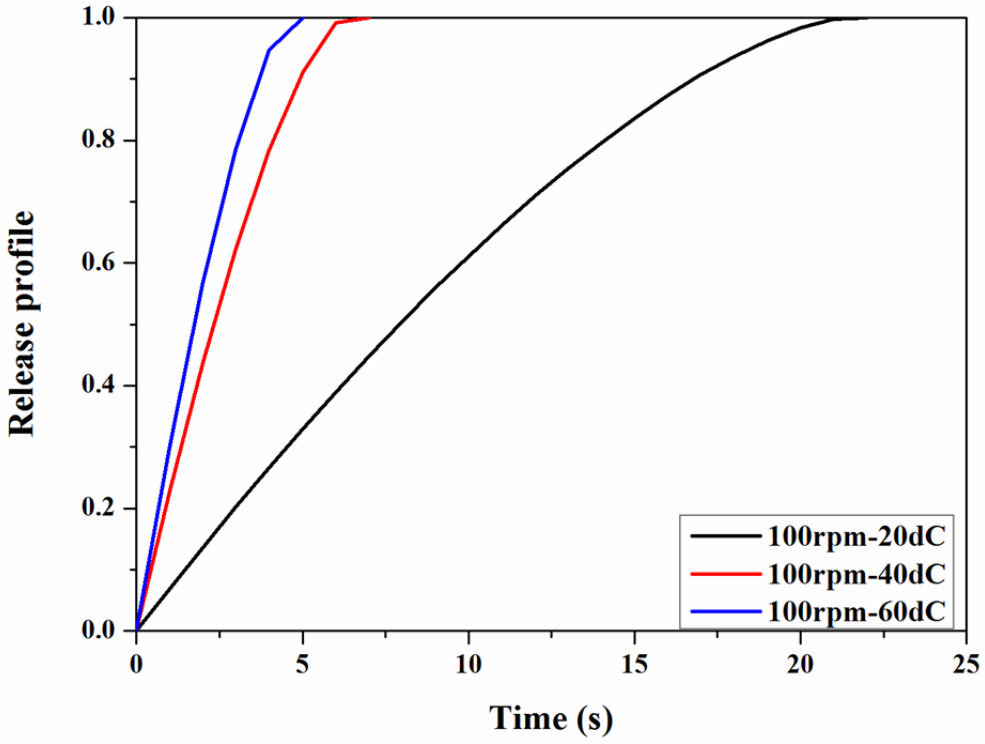

(b)

Figure 5. 3 Model prediction of Na_2CO_3 release profiles at (a) different rpm and (b) different temperature.

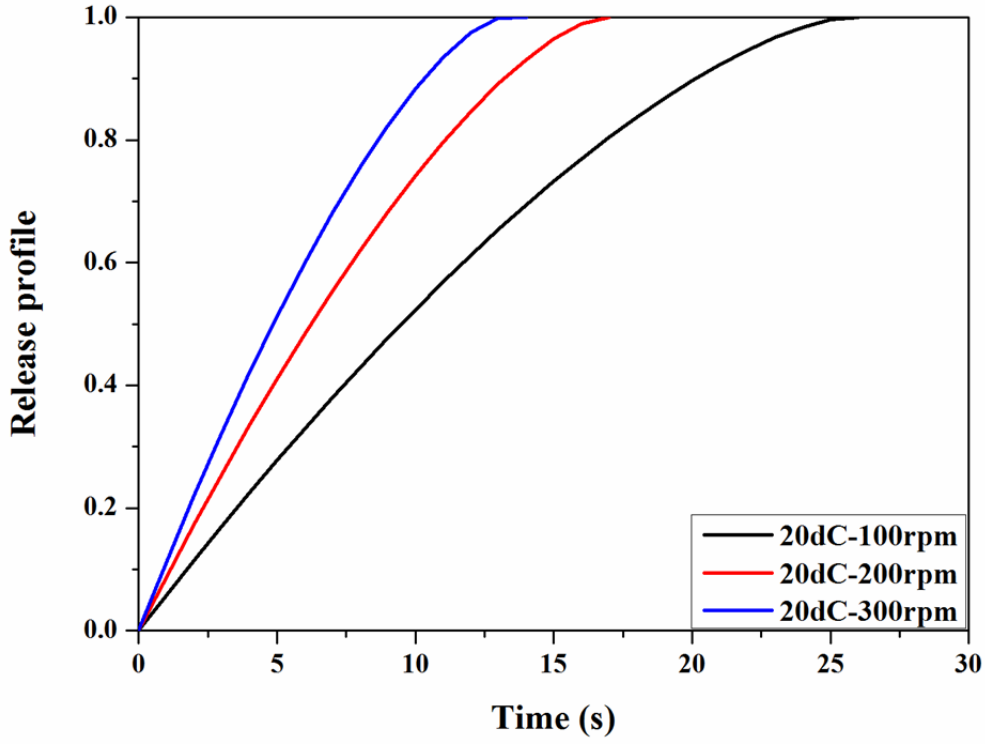

(a)

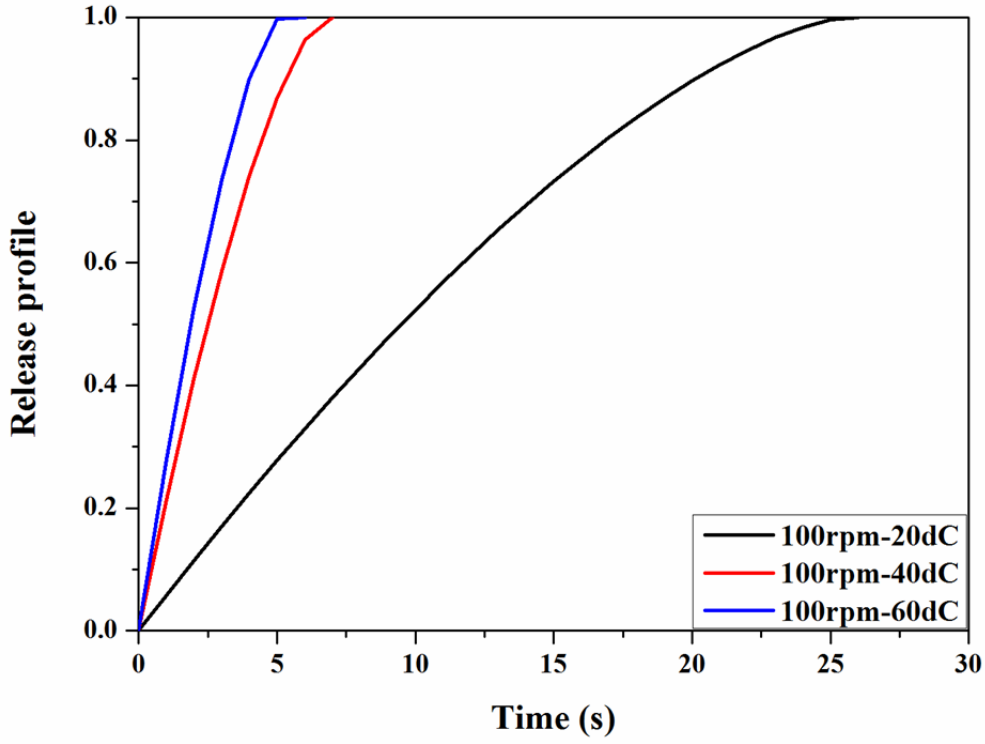

(b)

Figure 5. 4 Model prediction of Na_2SO_4 release profiles at (a) different rpm and (b) different temperature.

Under convective condition, Figure 5.3 and 5.4 show clearly that the mass transfer rate of Na_2CO_3 and Na_2SO_4 in water increase with increasing rotating speed and temperature. Higher rotating speed results in higher energy dissipation rate, hence higher Sherwood number, and eventually faster mass transfer rate. Temperature has a unique effect on mass transfer rate. From 20 dC to 40 dC, the total dissolution time of 0.15 g Na_2CO_3 and Na_2SO_4 decreases 15 s and 19 s respectively. From 40 dC to 60 dC, neither of these two salts show significant differences. This is probably solubilities of these two salts in water are nearly doubled from 20 dC to 40 dC but decrease 4.9% and 6.5% from 40 dC to 60 dC respectively. Temperature has a higher impact on mass transfer rate comparing to rotating speed.

5.4 Prediction of particle dissolving with certain size distribution

In previous section, the dissolution of single sized particle in standard mixing system was predicted by the derived equations. In this section, particle with certain size distribution dissolving in a non standard mixing system is predicted by both the derived equations and COMSOL Multiphysics CFD module.

5.4.1 PSD of Na2CO3 granule

PSD of Na_2CO_3 granule was measured by gravity dispersion for image analysis. Results are shown in Figure 5.5. From Figure 5.5, most of the particle size are between 200 μm and 1.2 mm, mainly distributes between 500 μm to 600 μm.

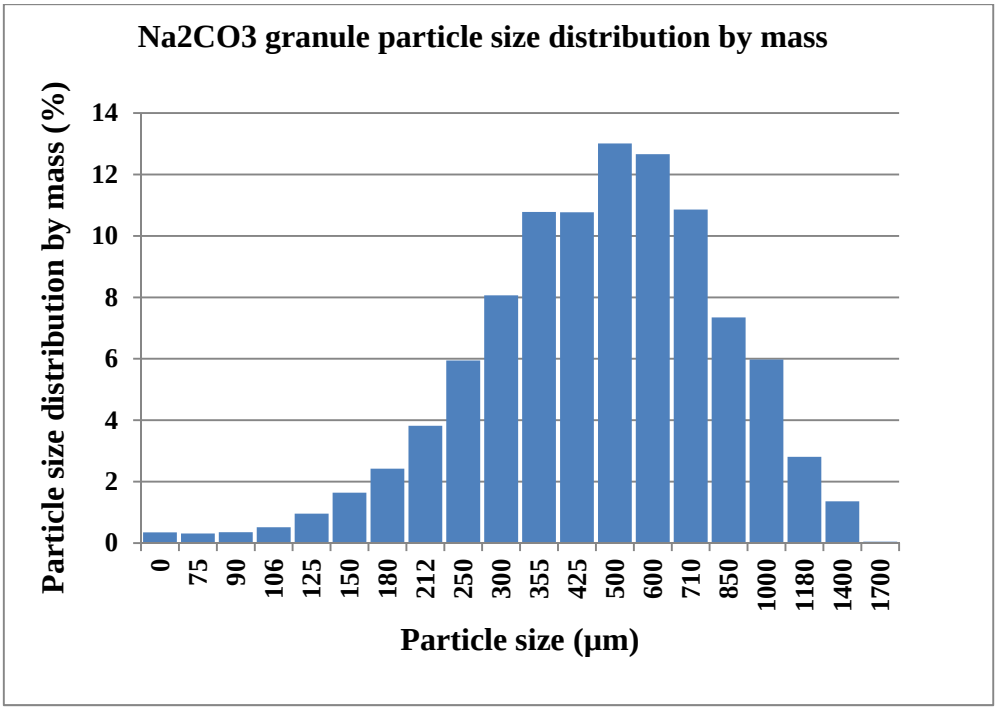

Figure 5. 5 Particle size distribution of Na2CO3 granule.

5.4.2 COMSOL simulation of mixing system power number

The dissolution system in this case study is PTWS 610 testing apparatus shown in Figure 2.8 with a rotating impeller in Figure 2.9 (b). For this impeller, power number information can not be found in mixing handbook. Therefore, COMSOL Multiphysics rotating machinary module is used to calculate its power number. Geometry is shown in Figure 3.11. Impeller diamention is shown in Figure 5.6.

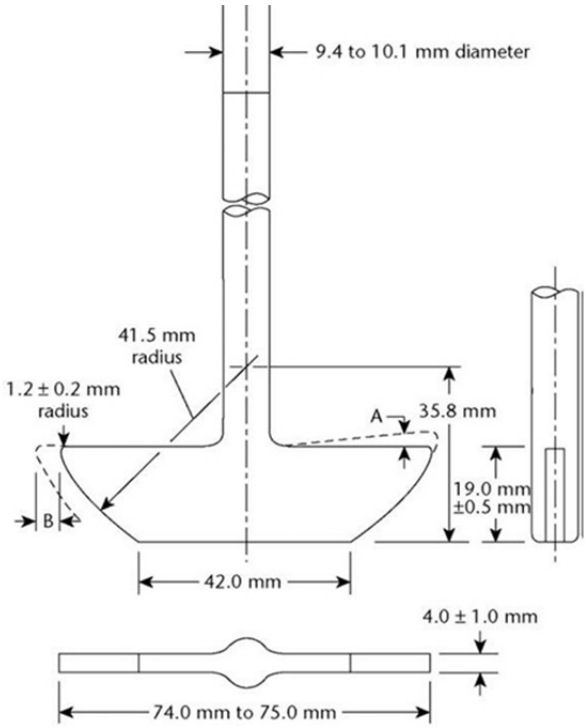

Figure 5. 6 Dimension of rotating impeller[129].

Following the method introduced in section 3.2.2, the power integrated on impeller surface at 20 rpm 20 dC is shown in Figure 5.7. After rotating 20 s, power on impeller stops changing, mixing system achieves equilibrium state.

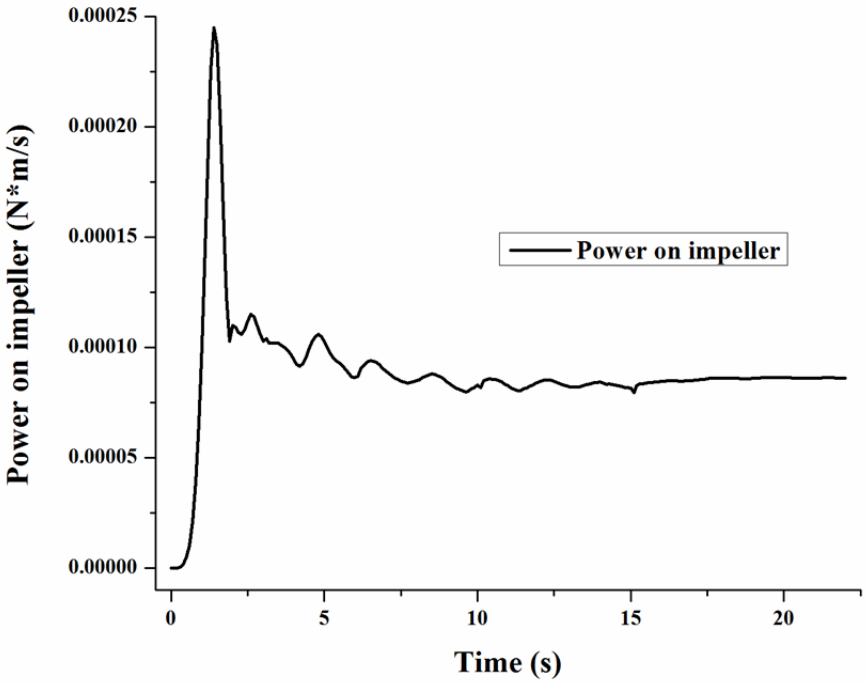

Figure 5. 7 Power on impeller changes as a function of rotating time.

Simulation of different rpm and temperature is carried out to calculated the power number of dissolution system. Simulation conditions are listed in Table 5.4.

Table 5. 4 COMSOL simulation conditions.

Temperature (dC)	N (rpm)	ρ_f (kg/m^3)	Re (10^4)
20	20	998	0.187
	50		0.468
	80		0.749
	200		1.871
40	20	992	0.285
	50		0.712
	80		1.139
	200		2.848
60	20	983	0.396
	50		0.889
	80		1.582
	200		3.955

Equation 5-11 is used to fit power number N_P of the impeller. Results are shown in Figure 5.8.

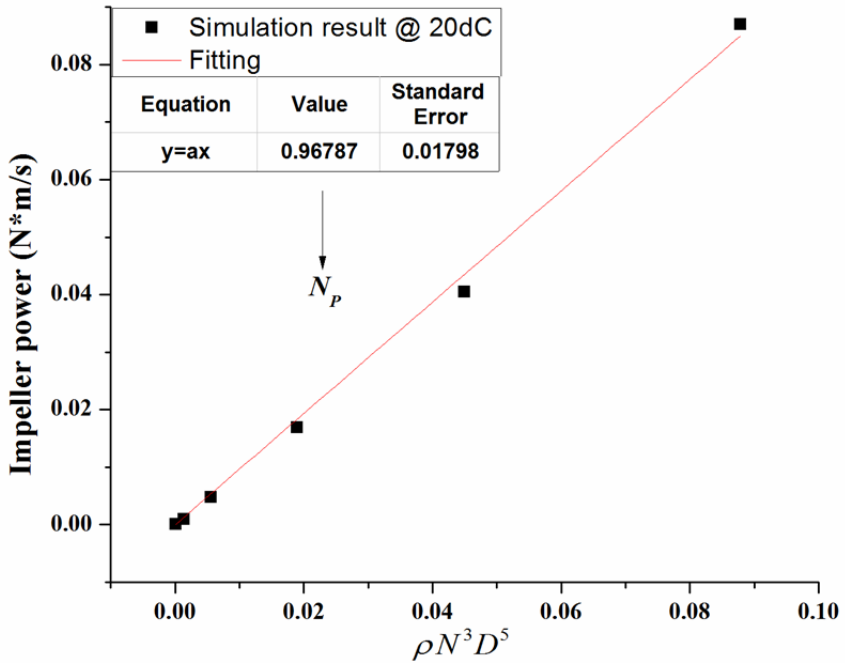

(a)

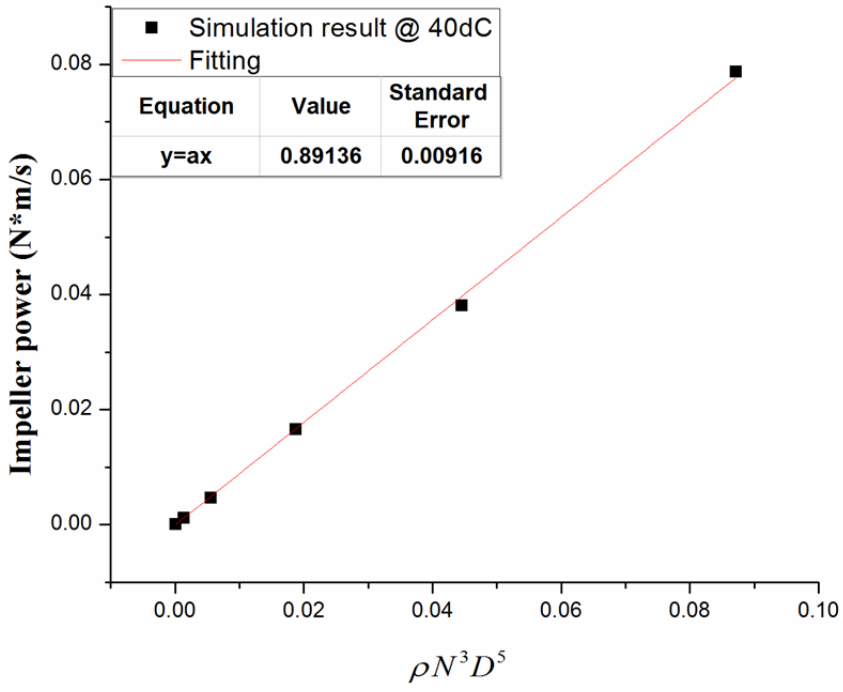

(b)

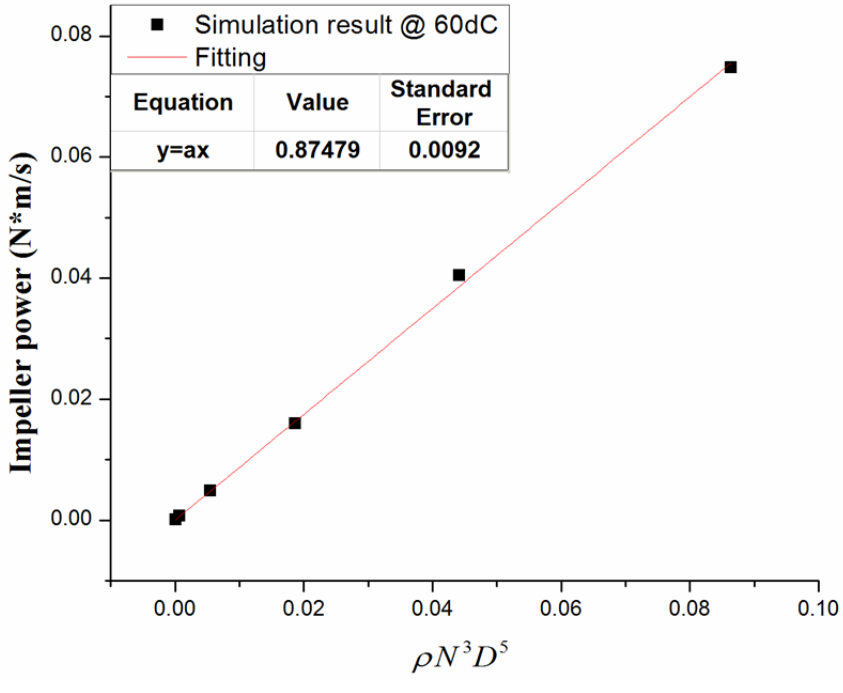

(c)

Figure 5. 8 Power number fitting results (a) 20 dC, (b) 40 dC and (c) 60 dC.

At different temperature, fitting results are slightly different. Figure 5.9 is power number vs Reynolds number. In the regime where Reynolds number is smaller than 5000, power number varies noticeably. As Reynolds number increases (>5000), turbulent flow developes more, the power number becomes constant and

independent of Re with an average power number of N_P ~ 0.882. This power number is between marin propeller (N_P 0.35) and paddle (N_P 2) [128], see embedded picture in Figure 5.9. Turbulent energy dissipation rate is calculated based on the fitting result of impeller power number, shown in Table 5.5. It is clear that dissipation rate is dependent on rotating speed for a certain mixing system and independent on temperature.

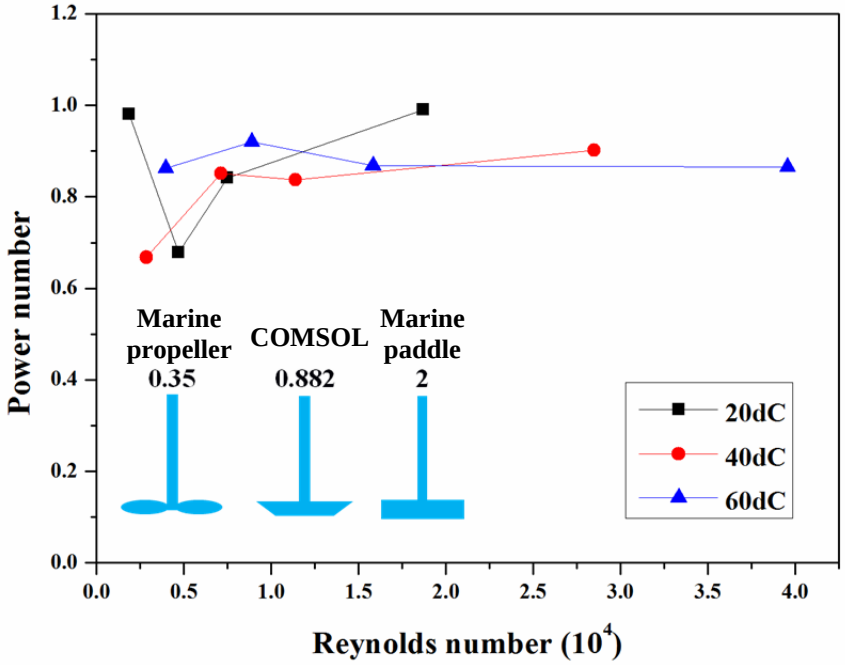

Figure 5. 9 Power number versus Reynolds number. Embedded pictures of marine propeller and paddle are from [128] with power number 0.35 and 2 respectively.

Table 5. 5 Turbulent energy dissipation rate in mixing tank with 800 mL water.

Temperature (dC)	N (rpm)	P (W)	ρ_f (kg/m^3)	ε (W/kg)
20	100	0.010	998	0.01211
	200	0.077		0.09690
	300	0.261		0.32704
40	100	0.010	992	0.01211
	200	0.077		0.09690
	300	0.260		0.32704
60	100	0.010	983	0.01211
	200	0.076		0.09690
	300	0.257		0.32704

5.4.3 Model prediction

0.15 g Na_2CO_3 granule with PSD as Figure 5.5 is inputed into Equation 2-12 and 5-9. Predicting results for particles dissolving in Figure 3.11 mixing system are shown in Figure 5.10 (a) at 20 dC different rpm and (b) 100 rpm different temperature.

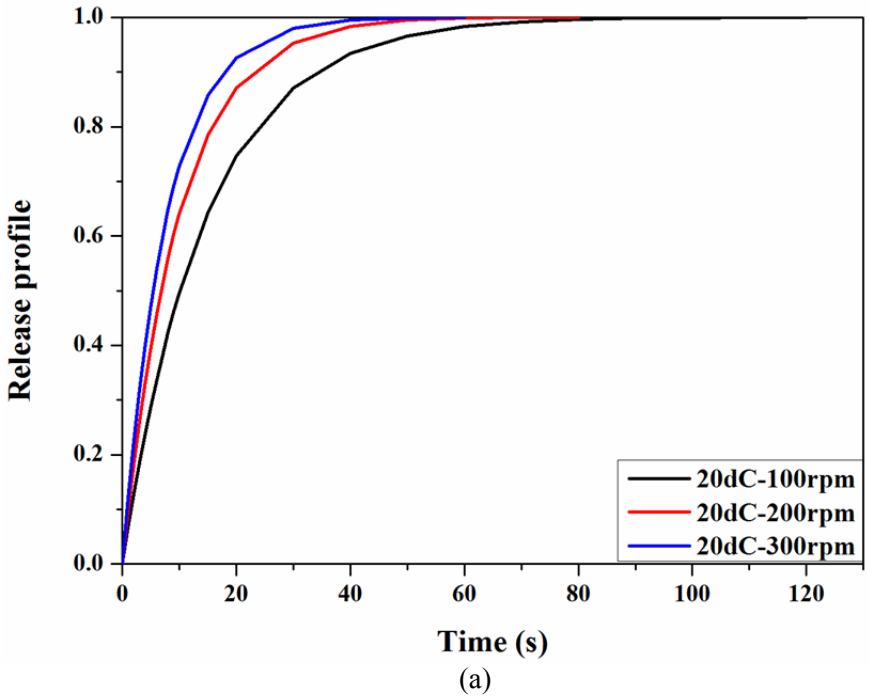

(a)

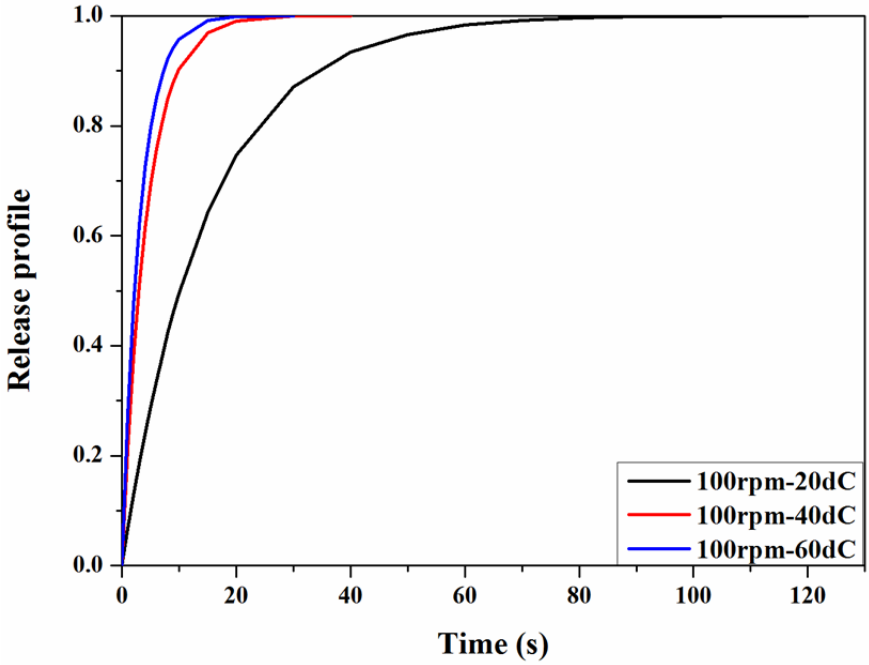

(b)

Figure 5. 10 Release profile of Na2CO3 granule dissolving in Figure 3.1 mixing tank with Figure 5.5 PSD.

Figure 5.10 shows similar particle dissolution profiles as single sized particle. Increasing rotating speed and temperature can increase particle mass transfer rate. Different from singe sized particle dissolution, higher mass transfer rate is predicted of this PSD particles, see Figure 5.11. The prediction of single sized particle uses particle size 1 mm. In multi sized particle prediction (with Figure 5.5 PSD), most of the particles are smaller than 1 mm. Only 10 wt % of the particles are ≥ 1mm. 90 wt% small particles contribute to the high mass transfer rate at the initial stage, and then slow down the dissolution process. The release profile of single sized particle is more linear. With the same weight 0.15 g, 1 mm particles uses shorter time to finish the dissolution.

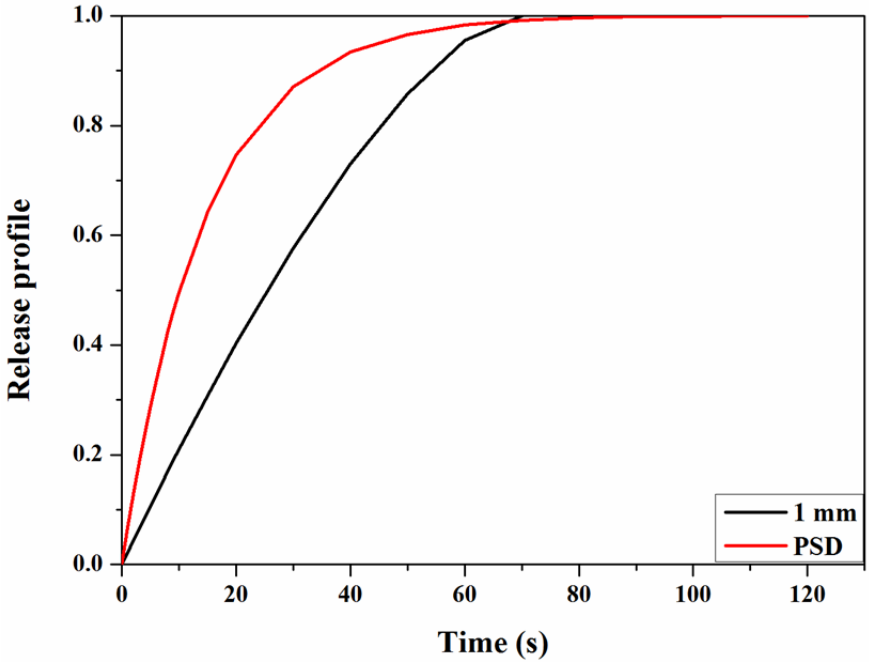

Figure 5. 11 Release profile of Na_2CO_3 granule dissolving in Figure 3.1 mixing tank, red line is Figure 5.5 PSD, and black line is 1 mm particle size.

5.4 Conclusions

Dissolution framework including mass transfer equation and CFD simulation has been developed to predict particle dissolving behavior at different rotating speed and temperature. Dissolution system with pre-known power number of the impeller and not-known power number of the impeller can be predicted by either equation or COMSOL simulation. Particle with certain size distribution can be predicted by the developed framework.

Simple case study of single sized Na_2CO_3 and Na_2SO_4 granule in marine impeller dissolution system was presented. Results show that with increasing rotating speed and temperature, mass transfer rate can be increased. Temperature has a bigger influence on dissolution behavior.

A more compllicated case study of multi sized Na_2CO_3 granule in PTWS 610 dissolution apparatus was presented. Predicting results show smaller particles faster

mass transfer rate at the initial stage while bigger particles slow down dissolution at the later stage.

CHAPTER 6
EXPERIMENT OF DISSOLUTION AND MODEL VALIDATION

In the previous chapter, a modelling framework combining mass transfer equations and COMSOL simulation has been developed and used to predict particle dissolving in different conditions. In this chapter, experiment of particles dissolving in water are carried out to validate the framework. More complicated cases while particles are not spherical, with multi ingredients and porous structures are investigated to validate the framework.

6.1 Na_2CO_3 dissolution experiment

A chemically homogeneous and non-porous granular sodium carbonate (batch number 1009260NM-019) provided by Proctor and Gamble is used to validate the model. 0.15 g Na_2CO_3 granule with PSD as Figure 5.5 were put into dissolution system PTWS 610 (Figure 2.8 and 2.9 (b)). The SEM images of these granules are shown in Figure 6.1.

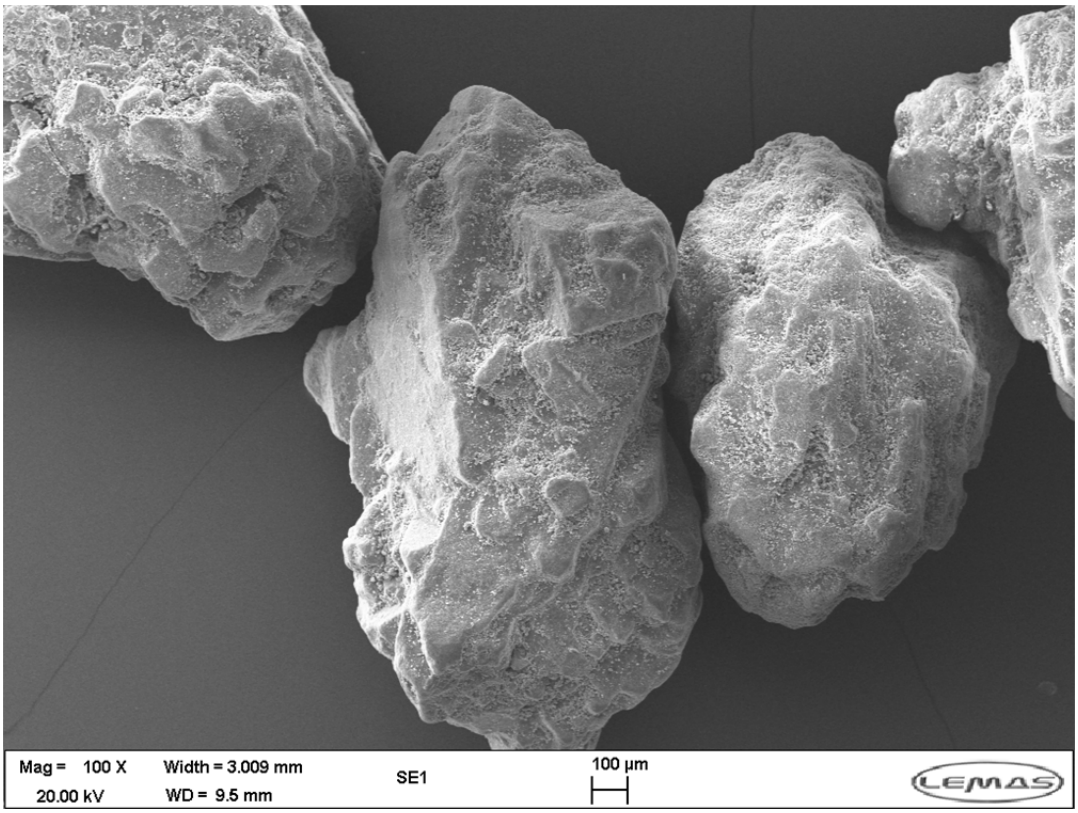

(a)

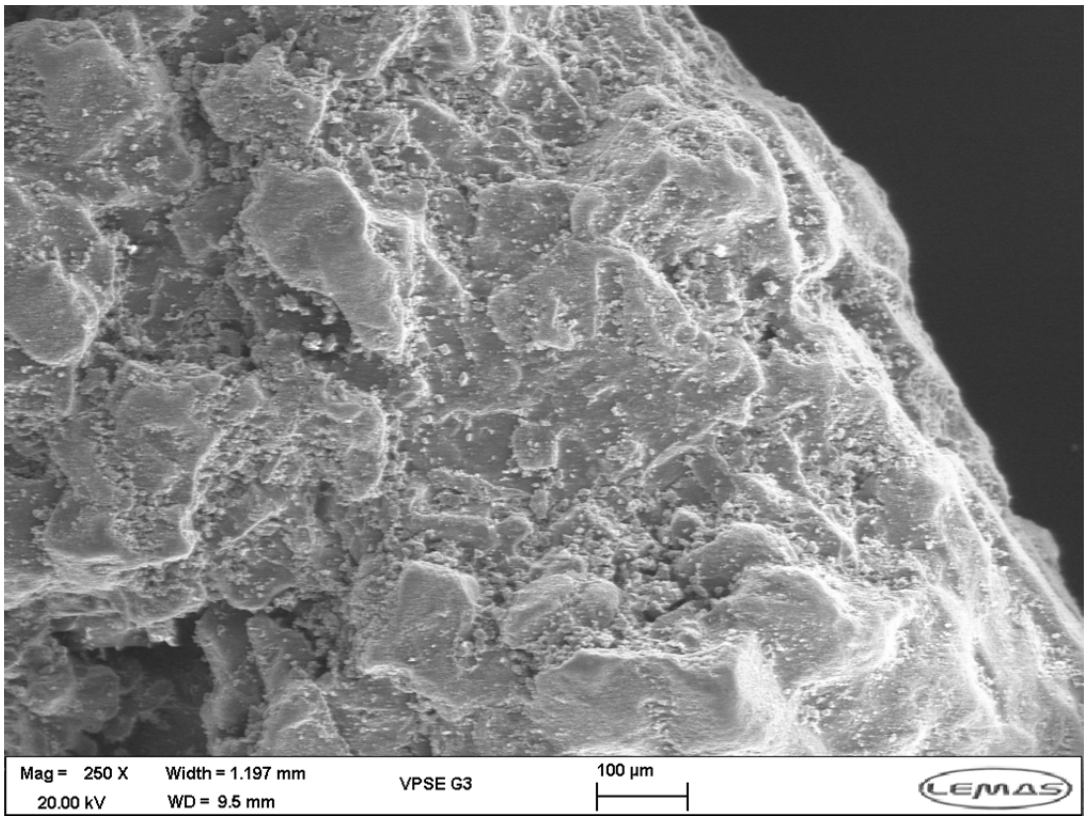

(b)

Figure 6. 1 SEM images of Na_2CO_3 granule.

6.1.1 Rotating speed

The main challenge with this particle is its density. Relatively high density (~2540 kg/m^3) of this particle makes it difficult to be well mixed inside the PTWS 610 system. The effect of rotating speed is first investigated in the framwork.

At 100 rpm, most of Na_2CO_3 granules are at the bottom of the vessel and have almost no motion at all (see Figure 6.2 (a), red circle indicates particle location). This leads to a lump formation that slows down the dissolution of the particle more than expected. Turbulent dissipation rate ε is probably smaller than average value. At 200 rpm and 300 rpm, amount of small sized Na_2CO_3 granules are circling around the shaft while big sized are in motion circling around the bottom of the vessel (see Figure 6.2 (b), red circle indicates big particle location). Therefore, it is

necessary to check local turbulent dissipation rate in COMSOL model. The same model in section 5.4.2 is used here.

(a)

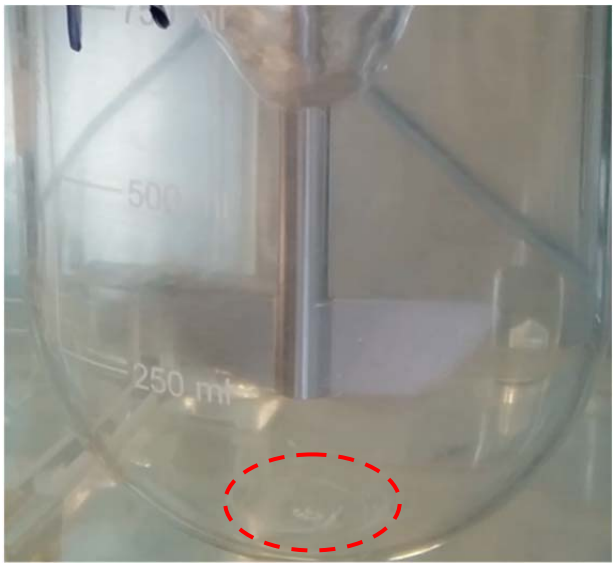

(b)

Figure 6. 2 Na_2CO_3 granule position in vessel under (a) 100 rpm and (b) 200, 300 rpm at 20dC. Red dash circles in the picture indicate where granules are.

Figure 6.3 shows turbulent dissipation rate inside PTWS 610 at 20 dC simulated by COMSOL. The average ε calculated in Table 5.5 for 100 rpm, 200 rpm and 300 rpm are 0.01211 W/kg, 0.09690 W/kg and 0.32704 W/kg respectively. The unit in Figure 6.3 m^2/s^3 equals W/kg. By comparing the average ε, it is clear in Figure 6.3

(a) 100 rpm that at the bottom of vessel, ε is around 0.004 m^2/s^3, which is smaller than the average value 0.01211 m^2/s^3. Same results can be found in Figure 6.3 (b) 200 rpm and (c) 300 rpm. However, because of higher rotating speed, more particles are circling around the shaft where ε is close to average value.

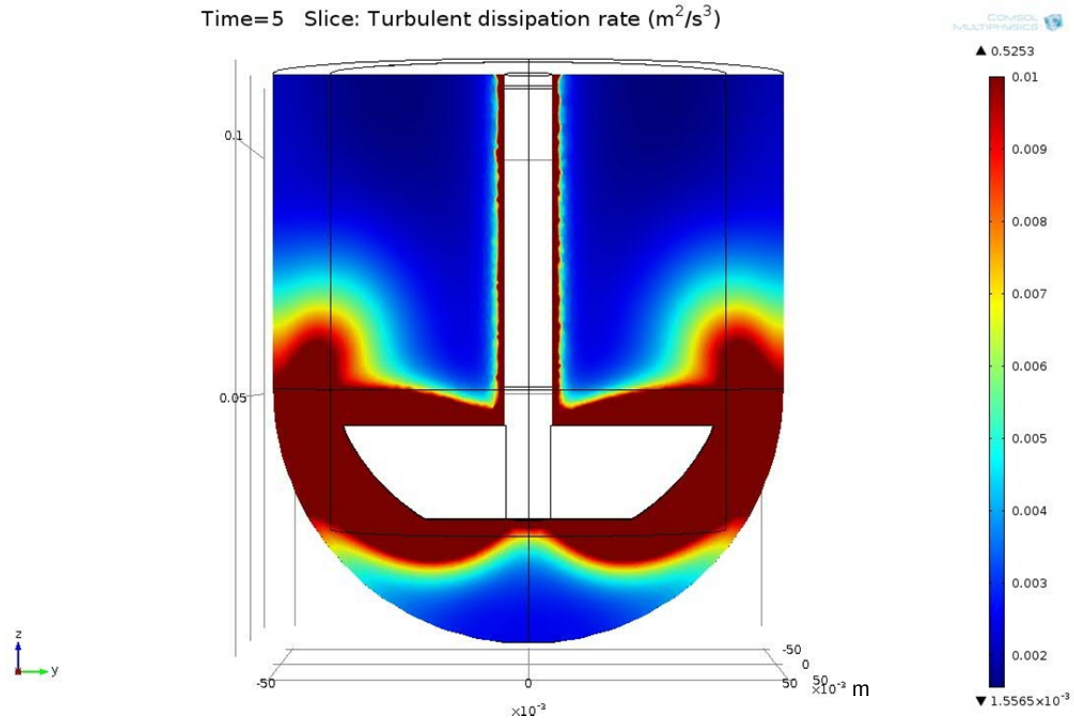

(a)

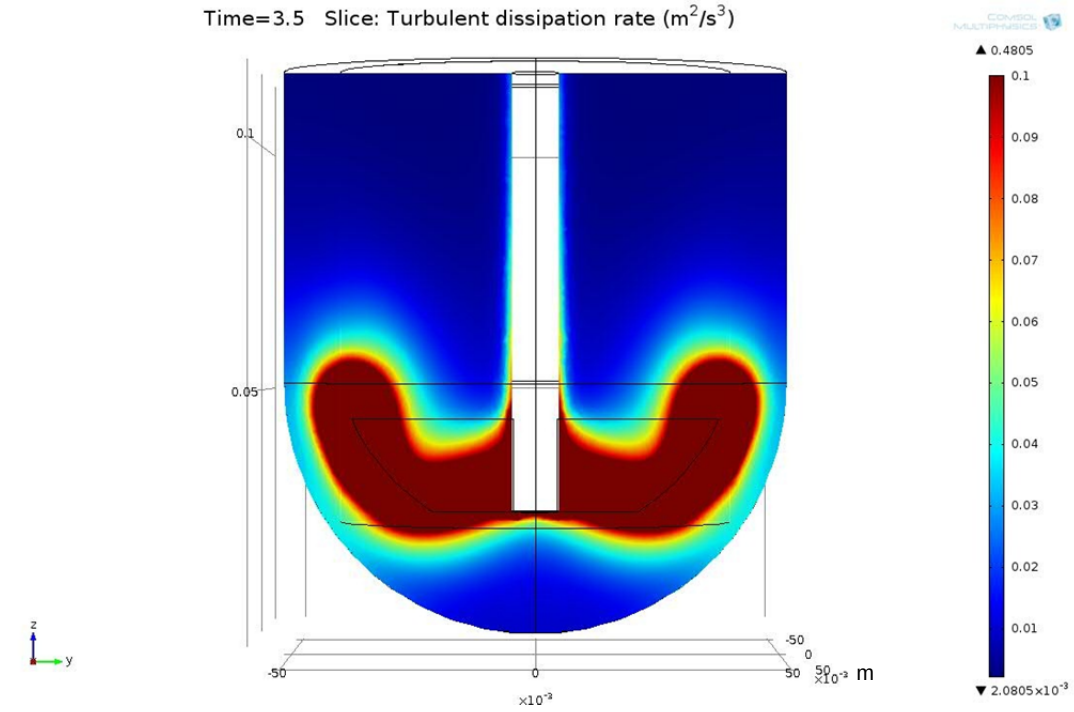

(b)

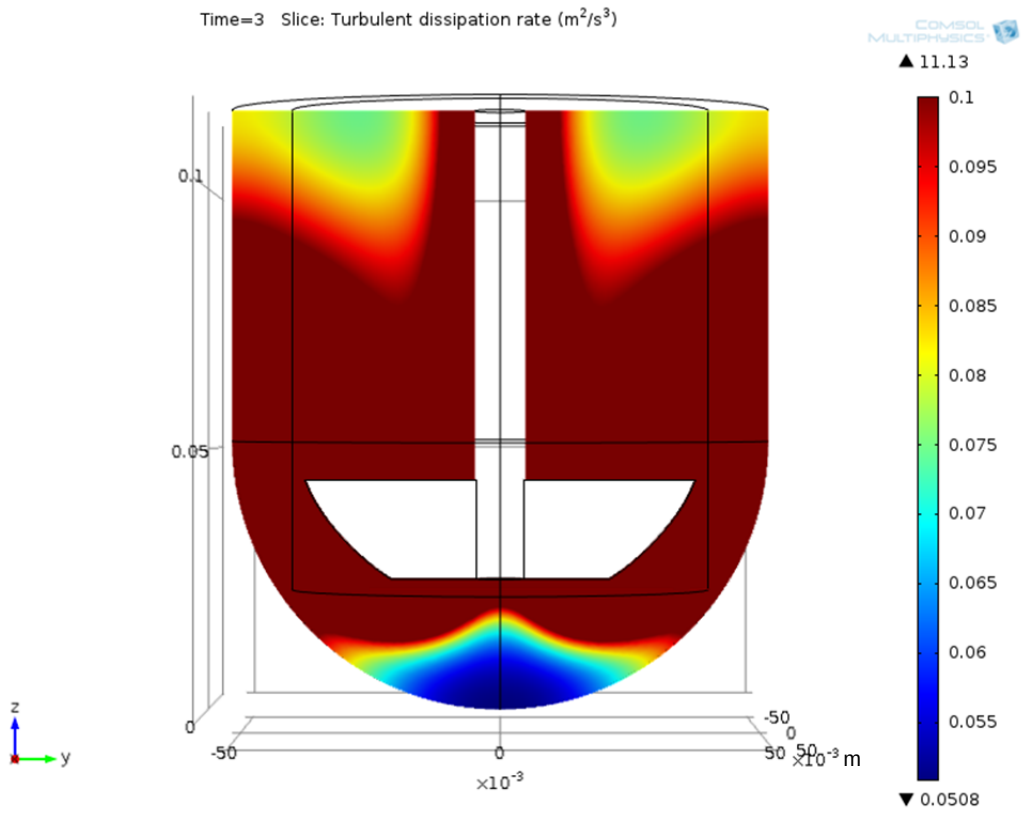

(c)

Figure 6. 3 Turbulent dissipation rate from COMSOL model at 20dC: (a) 100 rpm , (b) 200 rpm and (c) 300 rpm. Max scale ε = 0.01 m²/s³.

As a result, for 200 rpm and 300 rpm, model with average ε can be used to fit experiment data. Results are show in Figure 6.4 (a).

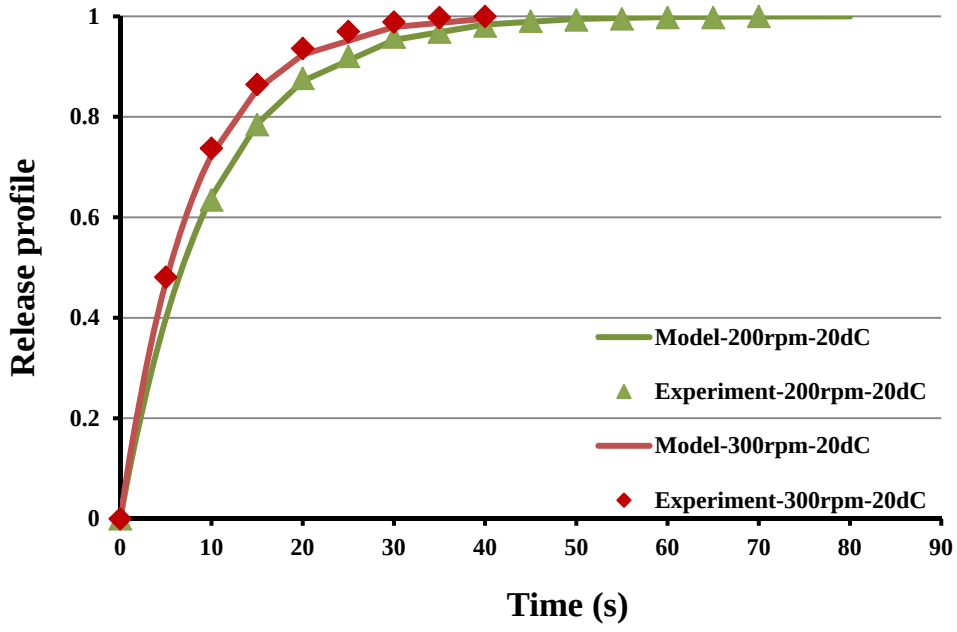

(a)

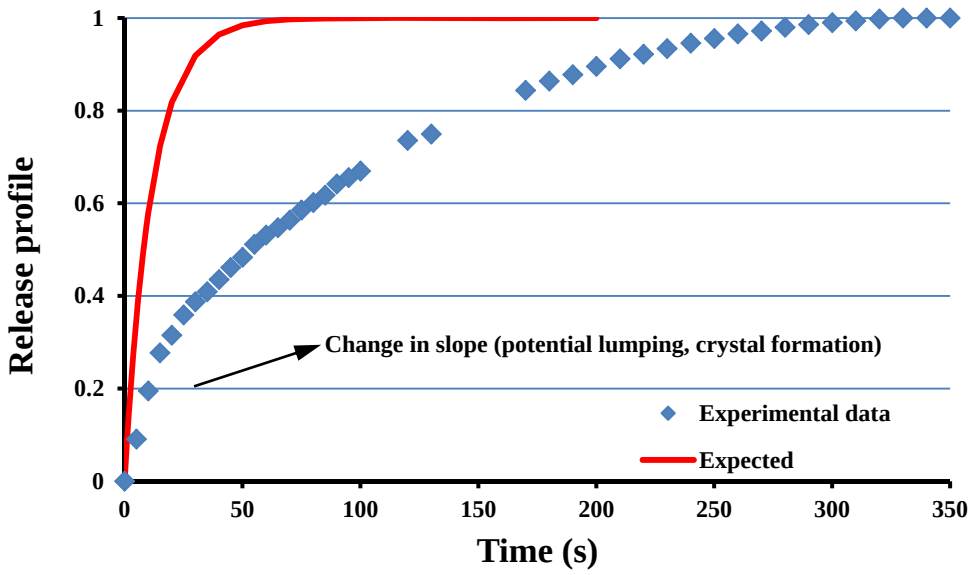

(b)

Figure 6. 4 Experimental vs. modelled particle dissolution data for Na_2CO_3 granule in a PTWS 610 mixing system for (a) 200 and 300 rpm and (b) 100 rpm at 20 dC.

A good fitting of Na_2CO_3 granule dissolving at 200 rpm and 300 rpm is shown in Figure 6.4 (a). These data experiment data and predicting data agree relatively well with an average turbulent energy dissipation rate.

For those cases where the particles are not well mixed with the flow, either floating at the water surface or sinking around the bottom of the impeller region (for example 100 rpm in the experiment), local values of the turbulent energy dissipation rate could be used with Equation 2-12 to predict dissolution rate.

The data for 100 rpm has been left out because in this case the granular sodium carbonate powder does not move at all because of high density and it lumps at the bottom of the vessel yielding a much lower dissolution rate than expected (see also the change of slope at time 20 s in Figure 6.4 (b)). In this cases where powder does not move at all and crystal formation and lumping takes place a different model for a powder bed may be needed to capture the reduction in surface area.

6.1.2 Temperature

As predicted in previous chapter, temperature has a higher effect on dissolution comparing to rotating speed. Figure 6.5 is release profiles of Na_2CO_3 granule at 20dC, 40dC and 60dC with 200 rpm and 300 rpm respectively.

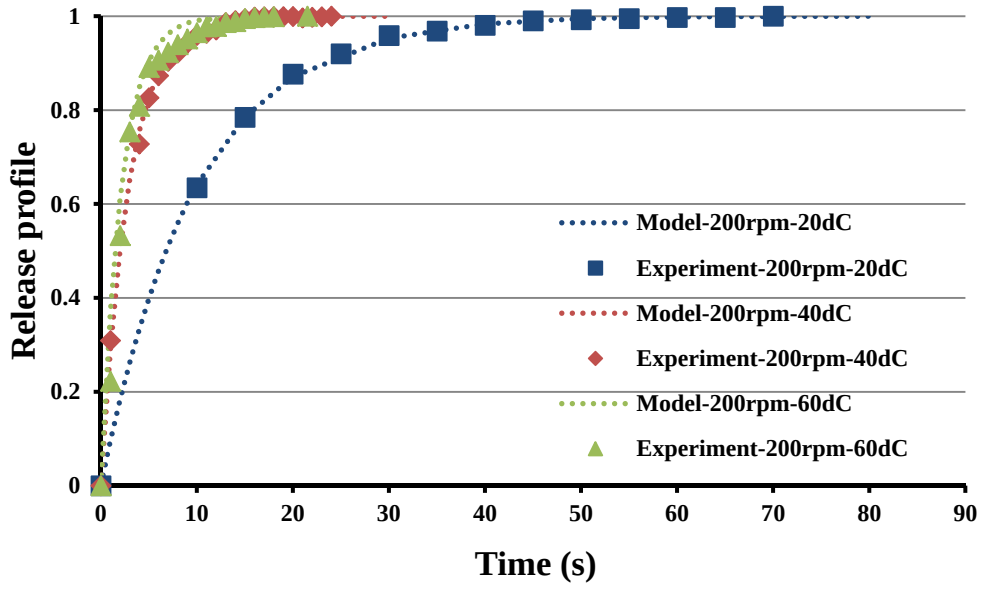

(a)

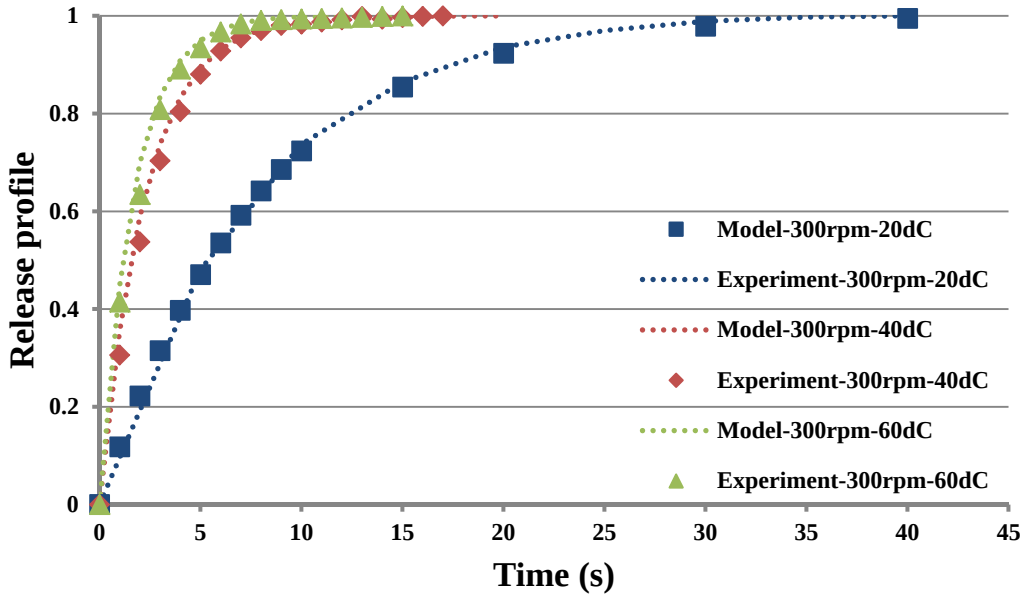

(b)

Figure 6. 5 Experimental vs. predicted particle dissolution data for Na_2CO_3 granule in a PTWS 610 mixing system for (a) 200 rpm and (b) 300 rpm at 20 dC, 40 dC and 60 dC respectively.

The average energy dissipation rate is used in the framework to predict Na_2CO_3 granule release profile, showing as dash line in Figure 6.5. A relatively good agreement is acheived between experiment data and modelling data, specially at 20 dC for both 200 rpm and 300 rpm. Slight differences appear when temperature increases to 40 dC and 60 dC. In some cases, the total dissolution time from experiment is shorter than predicted from the framework. This is probably because either the model is not abosutely accurate or experiment is not precise enough. However, results indicate that the developed framework can be used to predict single ingredients non porous particle dissolving in a well mixed system, either with pre-known PSD or single particle size.

6.2 Porous particle dissolution experiment

Based on the successful data correlation between experiment and model prediction for non-porous sodium carbonate, more complicated particle for example multi ingredients porous particle, hypothesis on whether external mass transfer is limited by the chemical dissolution process at the boundary or internal mass transfer occurs. The understanding of the role of porosity and internal surface area on controlling dissolution mechanism remains uncertian:

(1) If particle disintegration is present, internal area may become external area by breaking the large particle into smaller ones. Without disintegration, over time, internal pores will still become external when the granule shrinks as a result of dissolution.

(2) If solubility is very high, particle may fully dissolve in the water inside the particle when internal diffusion is faster than external mass transfer. If partially dissolved, this could also help to weaken granule and lead to particle breakage.

(3) If the chemical dissolution at the interface is the controlling step, internal area would speed up the process.

(4) If external mass transfer dominates, internal surface area does not play a substantial role although porosity still plays a role by increasing external surface area and thus dissolution rate. Internal mass transfer will not limit dissolution in any case, because even if it is very slow, particle will still dissolve through the external surface area (although dissolution could be slightly slower due to low concentration at the open area on the particle surface).

6.2.1 Porosity factor

For a porous particle, the intra porosity can be defined as:

$$\varphi = \frac{V_{pore}}{V_{particle}} = 1 - \frac{\rho_{particle,envelope}}{\rho_{particle,absolute}} \qquad 6\text{-}1$$

in which V_{pore} is pore volume, $V_{particle}$ is particle bulk volume, $\rho_{particle,envelope}$ is particle evelope density and $\rho_{particle,absolute}$ is particle true density.

The dissolved material inside the pores fills the pores. Assuming this could happen instantly and eventually all the particle becomes a pore, then the maximium internal concentration $C_{Max,Int}$ can be written as:

$$C_{Max,Int} = \frac{\rho_{particle,absolute} \cdot V_{particle} \cdot (1-\varphi)}{V_{particle}} = \rho_{particle,absolute} \cdot (1-\varphi) \qquad 6\text{-}2$$

If the pore saturates fast, then the volume to consider is V_{pore} . Maximium internal concentration can be written as:

$$C_{Max,Int} = \frac{\rho_{particle,absolute} \cdot V_{particle} \cdot (1-\varphi)}{V_{pore}} = \rho_{particle,absolute} \cdot \frac{(1-\varphi)}{\varphi} \qquad 6\text{-}3$$

If there is no pore disintegration, porosity will only be important on dissolution when liquid inside the pores does not quickly saturate, hence

$$C_{sat} > C_{Max,\text{int}} = \rho_{particle,absolute} \cdot (1-\varphi) = \rho_{particle,envelope} \qquad 6\text{-}4$$

Equation 6-4 can be used as a condition to check if this will happen.

6.2.2 Particle physical properties

The porous particle used here to validate the framework is provided by Proctor and Gamble, named PANDORA with two different size cut 355-425 μm and 425-600μm. PANDORA is one of the spray-drying blown powders (BP) in Proctor and Gamble manufacturing process. It is a semi product of detergent powder.

Several experiments are carried out in order to obtain physical properties. Gravity dispersion for image analysis is used to measure PSD of PANDORA and results are shown in Figure 6.6. Resutls do not show clear differences of these two size cuts in terms of PSD, however PANDORA 355-425 has narrower distribution around 320 μm while PANDORA 425-600 has wider distribution around 450 μm. SEM images in Figure 6.7 show particle morphology. The porosity and specific surface area are measured by BET and results are compared to non porous Na_2CO_3 granule in Table 6.1. Solubility of particle at different temperature is measured by Conductivity meter and results are shown in Figure 6.8. It is difficult to calculate the diffusivity because there are more than one ingredients in these powders, hence at each temperature at 100 rpm, experiment data is first used to estimate the diffusivity.

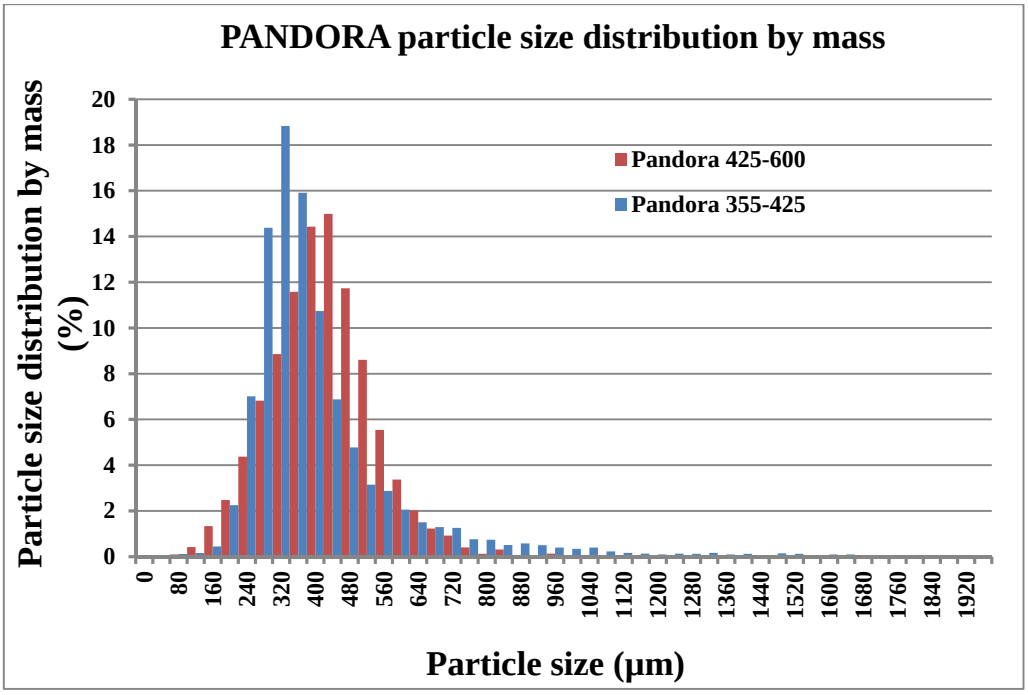

Figure 6. 6 Particle size distribution of PANDORA agglomerate.

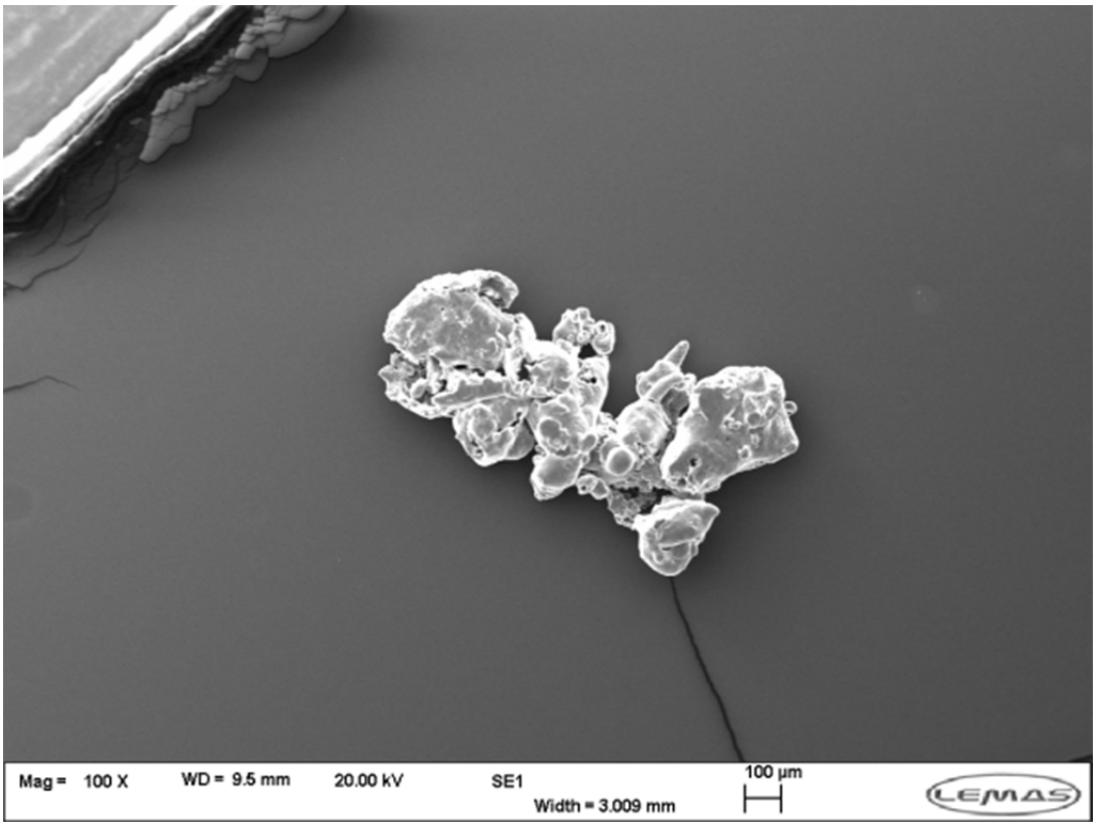

(a)

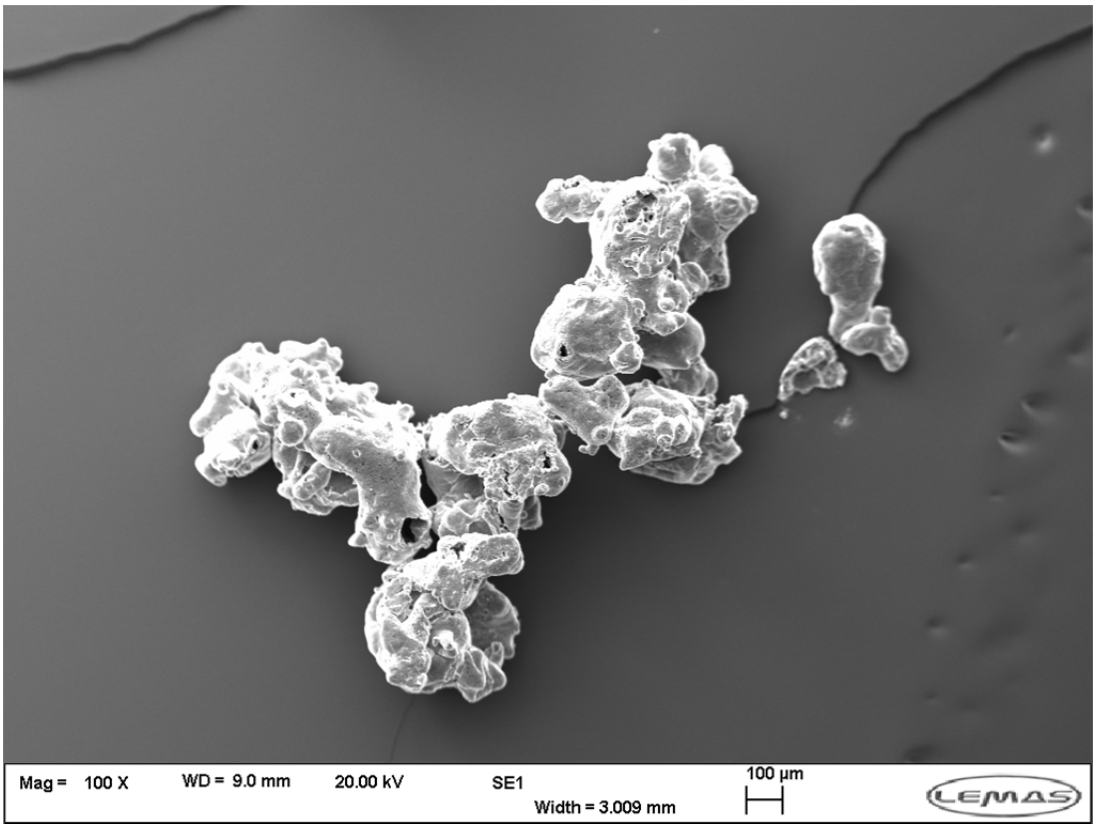

(b)

Figure 6. 7 SEM images of PANDORA agglomerate (a) 355-425 µm and (b) 425-600 µm.

Table 6. 1 BET results of specific surface area and porosity of Na_2CO_3 and PANDORA. Envelope density used for external area calculation = 1914·(1-0.41) = 1129 kg/m^3.

	Na2CO3	PANDORA 355-425	PANDORA 425-600
Specific surface area (m^2/g)	0.273	0.332	0.396
Porosity		0.41	0.41
Absolute density (kg/m^3)	2540	1914	1914
Envelope density (kg/m^3)		1129	1129

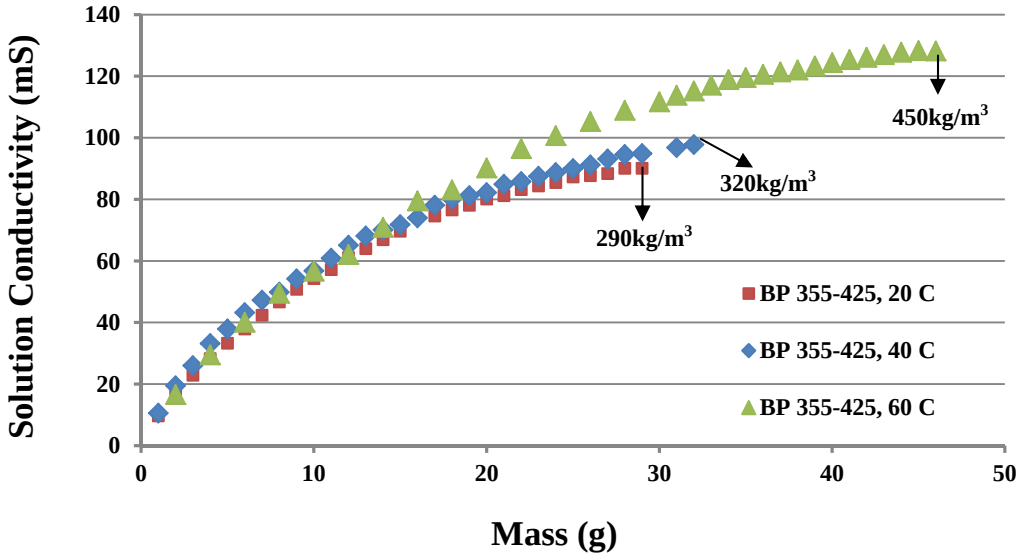

Figure 6. 8 Solubility test of PANDORA 355-425 µm at different temperature in 100 mL water.

For a porous particle, the density to be used to calculate whether the particle sinks, floats or is well suspended within the flow of the mixing system is the density of the particle when the pores have been filled with water (if this process takes place, i.e. hydrophilic particle or high pressures), which is given by Equation 6-5. A water filled density of 1539 kg/m3 indicates that these particles will sink to the bottom of vessel and substantial agitation will be needed in order to suspend them.

$$\rho_{filled\ H2O} = \rho_{water} \cdot \varphi + \rho_{particle,absolute} \cdot (1-\varphi) = 1539\ kg/m^3 \qquad 6\text{-}5$$

The solubility of PANDORA is the combination of many ingredients with the most soluble material sodium carbonate. Figure 6.8 shows conductivity vs PANDORA mass added to 100 mL water until reaching equilibrium. There is no linearity because of multiple ingredients. For this blown powder, C_s ≈ 1129 kg/m^3 and thus the particle cannot be fully dissolved inside its own porosity.

6.2.3 Model validation

Figure 6.9 (a) and (b) show experimental vs. predicted particle dissolution data for two different size cuts at 3 different rpms. Different from Na_2CO_3 granule dissolution test, all experiment data are slightly faster than expected from modelling, this is probably because of some parameters used in the modelling for example particle envelope density instead of absolute density, diffusivity (multi ingredients), solubility (experiment measure accuracy). However, the agreement is still acceptable.

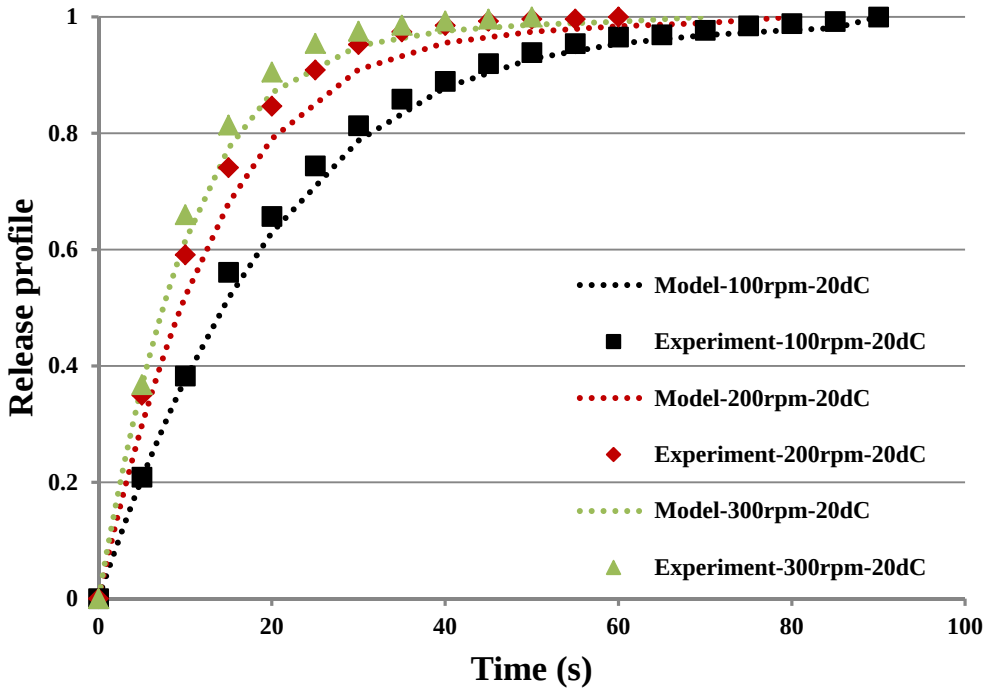

(a)

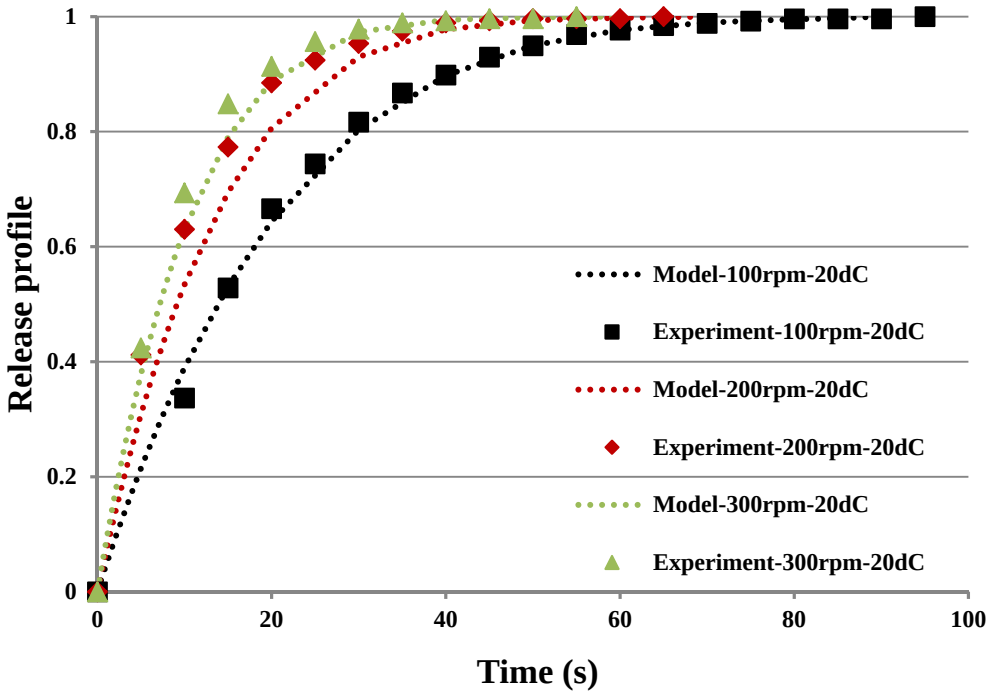

(b)

Figure 6. 9 PANDORA release profile of experiment data vs modelling (a) 355-425 µm and (b) 425-600 µm at 20 dC for 100 rpm, 200 rpm and 300 rpm.

At 100 rpm, similar phenomenon as Na_2CO_3 granule (Figure 6.4 (b)) did not happen. Lower density of these porous particles makes most of the particles suspended in the vessel, therefore experiment data agrees well with modelling data.

BET surface area of each size cuts, 0.332 m^2/g for 355-425 µm and 0.396 m^2/g for 425-600 µm, are not employed in framwork predicting. Instead, the surface area of a spherical particle with PSD is used in modelling which is the same as Na_2CO_3 granule. The SEM images in Figure 6.7 shows clearly that these porous particles are irregular shaped aggolomerate, rather than spherical granule. With a porosity of 0.41, it is understandable to use BET surface area to fit the model. However, if BET surface area is used, the only parameter which reamins unknown can be modified in order to make predicting result agree with experiment result is particle diffusivity, and diffusivity will be 10^{-12} m^2/s, which is too small and normally exists between

gas and solid [13]. As a result, spherical area is used at each temperature at 100 rpm to first obtain the diffusivity of PANDORA particle.

Figure 6.10 shows porous particle PANDORA dissolving at different temperature and agitating speed. (a) is size cut 355 to 425 µm and (b) sis 425 to 600 µm.

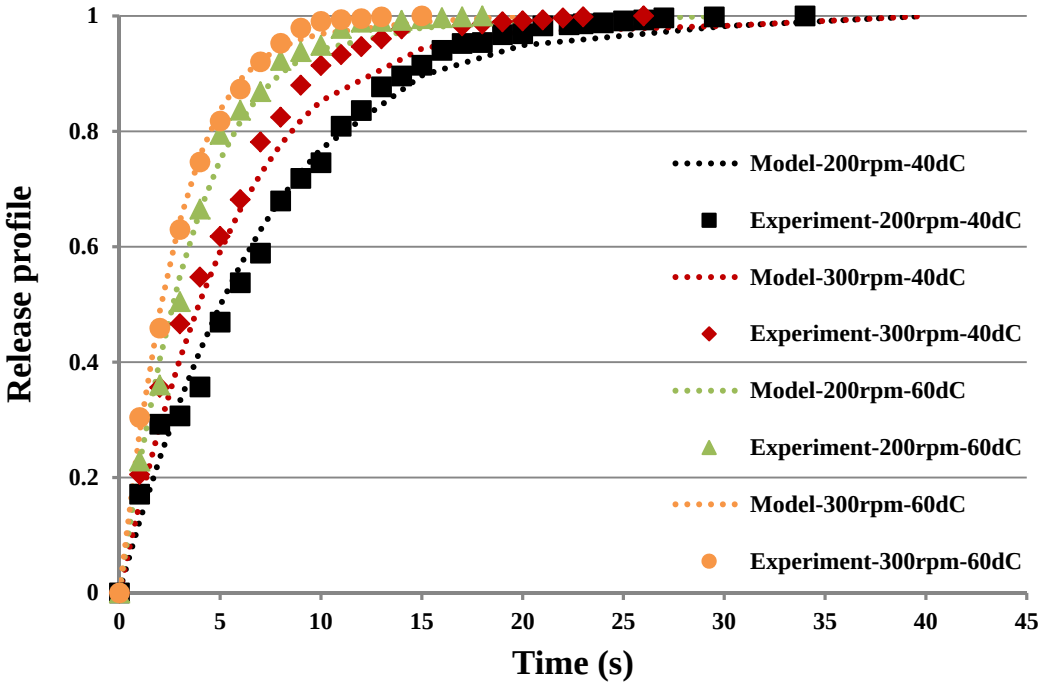

(a)

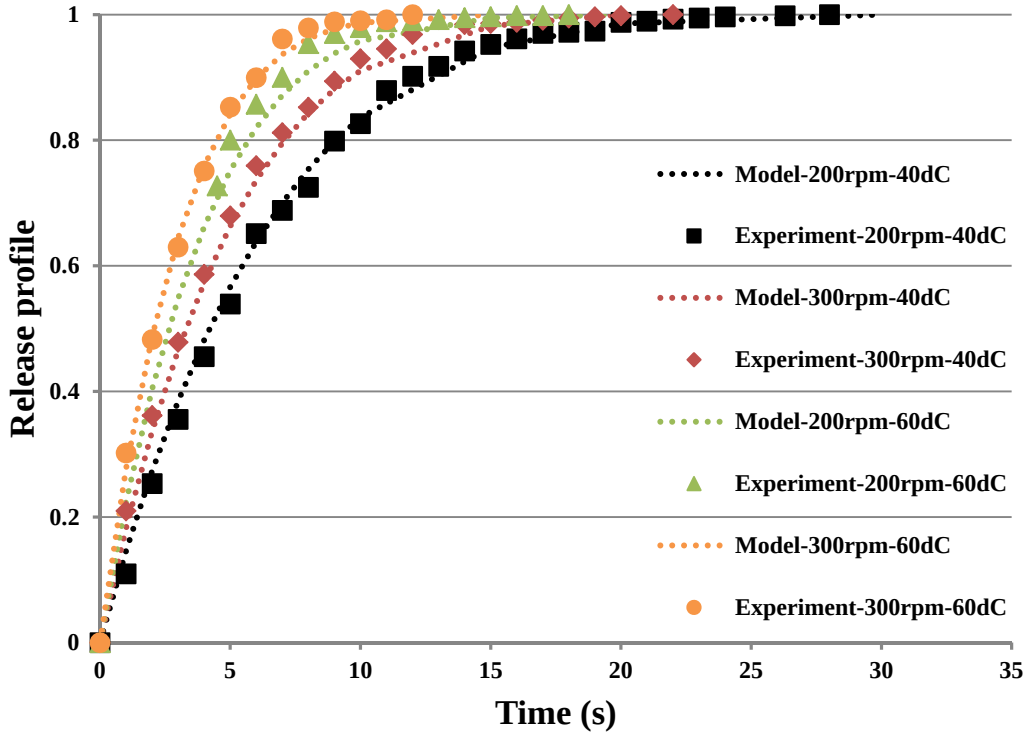

(b)

Figure 6. 10 PANDORA release profile of experiment data vs modelling (a) 355-425 µm and (b) 425-600 µm at 40 dC and 60 dC for 200 rpm and 300 rpm.

Although from Figure 6.6 these two different size cuts still have some big particles (> 1 mm), the main PSD is around 350 µm and 450 µm respectively. The modelling results are acceptable throughout different dissolution conditions. At some conditions for example PANDORA 355-425 µm at 40 dC 300 rpm, experiment data show faster dissolution than model predicting. But the others show well agreements even with bad experiment data for example at 40 dC 200 rpm for both PANDORA 355-425 µm and PANDORA 425-600 µm.

Since spherical area of the particle has to be used, diffusivity at 20 dC for PANDORA 355-425 µm and PANDORA 425-600 µm are first modified in the framework to make good agreement to experiment result. Later on, Stokes-Einstein equation (Equation 2-8) is used to estimate diffusivity at 40 dC and 60 dC. However the modelling results are not good, and further modification of diffusivities shown in

Table 6.2 have to be used to make the modelling results agree with experiment data at 100 rpm.

Table 6. 2 Comparing of diffusivity from Stokes-Einstein D_{SE} and experiment fitting results D_{fit} at different temperature.

	PANDORA 355-425 μm		PANDORA 425-600 μm	
Temperature (dC)	D_{SE} ($\times 10^{-10}$ m^2/s)	D_{fit} ($\times 10^{-10}$ m^2/s)	D_{SE} ($\times 10^{-10}$ m^2/s)	D_{fit} ($\times 10^{-10}$ m^2/s)
20	1.00	1.00	1.20	1.20
40	1.07	2.00	1.28	2.50
60	1.14	2.80	1.36	2.80

The diffusivities from fitting results are bigger than estimated data from Stokes-Einstein equation. This could be due to particle structure and different chemical composition as a function of the size cut leading to different diffusivity values.

After obtaining the right diffusivity of PANDORA at different temperature, predicting results from framework show very well agreement with experiment results at 200 rpm and 300 rpm. These results seem to indicae that within this mixing system, the developed framework still applies to spray drying porous particles.

Under this model, although internal surface area is not important, intraparticle porosity still plays a role since it decreases envelope density and thus increases external surface area by a factor of $1/(1-\varphi)$:

$$N_{factor} = \frac{Mass}{V_{particle} \cdot \rho_{particle,envelope}} = \left(\frac{1}{1-\varphi}\right) \cdot \frac{Mass}{V_{particle} \cdot \rho_{material}} \qquad 6\text{-}6$$

Thus, a particle with 50 % porosity will dissolve ~ 2 times faster than a non-porous particle of the same material and a particle with 90 % porosity will dissolve ~10 times faster (see Equation 6-6).

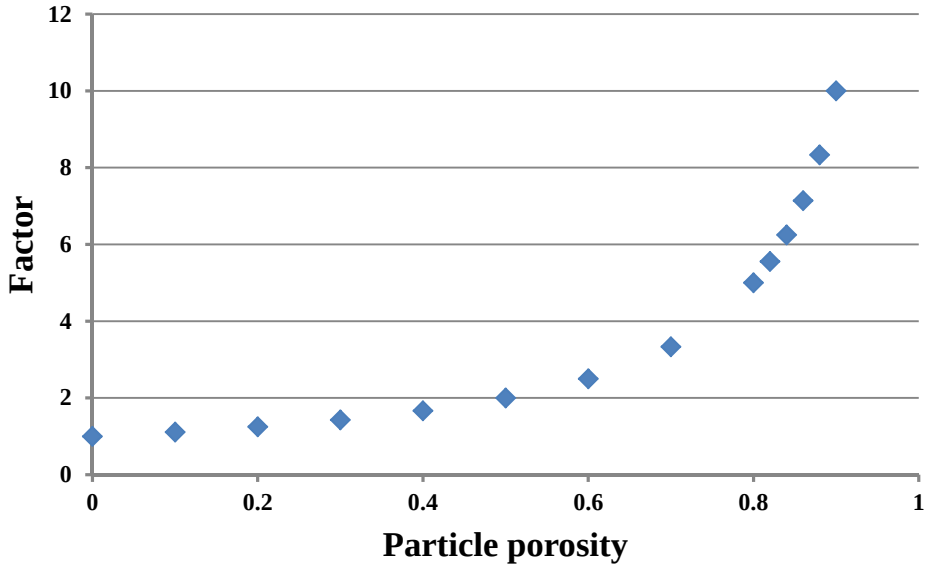

Figure 6. 11 External area increase factor as a function of particle porosity if no disintegration takes place.

6.3 Conclusions

The validation results from both non-porous single ingredient particles and porous multi ingredients particles proved that the developed framwork can be used to predict particle dissolution behaviour in a well mixed system.

By combining CFD simulation and mass transfer equation with particle size distribution information, this framework is cabable to predict particle dissolution behaviour. On the other hand, depends on the pre-known parameters, the model can also be used to estimate particle diffusion coefficient when there are more ingredients inside particle and particle structure is rather complicated. Furthermore,

if particle parameters are all well know, this model can be used to predict how much power is needed in the dissolution system for the required mass release behaviour.

In all the porous particle cases in this chapter, results indicate that within this mixing system, the external mass transfer of particle dominates the dissolution process, and the internal surface area is not important. However intraparticle porosity still plays a role as it decreases envelope density and thus increases external surface area.

For a dissolution system where particles are not well mixed, either floating on the surface or lumping at the bottom due to different envelope density of particles, local turbulent dissipation rate will be required to make the model fully cabable of predicting all the dissolution conditions in the future.

CHAPTER 7
CONCLUSIONS AND RECOMMENDATIONS

In this thesis, first, some dissolution parameters have been investigated in Chapter 4. Then in Chapter 5, a modelling framework combining CFD simulation and dissolution equations was developed and used to predict both single size particle dissolution and a population particle dissolution behaviour. In Chapter 6, experiments of single size particle dissolution and population particle dissolution were carried out at different conditions in order to validate the developed framework.

7.1 General conclusions

LBM based code *DigiDiss* has been used to simulate parameters affecting diffusion dominated dissolution, for example particle shape, surface area to volume ratio, pore structure.

Concentration distribution inside water has been plotted in order to show dissolution process. Four colour zones, white, red, yellow, green and blue represent concentration of solid Na_2CO_3 to water in a decreasing fashion. The images suggest that Na_2CO_3 dissolves faster than it diffuses away so that a significant high concentration zone is formed around particle.

Different shape particles (cube, cylinder, sphere) dissolve in a similar way. They shrink from the outside into the center of the particle, and eventually characteristic features such as corners and edges disappear, particles become spheres. These results indicate that mass transfer rate on the corners and edges are faster than on the face. Similar phenomena was also observed by Dr Yuan [28].

Surface area to volume ratio plays a more important role than particle shape and pore structure. With more or less the same volume but different surface area, disc shaped particle dissolves much faster than rod or tablet which indicates higher

surface area to volume ratio ends up much faster dissolution. By increasing specific surface area of particle, dissolution process can be fastened in a significant way.

The preliminary investigation of pore structure in particle shows that internal mass transfer can be limited due to saturated solution forms instantly inside pores. However future work of convective dissolution should be further investigated in order to fully understand how pore structure affecting dissolution when disintegration happens.

Particle dissolution under convective mass transfer condition has been studied by both experiment and simulation. Results show that agitation influence particle dissolution significantly mainly due to the shear rate around particle. The higher the shear rate, the faster particle dissolves. Concentration distribution was plotted by *DigiDiss* which shows water flow pattern. The total dissolution time from simulation is shorter than experiment results due to experiment observation limit and the velocity field coupling method between *DigiDiss* and COMSOL.

A very detailed investigation of wetting process has been done by both high speed camera experiment and COMSOL simulation. Liquid surface tension, pore size, wettability are important when pore size is in millimeter scale. Results from COMSOL simulation shows that, to the opposite of millimeter sized pores, wetting process in micro-sized range shows less importance in terms of the total dissolution time of detergent powder.

A modelling framework combing mass transfer equations and CFD simulation has been developed to predict particle dissolving behavior at different conditions (agitating speed, temperature) within standard mixing system or non-standard mixing system. Different sized particles can be predicted by the developed framework.

Two case studies have been presented in the thesis. First, the simple one where single sized Na_2CO_3 and Na_2SO_4 granule in marine impeller dissolution system has been predicted by the model. Results show that with increasing rotating speed and temperature, mass transfer rate can be increased. Temperature has a larger influence on dissolution behavior.

Then, the more complicated case of Na_2CO_3 granule with a certain PSD dissolving in PTWS 610 apparatus has been studied. Predicting results show smaller particles accelerate mass transfer rate at the initial stage while larger particles slow down dissolution at the later stage.

Experiment of the complicated case has been investigated in order to valite the developed framework. Provided by Procter and Gamble, non-porous single ingredient Na_2CO_3 granule with certain PSD was used. The predicting results from the framework at different temperature and agitating speed show decent agreements in the well mixed system. For the case while particles lump at the bottom of the vessel, local turbulent dissipation rate probably need to be considered to modify the framework in the future.

Porous particle PANDORA, also provided by Procter and Gamble, was dissolved in water at different temperature and agitating speed. Highly agreement between experiment and modelling prediction indicates that the developed model can be used for multi ingredients porous particle. Results also show that within the studied mixing system, the external mass transfer of particle dominates the dissolution, and the internal surface area is not important. However intraparticle porosity still plays a role as it decreases envelope density and thus increases external surface area.

In summary, the developed framework is fully capable of predicting particles with certain size distribution disslving in a well mixed system. On the other hand,

depending on the pre-known parameters, the model can be used to estimate particle parameters (diffusion coefficient, density, etc) when there are more ingredients inside particle and particle structure is rather complicated. Furthermore, if particle parameters are all pre-know, this model can be used to predict how much power is needed in the dissolution system for a required dissolution behaviour.

7.2 Future work

Developing a model to predict particle dissolution considering wetting, sinking, disintegration and dissolving is rather challenge from the fundermental of modelling point of view. The developed framework in this thesis takes into account particle size distribution, combines mass transfer equations and CFD simulation, is fully capable of predicting particle dissolution in well mixed system.

However, future research is still needed to improve the framework. Two different methods can become the direction. One is based on the existing LBM code *DigiDiss*, the other one is based on COMSOL.

DigiDiss

1. By modifying the code to consider capillary penetrating can give more information about intraparticle porosity influencing wetting and internal mass transfer simultaneously.

2. By improving the coupling between *DigiDiss* and COMSOL can give real time simulation of particle dissolving under convective condition. Or, alternatively, by modifying the code of *DigiDiss* to include rotating part in the model can also provide the ability to simulate flow field and dissolution at the same time.

3. In this thesis, disintegration process is not investigated either by simulation or experiment. Although the current *DigiDiss* has a function of disintegration, it is

artificial rather than real disintegration. It lacks the ability to define mechanical strength of particle, couple particle movement to flow field. This probably can be done by introducing DEM into the code.

Once single particle dissolution model is developed, the model can be expanded to particle clusters with different structure, ingredients etc. However, due to the efficiency of LBM, the final model can be very time consuming and require much powerful computer facility.

COMSOL

1. First improvement can be focused on replacing average turbulent dissipation rate with local one which probably can be achieved by using dimenionless number or introducing new parameters into the dissolution equations.

2. The advantage with COMSOL is its flexibility of coupling between different physical modulus. A simple validation of the developed model can be done by coupling the presented CFD module with particle tracing module to obtain the relative velocity around particle surface. By replacing turbulent dissipation rate with the relative velocity of particle, probably the developed framwork can be improved when particles lump at a local position or floating on water surface.

3. A more complicated future work with COMSOL could be coupling dissolution equation into CFD model, considering mass transfer, capillary penetration (two-phase flow), and agitating in the same model. However, this coupling requires geometry distortion which needs to be considered in the mesh process. The same as LBM model, the final model of COMSOL will also require a much powerful computer facility.

BIBIOGRAPHY

1. Hsu, W.L., M.J. Lin, and J.P. Hsu, Dissolution of Solid Particles in Liquids: A Shrinking Core Model. World Academy of Science, Engineering and Technology, 2009. 53: p. 6.

2. Noyes, A.A. and W.R. Whitney, The rate of solution of solid substances in their own solutions. The Journal of the American Chemical Society, 1897. 19(12): p. 930-934.

3. Frolov, V.F., Dissolution of disperse materials. Theoretical Foundations of Chemical Engineering, 1998. 32(4): p. 357-368.

4. Varelas, C.G., D.G. Dixon, and C.A. Steiner, Zero-order release from biphasic polymer hydrogels. Journal of Controlled Release, 1995. 34(3): p. 185-192.

5. Dokoumetzidis, A. and P. Macheras, A century of dissolution research: From Noyes and Whitney to the Biopharmaceutics Classification System. International Journal of Pharmaceutics, 2006. 321(1–2): p. 1-11.

6. Erich Brunner and S.v. Tolloczko, Über die Auflösungsgeschwindigkeit Fester Körper. Z. Phys. Chem., 1900. 35: p. 8.

7. Brunner, E., Reaktionsgeschwindigkeit in heterogenen Systemen. Z. Phys. Chem., 1904. 43: p. 47.

8. Nernst, W., Theorie der Reaktionsgeschwindigkeit in heterogenen Systemen. Z. Phys. Chem., 1904. 47: p. 4.

9. Hixson, A.W. and J.H. Crowell, Dependence of Reaction Velocity upon surface and Agitation. Industrial & Engineering Chemistry, 1931. 23(8): p. 923-931.

10. Wilderman, M., Über die Geschwindigkeit molekularer und chemischer Reaktionen in heterogenen Systemen. Erster Teil. Z. Phys. Chem., 1909. 66: p. 41.

11. Zdanovskii, A.B., The role of the interphase solution in the kinetics of the solution of salts. Zhur. Fiz. Khim. (USSR), 1946. 20: p. 12.

12. Miyamoto, S., A theory of the rate of solution of solid into liquid. Trans. Faraday Soc., 1933. 29: p. 16.

13. Hines, A.L. and R.N. Maddox, Mass Transfer: Fundamentals and Applications. 1 ed. 1984, New Jersey: Prentice Hall.

14. Frenkel, J., Kinetic Theory of Liquids. 1946, Oxford: Clarendon Press.

15. Wilke, C.R. and P. Chang, Correlation of diffusion coefficients in dilute solutions. AIChE Journal, 1955. 1(2): p. 264-270.

16. Nernst, W., Zur Kinetik der in Lösung befindlichen Körper. Erste Abhandlung. Theorie der Diffusion. Z. Phys. Chem., 1888. 2: p. 25.

17. R. A. Robinson, R.H.S., Electrolyte Solutions. 2nd ed. 1959, New York: Academic Press.

18. Cussler, E.L., Diffusion: Mass Transfer in Fluid System. 3 ed. 2009: Cambridge University Press.

19. Wurster, D.E. and P.W. Taylor, Dissolution rates. Journal of Pharmaceutical Sciences, 1965. 54(2): p. 169-175.

20. Ralph Gibbs Van Name and D.U. Hill, On the Influence of Alcohol and of Cane Sugar Upon the Rate of Solution of Cadmium in Dissolved Iodine. American Journal of Science, 1913. 36: p. 12.

21. Ralph Gibbs Van Name and D.U. Hill, On the rates of solution of metals in ferric salts and in chromic acid. American Journal of Science, 1916. 42: p. 32.

22. King, C.V., Reaction Rates at Solid—Liquid Interfaces. Journal of the American Chemical Society, 1935. 57(5): p. 828-831.

23. Fage, A. and H.C.H. Townend, An Examination of Turbulent Flow with an Ultramicroscope. Proceedings of the Royal Society of London. Series A, 1932. 135(828): p. 656-677.

24. Koganti, V., et al., Application of Modelling to Scale-Up Dissolution in Pharmaceutical Manufacturing. AAPS PharmSciTech, 2010. 11(4): p. 8.

25. Levins, D.M. and J.R. Glastonbury, Particle-liquid hydrodynamics and mass transfer in a stirred vessel. 2. Mass transfer. Trans Inst Chem Eng, 1972. 50: p. 15.

26. Keith, A. and P. Bouza (2011) The Impact Of Dissolution On Particle Size And Particle Shape Of Multi-Component Drug Delivery Systems.

27. Jia, X. and R.A. Williams, From microstructures of tablets and granules to their dissolution behaviour. Dissolution Technologies, 2006. 13: p. 10.

28. Yuan, Q., X. Jia, and R.A. Williams, Validation of a multi-component digital dissolution model for irregular particles. Powder Technology, 2013. 240(0): p. 25-30.

29. Bisrat, M. and C. Nyström, Physicochemical aspects of drug release. VIII. The relation between particle size and surface specific dissolution rate in agitated suspensions. International Journal of Pharmaceutics, 1988. 47(1–3): p. 223-231.

30. Niebergall, P.J., G. Milosovich, and J.E. Goyan, Dissolution rate studies. II. Dissolution of particles under conditions of rapid agitation. Journal of pharmaceutical sciences, 1963. 52: p. 236-241.

31. Hintz, R.J. and K.C. Johnson, The effect of particle size distribution on dissolution rate and oral absorption. International Journal of Pharmaceutics, 1989. 51(1): p. 9-17.

32. Mosharraf, M. and C. Nyström, The effect of particle size and shape on the surface specific dissolution rate of microsized practically insoluble drugs. International Journal of Pharmaceutics, 1995. 122(1–2): p. 35-47.

33. Nicklasson, M. and A. Brodin, The relationship between intrinsic dissolution rates and solubilities in the water—ethanol binary solvent system. International Journal of Pharmaceutics, 1984. 18(1–2): p. 149-156.

34. Brigante, M., G. Zanini, and M. Avena, Effect of pH, anions and cations on the dissolution kinetics of humic acid particles. Colloids and Surfaces A: Physicochemical and Engineering Aspects, 2009. 347(1–3): p. 180-186.

35. Brigante, M., G. Zanini, and M. Avena, On the dissolution kinetics of humic acid particles: Effects of pH, temperature and Ca2+ concentration. Colloids and Surfaces A: Physicochemical and Engineering Aspects, 2007. 294(1–3): p. 64-70.

36. Serajuddin, A.T.M. and C.I. Jarowski, Effect of diffusion layer pH and solubility on the dissolution rate of pharmaceutical bases and their hydrochloride salts I: Phenazopyridine. Journal of Pharmaceutical Sciences, 1985. 74(2): p. 142-147.

37. Serajuddin, A.T.M. and C.I. Jarowski, Effect of diffusion layer pH and solubility on the dissolution rate of pharmaceutical acids and their sodium salts II: Salicylic acid, theophylline, and benzoic acid. Journal of Pharmaceutical Sciences, 1985. 74(2): p. 148-154.

38. Hixson, A.W. and S.J. Baum, Agitation. Mass Transfer Coefficients in Liquid-Solid Agitation Systems. Industrial & Engineering Chemistry, 1941. 33(4): p. 478-485.

39. Hixson, A.W. and S.J. Baum, Agitation. Performance of Propellers in Liquid-Solid Systems. Industrial & Engineering Chemistry, 1942. 34(1): p. 120-125.

40. Nelson, K.G. and A.C. Shah, Convective diffusion model for a transport-controlled dissolution rate process. Journal of Pharmaceutical Sciences, 1975. 64(4): p. 610-614.

41. Forny, L., A. Marabi, and S. Palzer, Wetting, disintegration and dissolution of agglomerated water soluble powders. Powder Technology, 2011. 206(1-2): p. 72-78.

42. Washburn, E.W., The Dynamics of Capillary Flow. Physical Review, 1921. 17(3): p. 273-283.

43. Zhmud, B.V., F. Tiberg, and K. Hallstensson, Dynamics of Capillary Rise. Journal of Colloid and Interface Science, 2000. 228(2): p. 263-269.

44. Xue, H.T., et al., Contact angle determined by spontaneous dynamic capillary rises with hydrostatic effects: Experiment and theory. Chemical Physics Letters, 2006. 432(1–3): p. 326-330.

45. Richard, L., Ueber das Zeitgesetz des kapillaren Aufstiegs von Flüssigkeiten. Kolloid-Zeitschrift, 1918.

46. Masoodi, R., E. Languri, and A. Ostadhossein, Dynamics of liquid rise in a vertical capillary tube. Journal of Colloid and Interface Science, 2013. 389(1): p. 268-272.

47. Smulders, E., et al., Laundry Detergents, in Ullmann's Encyclopedia of Industrial Chemistry. 2002, Wiley-VCH.

48. Reynolds, G.K., et al., Breakage in granulation: A review. Chemical Engineering Science, 2005. 60(14): p. 3969-3992.

49. PTWS D610 Dual Drive Dissolution Tester Available from: http://www.pharma-test.de/ptws-d610/.

50. Way, T., An Overview of in vitro Dissolution and Drug Release. 2013.

51. Whitaker, S., Flow in porous media. 1986.

52. Fatt, I., The Network Model of Porous Media. Petroleum Transactions, AIME, 1956. 207: p. 38.

53. Payatakes, A.C., DYNAMICS OF OIL GANGLIA DURING IMMISCIBLE DISPLACEMENT IN WATER-WET POROUS-MEDIA. Annual Review of Fluid Mechanics, 1982. 14: p. 365-393.

54. Chen, J.-d. and J. Koplik, Immiscible fluid displacement in small networks. Journal of Colloid and Interface Science, 1985. 108(2): p. 304-330.

55. Chen, J.-D. and D. Wilkinson, Pore-Scale Viscous Fingering in Porous Media. Physical Review Letters, 1985. 55(18): p. 1892-1895.

56. King, P.R., The fractal nature of viscous fingering in porous media. Journal of Physics A: Mathematical and General, 1987. 20(8): p. L529.

57. Lenormand, R. and E. Touboul, Numerical models and experiments on immiscible displacements in porous media. J. Fluid Mech., 1988. 189: p. 23.

58. Furuberg, L., et al., Dynamics of Invasion Percolation. Physical Review Letters, 1988. 61(18): p. 2117-2120.

59. Tsakiroglou, C.D. and A.C. Payatakes, A new simulator of mercury porosimetry for the characterization of porous materials. Journal of Colloid and Interface Science, 1990. 137(2): p. 315-339.

60. Jerauld, G.R. and S.J. Salter, The effect of pore-structure on hysteresis in relative permeability and capillary pressure: Pore-level modeling. Transport in Porous Media, 1990. 5(2): p. 103-151.

61. Koplik, J. and T.J. Lasseter, ONE- AND TWO-PHASE FLOW IN NETWORK MODELS OF POROUS MEDIA. Chemical Engineering Communications, 1984. 26(4-6): p. 285-295.

62. Lenormand, R. and C. Zarcone, Capillary fingering: Percolation and fractal dimension. Transport in Porous Media, 1989. 4(6): p. 599-612.

63. Cieplak, M. and M.O. Robbins, Dynamical Transition in Quasistatic Fluid Invasion in Porous Media. Physical Review Letters, 1988. 60(20): p. 2042-2045.

64. Stokes, J.P., et al., Interfacial Stability of Immiscible Displacement in a Porous Medium. Physical Review Letters, 1986. 57(14): p. 1718-1721.

65. Måløy, K.J., J. Feder, and T. Jøssang, Viscous Fingering Fractals in Porous Media. Physical Review Letters, 1985. 55(24): p. 2688-2691.

66. Sahimi, M., Flow and transport in porous media and fractured rock. 1995: Wiley-VCH.

67. Sahimi, M., Applications of percolation theory. 1994: Taylor & Francis.

68. Louriou, C. and M. Prat, Pore Network Study of Bubble Growth by Vaporisation in a Porous Medium. International Journal for Thermal Sciences, 2011. xxx: p. 15.

69. Ramírez, A., et al., Simulation of uncompressible fluid flow through a porous media. Chaos, Solitons & Fractals, 2009. 39(4): p. 1753-1763.

70. Lin, C.-Y. and J.C. Slattery, Three-dimensional, randomized, network model for two-phase flow through porous media. AIChE Journal, 1982. 28(2): p. 311-324.

71. Turner, M.J., et al., Stiffness and deflection analysis of complex structures. J. Aeronautical Society, 1956. 23.

72. Zienkiewicz, O.C., P. Mayer, and Y.K.Cheung, Solution of anisotropic seepage by finite elements. Proc. Am. Soc. Civ. Eng., 1966. 92(EM1): p. 10.

73. Taylor, R.L. and C.B. Brown, Darcy flow solutions with a free surface. J. Hydraul. Div., Proc. ASCE. (2nd edn), 1967. 93: p. 9.

74. Gurtin, M.E., Variational principles for linear initial-value problems. Quart. Appl. Math, 1964. 22: p. 5.

75. Wilson, E.L. and R.E. Nickell, Application of the finite element method to heat conduction analysis. Nuclear Engineering and Design, 1966. 4(3): p. 276-286.

76. Javandel, I. and P.A. Witherspoon, Application of the Finite Element Method to Transient Flow in Porous Media. Society of Petroleum Engineers Journal, 1968. 8(3): p. 12.

77. Lewis, R.W. and H.R. Ghafouri, A novel finite element double porosity model for multiphase flow through deformable fractured porous media. International Journal for Numerical and Analytical Methods in Geomechanics, 1997. 21(11): p. 789-816.

78. Huber, R. and R. Helmig, Multiphase flow in heterogeneous porous media: A classical finite element method versus an implicit pressure–explicit saturation-based mixed finite element–finite volume approach. International Journal for Numerical Methods in Fluids, 1999. 29(8): p. 899-920.

79. Kadanoff, L.P., On Two Levels. Physics Today, 1986. 39(9): p. 7-9.

80. Genabeek, O.v. and D.H. Rothman, Macroscopic manifestations of microscopic flows through porous-media phenomenology from simulation. Annu. Rev. Earth Planet. Sci, 1996. 24: p. 25.

81. Grunau, D., S. Chen, and K. Eggert, A lattice Boltzmann model for multiphase fluid flows. Physics of Fluids A: Fluid Dynamics, 1993. 5(10): p. 2557-2562.

82. Blake, T.D., J. De Coninck, and U. D'Ortona, Models of Wetting: Immiscible Lattice Boltzmann Automata versus Molecular Kinetic Theory. Langmuir, 1995. 11(11): p. 4588-4592.

83. Martys, N.S. and H. Chen, Simulation of multicomponent fluids in complex three-dimensional geometries by the lattice Boltzmann method. Physical Review E, 1996. 53(1): p. 743-750.

84. Ferréol, B. and D.H. Rothman, Lattice-Boltzmann simulations of flow through Fontainebleau sandstone. Transport in Porous Media, 1995. 20(1): p. 3-20.

85. Guo, Z. and T.S. Zhao, Lattice Boltzmann model for incompressible flows through porous media. Physical Review E, 2002. 66(3): p. 036304.

86. Sullivan, S.P., L.F. Gladden, and M.L. Johns, Simulation of power-law fluid flow through porous media using lattice Boltzmann techniques. Journal of Non-Newtonian Fluid Mechanics, 2006. 133(2-3): p. 91-98.

87. Antonyuk, S., et al., Impact breakage of spherical granules: Experimental study and DEM simulation. Chemical Engineering and Processing: Process Intensification, 2006. 45(10): p. 838-856.

88. Moreno, R., M. Ghadiri, and S.J. Antony, Effect of the impact angle on the breakage of agglomerates: a numerical study using DEM. Powder Technology, 2003. 130(1–3): p. 132-137.

89. Thakur, P.K., J.S. Vinod, and B. Indraratna, Effect of particle breakage on cyclic densification of ballast: A DEM approach. IOP Conference Series: Materials Science and Engineering, 2010. 10(1): p. 012229.

90. Hossain, Z., et al., DEM analysis of angular ballast breakage under cyclic loading. Geomechanics and Geoengineering, 2007. 2(3): p. 175-181.

91. Jensen, R., et al., DEM Simulation of Particle Damage in Granular Media — Structure Interfaces. International Journal of Geomechanics, 2001. 1(1): p. 21-39.

92. Wendt, J.F., Computational Fluid Dynamics. 2009: Springer Berlin Heidelberg.

93. Yu, A.B. and B.H. Xu, Particle-scale modelling of gas-solid flow in fluidisation. Journal of Chemical Technology and Biotechnology, 2003. 78(2-3): p. 111-121.

94. Yin, K., Numerical modelling of agglomerate degradation. 1992, Aston University.

95. Tsuji, Y., T. Tanaka, and T. Ishida, Lagrangian numerical simulation of plug flow of cohesionless particles in a horizontal pipe. Powder Technology, 1992. 71(3): p. 239-250.

96. Xu, B.H. and A.B. Yu, Numerical simulation of the gas-solid flow in a fluidized bed by combining discrete particle method with computational fluid dynamics. Chemical Engineering Science, 1997. 52(16): p. 2785-2809.

97. Zhu, H.P., et al., Discrete particle simulation of particulate systems: Theoretical developments. Chemical Engineering Science, 2007. 62(13): p. 3378-3396.

98. Cundall, P.A. and O.D.L. Strack, A discrete numerical model for granular assemblies. Geotechnique, 1979. 29(1): p. 19.

99. Tsuji, Y., T. Kawaguchi, and T. Tanaka, Discrete particle simulation of two-dimensional fluidized bed. Powder Technology, 1993. 77(1): p. 79-87.

100. Hertz, H., On the contact of elastic solids. Journal fur die Reine und Angewandte Mathematik, 1881. 92: p. 16.

101. Mindlin, R.D. and H. Deresiewicz, Elastic spheres in contact under varying oblique forces. Journal of Applied Mechanics, 1953. 20(3): p. 15.

102. Thornton, C. and K.K. Yin, Impact of elastic spheres with and without adhesion. Powder Technology, 1991. 65(1-3): p. 14.

103. Johnson, K.L., K. Kendall, and A.D. Roberts, Surface energy and the contact of elastic solids. Proceedings of the Royal Society of London. Series A, 1971. 324(1558): p. 13.

104. Derjaguin, B.V., V.M. Muller, and Y.P. Toporov, Effect of contact deformation on the adhesion of elastic solids. Journal of Colloid and Interface Science, 1975. 53: p. 13.

105. Thornton, C., Coefficient of restitution for collinear collisions of elastic-perfectly plastic spheres. Journal of Applied Mechanics, 1997. 64.

106. Vu-Quoc, L. and X. Zhang, An elastoplastic contact force-displacement model in the normal direction: displacement-driven version. Proceedings: Mathematical, Physical and Engineering Sciences, 1999. 455(1991): p. 32.

107. Ergun, S., Fluid flow through packed columns. Chemical Engineering Progress, 1952. 48(2): p. 6.

108. Wen, C.Y. and Y.H. Yu, Mechanics of fluidization. Chemical Engineering Progress Symposium Series, 1966. 62(62): p. 12.

109. Felice, R.D., The voidage function for fluid-particle interaction systems. International Journal of Multiphase Flow, 1994. 59(16): p. 7.

110. Mazzei, L. and P. Lettieri, A drag force closure for uniformly dispersed fluidized suspensions. Chemical Engineering Science, 2007. 62(22): p. 14.

111. Beetstra, R., M.A.V.D. Hoef, and J.A.M. Kuipers, Drag force of intermediate Reynolds number flow past mono- and bidisperse arrays of spheres. AICHhE Journal, 2007. 53(2): p. 13.

112. Fan, L.S. and C. Zhu, Principles of Gas-Solid Flows. 1998: Cambridge University Press, Cambridge.

113. Saffman, P.G., The lift on a small sphere in a slow shear flow. Journal of Fluid Mechanics, 1965. 22(2): p. 16.

114. Tritton, D.J., Physical Fluid Dynamics. 1988: Clarendon Press, Oxford.

115. Štěpánek, F., Computer-Aided Product Design: Granule Dissolution. Chemical Engineering Research and Design, 2004. 82(11): p. 1458-1466.

116. Ansari, M.A. and F. Stepanek, Design of granule structure: Computational methods and experimental realization. AIChE Journal, 2006. 52(11): p. 3762-3774.

117. Kang, Q., et al., Lattice Boltzmann simulation of chemical dissolution in porous media. Physical Review E, 2002. 65(3): p. 036318.

118. Arnout, S., et al., Lattice Boltzmann model for diffusion-controlled indirect dissolution. Computers & Mathematics with Applications, 2008. 55(7): p. 1377-1391.

119. Jia, X. and R.A. Williams, A Hybrid Mesoscale Modelling Approach to Dissolution of Granules and Tablets. Chemical Engineering Research and Design, 2007. 85(7): p. 1027-1038.

120. Crank, J., The Mathematics of Diffusion. 2 ed. 1979: Oxford University Press.

121. Strikwerda, J.C., Finite Difference Schemes and Partial Differential Equations. second ed. 2004, Philadelphia, USA: Society for Industrial and Applied Mathematics.

122. Siebold, A., et al., Effect of dynamic contact angle on capillary rise phenomena. Colloids and Surfaces A: Physicochemical and Engineering Aspects, 2000. 161(1): p. 81-87.

123. Hamraoui, A. and T. Nylander, Analytical Approach for the Lucas–Washburn Equation. Journal of Colloid and Interface Science, 2002. 250(2): p. 415-421.

124. Quéré, D., É. Raphaël, and J.-Y. Ollitrault, Rebounds in a Capillary Tube. Langmuir, 1999. 15(10): p. 3679-3682.

125. Tagawa, M., K. Gotoh, and Y. Nakagawa, Penetration of water/ethanol mixtures into silanized silica fibrous assemblies. Journal of Adhesion Science and Technology, 1998. 12(12): p. 1341-1353.

126. Balard, H., et al., Trimethylchlorosilane modified silica surfaces: characterization by inverse gas chromatography using PDMS oligomers as probes. Composite Interfaces, 1998. 6(1): p. 19-25.

127. Etacude. 2004-2008, Etacude.

128. Paul, E.L., V.A. Atiemo-Obeng, and S.M. Kresta, Handbook of Industrial Mixing: Science and Practice. 2004: Wiley-IEEE.

129. U.S.PHARMACOPEIA.